DOT/FAA/AR-07/16

Air Traffic Organization
Operations Planning
Office of Aviation Research
and Development
Washington, DC 20591

Characteristics of Runback Ice Accretions and Their Aerodynamic Effects

April 2007

Final Report

U.S. Department of Transportation
Federal Aviation Administration

NOTICE

Technical Report Documentation Page

1. Report No. DOT/FAA/AR-07/16	2. Government Accession No.	3. Recipient's Catalog No.

4. Title and Subtitle
CHARACTERISTICS OF RUNBACK ICE ACCRETIONS AND THEIR AERODYNAMIC EFFECTS

5. Report Date
April 2007

6. Performing Organization Code

7. Author(s)
Edward A. Whalen, Andy P. Broeren, and Michael B. Bragg

8. Performing Organization Report No.

9. Performing Organization Name and Address
University of Illinois
Aerospace Engineering Department
306 Talbot Laboratory, 104 S. Wright St.
Urbana, IL 61801

10. Work Unit No. (TRAIS)

11. Contract or Grant No.

12. Sponsoring Agency Name and Address
U.S. Department of Transportation
Federal Aviation Administration
Air Traffic Organization Operations Planning
Office of Aviation Research and Development
Washington, DC 25091

13. Type of Report and Period Covered
Final Report

14. Sponsoring Agency Code
AIR-100

15. Supplementary Notes
The Federal Aviation Administration Airport and Aircraft Safety R&D Division COTR was James Riley.

16. Abstract

The results of a research program to investigate runback ice accretions due to hot-air ice protection systems, scaling of external flow parameters for testing thermal systems, and the resulting aerodynamic effects are presented. Ice accretion testing was conducted at the National Aeronautics and Space Administration Glenn Icing Research Tunnel to evaluate thermal scaling methods and produce representative runback ice accretions using a business jet wing section equipped with a hot-air, anti-icing system. Test conditions simulated an airplane holding in both at ambient static air temperatures near freezing (warm hold) and well below freezing (cold hold), as well as descending through (descent) Title 14 Code of Federal Regulations Part 25 Appendix C icing conditions. Warm-hold ice accretions were characterized on the suction surface by dense frozen rivulets that formed a ridge while the pressure surface accretion was composed of nodules and chunks that formed a ridge. In all cases, a clean airfoil region of varying chordwise extent was located upstream of the runback ice accretions. The runback ridge formations were shown to be very sensitive to total air temperature in both height and chordwise location. Increased hot-air temperature and mass flow rate were found, in general, to correspond to shorter ridges located farther aft on the model. The cold-hold accretions had the character of rime ice and exhibited more spanwise variation due to the proximity of the ridge to the hot-air jet impingement zones. Descent accretions also exhibited spanwise variation in chordwise position, but were more uniform in height than the cold-hold accretion. Results of the scaling analysis showed that a useful and qualitatively accurate scaling method was developed for scaling thermal anti-icing systems for ground testing, but further development and investigation of the methods and governing equations are required.

Wind tunnel testing was also conducted to evaluate the aerodynamic performance effects of runback ice accretions. Simulated ice shapes were scaled from the documented ice accretions for testing in the Illinois 3- by 4-ft subsonic wind tunnel. Simple geometric scaling and boundary-layer scaling methods were used. The National Advisory Committee for Aeronautics (NACA) 3415 and the NACA 23102 were tested at a Reynolds number of $1.8\text{x}10^6$ and Mach number of 0.18, with and without the simulated ice shapes attached. The maximum lift coefficient (C_{lmax}) of the NACA 3415 was reduced to 1.16 from 1.35, and the stalling angle of attack was reduced by 1 degree due to the three-dimensional (3-D) warm hold simulation, while the NACA 23012 experienced a reduction in C_{lmax} to 1.16 from 1.46, and a loss of 2 degrees in stalling angle of attack. The 3-D cold-hold simulation reduced C_{lmax} to 0.9 and caused a 3 degree reduction in stalling angle of attack for the NACA 3415. The same ice shape reduced C_{lmax} to 0.73 and caused a 4 degree reduction in stalling angle of attack for the NACA 23012. Geometrically scaled two-dimensional (2-D) simulations of the warm-hold accretions were found to enhance the lift performance of the NACA 3415 and had little effect on the NACA 23012. The boundary-layer-scaled ice shapes were observed to cause greater penalties than both the 2-D and 3-D geometrically scaled ice shapes. Therefore, geometric scaling may not be sufficient for scaling runback-type ice accretions over the range of scales and Reynolds number tested.

17. Key Words
Runback icing, Ridge ice, Thermal ice protection, Anti-icing, Hot-air, Aerodynamic performance degradation, Simulated ridge shapes, Spanwise ridge ice

18. Distribution Statement
This document is available to the public through the National Technical Information Service (NTIS) Springfield, Virginia 22161.

19. Security Classif. (of this report) Unclassified	20. Security Classif. (of this page) Unclassified	21. No. of Pages 92	22. Price

Form DOT F1700.7 (8-72) Reproduction of completed page authorized

TABLE OF CONTENTS

Page

EXECUTIVE SUMMARY xi

1. INTRODUCTION 1

    1.1 Review of Literature 1
    1.2 Objectives and Approach 2

2. ICE ACCRETION TESTS 4

    2.1 Facility and Model 4
    2.2 Reference Conditions 6
    2.3 Thermal Scaling 6
    2.4 Scaled Icing Results Using Matched Static Temperature 9

        2.4.1 Appendix C Warm-Hold Case 9
        2.4.2 Supercooled Large Droplet Warm-Hold Case 13
        2.4.3 Appendix C Cold-Hold Case 15
        2.4.4 Descent Case 17

    2.5 Scaled Icing Results Using Matched Total Temperature 19
    2.6 Sensitivity to Hot-Air Settings 22

3. AERODYNAMIC TESTS 23

    3.1 Facility and Models 24
    3.2 Ice Shape Simulation and Scaling 26

        3.2.1 Geometrically Scaled, 3-D Ice Shape Simulations 27
        3.2.2 Geometrically and Boundary-Layer-Scaled 2-D Ice Shape Simulations 30

    3.3 Results 31

        3.3.1 Warm Hold 31
        3.3.2 Effect of Chordwise Extent of Ridges 35
        3.3.3 Lift Enhancement of Ridges 37
        3.3.4 Cold Hold 44
        3.3.5 Descent 48

4. SUMMARY 49

    4.1 Ice Accretion Tests 49
    4.2 Aerodynamic Tests 51

5. CONCLUSIONS 52

5.1 Ice Accretion Tests 52
5.2 Aerodynamic Tests 53

6. RECOMMENDATIONS 53

7. REFERENCES 54

APPENDICES

A—Icing Research Tunnel Run Logs
B—Total Temperature Variation Results

LIST OF FIGURES

Figure		Page
1	Representative Business Jet Thermal Model Installed in the IRT	5
2	Cross Section of the Model Leading Edge Showing the Piccolo Tube and Diffuser With Airflow Path Indicated	5
3	Tracing of a Warm-Hold Runback Accretion After a 22.5-Minute Spray, Using the h, K_0, RHF Scaling Method	11
4	Close-Up Photograph (Suction Surface) of a Warm-Hold Runback Accretion After a 22.5-Minute Spray, Using the h, K_0, RHF Scaling Method	12
5	Overall Photograph (Suction Surface) of a Warm-Hold Runback Accretion After a 22.5-Minute Spray, Using the h, K_0, RHF Scaling Method	12
6	Overall Photograph (Pressure Surface) of a Warm-Hold Runback Accretion After a 22.5-Minute Spray, Using the h, K_0, RHF Scaling Method	13
7	Close-Up Photograph (Suction Surface) of a Warm-Hold SLD Runback Accretion After a 22.5-Minute Spray, Using the h, K_0, RHF Scaling Method	14
8	Close-Up Photograph (Pressure Surface) of a Warm-Hold SLD Runback Accretion After a 22.5-Minute Spray, Using the h, K_0, RHF Scaling Method	14
9	Tracing of a Cold-Hold Runback Accretion After an 8.6-Minute Spray, Using the h, K_0, RHF Scaling Method	16
10	Close-Up Photograph (Suction Surface) of a Cold-Hold Runback Accretion After an 8.6-Minute Spray, Using the h, K_0, RHF Scaling Method	16
11	Overall Photograph (Pressure Surface) of a Cold-Hold Runback Accretion After an 8.6-Minute Spray, Using the h, K_0, RHF Scaling Method	17
12	Tracing of a Descent Runback Accretion After a 1.7-Minute Spray, Using the h, K_0, RHF Scaling Method	18
13	Close-Up Photograph (Suction Surface) of a Descent Runback Accretion After a 1.7-Minute Spray, Using the h, K_0, RHF Scaling Method	18
14	Close-Up Photograph (Pressure Surface) of a Descent Runback Accretion After a 1.7-Minute Spray, Using the h, K_0, RHF Scaling Method	19
15	Photograph of the Suction Surface (Trailing-Edge Region) for the Warm-Hold Case With Matched Total Temperature	21

16 Thermocouple Surface Temperature Data for the Static and Total Temperature Scaling of the Warm-Hold Case 21

17 Suction Surface Ice Accretion Following a 22.5-Minute spray at Warm-Hold Conditions and a Total Temperature of 28.5°F 22

18 Pressure Surface Ice accretion Following a 22.5-Minute Spray at Warm-Hold Conditions and a Total Temperature of 28.5°F 22

19 Experimental Setup in Illinois 3- by 4-Foot Wind Tunnel 24

20 Boundary-Layer Rake (Viewed From Above) Attached to Model 25

21 Comparison of Pressure Profiles at Matched C_l from XFOIL (Re=7.65X10^6, M=0.33) 26

22 Photograph of Suction Surface 3-D Ice Shape Simulation for Warm-Hold Case 28

23 Photograph of 3-D Ice shape Simulation for Cold-Hold Case 29

24 Effect of 3-D Ice Shape Simulation for the Warm-Hold Case on the Lift, Drag, and Pitching Moment of the NACA 23012 and 3415 (Re=1.8x10^6, M=0.18) 32

25 Comparison of the Effect of Geometrically Scaled, 3-D and 2-D Ice Shape Simulations for the Warm-Hold Case on the Lift, Drag, and Pitching Moment of the NACA 3415 (Re=1.8x106, M=0.18) 33

26 Comparison of the Effect of Geometrically Scaled, 3-D and 2-D Ice Shape Simulations for the Warm-Hold Case on the Lift, Drag, and Pitching Moment of the NACA 23012 (Re=1.8x10^6, M=0.18) 34

27 Effect of a 2-D Ice Shape Simulation for the Warm-Hold Case (Suction Surface Only) on the Lift, Drag, and Pitching Moment of the NACA 3415 (Re=1.8x10^6, M=0.18) 35

28 Effect of Chordwise Extent of k=0.063-Inch and k=0.125-Inch Ridges at x/c=0.05 and 0.10 on the (a) α_{stall} and (b) C_{lmax} of the NACA 23012 (Re=1.8x10^6, M=0.18) 36

29 Effect of Chordwise Extent of K=0.063-Inch and K=0.125-Inch Ridges at x/c=0.05 and 0.10 on the (a) $\alpha_{l,0}$ and (b) $C_{d,0}$ of the NACA 23012 (Re=1.8x10^6, M=0.18) 36

30 Fluorescent Oil Flow Visualization at α=16° for the NACA 3415 With the Geometrically Scaled Ridge for the Warm-Hold Case (Re=1.8x10^6, M=0.18) 37

31 Fluorescent Oil Flow Visualization at (a) α=6° and (b) α=8° for the NACA 3415 With the Boundary-Layer-Scaled Ridge for theWarm-Hold Case (Re=1.8x10^6, M=0.18) 38

32 Fluorescent Oil Flow Visualization Analysis With (a) the Geometrically Scaled and (b) the Boundary-Layer-Scaled Ridge for the Warm-Hold Case at x/c=0.16 (NACA 3415, *Re*=$1.8\text{x}10^6$, M=0.18). 39

33 Effect of Ridge Height at x/c=0.16 on the NACA 3415 (*Re*=$1.8\text{x}10^6$, M=0.18) 40

34 Comparison of K/δ for Various Ice Shapes at x/c=0.15 41

35 Boundary-Layer Profile Measurements at α=8° for the Geometrically Scaled Ridge for the Warm-Hold Case at x/c=0.18, 0.20, 0.24, and 0.30 (NACA 3415, *Re*=1.8x106, M=0.18) 42

36 Boundary-Layer Profiles Measurements at $\alpha=8^{\text{o}}$ for the Boundary-Layer-Scaled Ridge for the Warm-Hold Case at x/c=0.18, 0.20, 0.24, and 0.30 (NACA 3415, *Re*=$1.8\text{x}10^6$, M=0.18) 42

37 NACA 3415 Pressure Profiles Near Maximum Lift With the (a) Geometrically Scaled and (b) Boundary-Layer-Scaled Ice Shape Installed at x/c=0.16 (*Re*=$1.8\text{x}10^6$, M=0.18) 43

38 Effect of Ridge for the Cold-Hold Case on the Lift, Drag, and Pitching Moment of the NACA 23012 and 3415 (*Re*=$1.8\text{x}10^6$, M=0.18) 45

39 Comparison of the Effect of Geometrically Scaled, 2-D and 3-D Ice Shape Simulations for the Cold-Hold Case on the Lift, Drag, and Pitching Moment of the NACA 3415 (*Re*=$1.8\text{x}10^6$, M=0.18) 46

40 Comparison of the Effect of Geometrically Scaled, 2-D and 3-D Ice Shape Simulations for the Cold-Hold Case on the Lift, Drag, and Pitching Moment of the NACA 23102 (*Re*=$1.8\text{x}10^6$, M=0.18) 47

41 Effect of 2-D Ice Shape Simulation for the Cold-Hold Case on the Lift, Drag, and Pitching Moment of the NACA 3415 (*Re*=$1.8\text{x}10^6$, M=0.18) 48

42 Effect of 2-D Ice Shape Simulation for the Descent Case on the Lift, Drag, and Pitching Moment of the NACA 23012 and 3415 (*Re*=$1.8\text{x}10^6$, M=0.18) 49

LIST OF TABLES

Table Page

1 Reference Conditions 6

2 Warm-Hold-Scaled Conditions 8

3 Variation in Measured Runback Ridge Height From Repeat Runs at the Same Conditions 10

4 Warm-Hold SLD Conditions 13

5 Cold-Hold Conditions 15

6 Descent Conditions 17

7 Effect of Total Temperature Variation on Ridge Location and Height 20

8 Comparison of Scaling Methods Based on Total and Static Temperature 20

9 Sensitivity of a Warm-Hold Runback Ridge to the Bleed Air Temperature 23

10 Sensitivity of a Warm-Hold Runback Ridge to the Bleed Air Mass Flow Rate 23

11 Estimated Experimental Uncertainties 25

12 Ridge Scaling for Warm-Hold Case 31

13 Ridge Scaling for Cold-Hold Case 31

LIST OF SYMBOLS AND ACRONYMS

α	Angle of attack
$\alpha_{l,0}$	Zero-lift angle of attack
α_{stall}	Stalling angle of attack
c	Model chord length
C_d	Drag coefficient
$C_{d,0}$	Zero-lift drag coefficient
C_l	Lift coefficient
C_{lmax}	Maximum lift coefficient
C_m	Quarter-chord pitching moment coefficient
C_p	Pressure coefficient
h	Convective heat transfer coefficient
k	Ice height or thickness
k_0	Thermal conductivity
K_0	Modified droplet inertia parameter
μ	Absolute viscosity
M	Mach number
m_w	Water catch rate
n_0	Stagnation point freezing fraction
Nu	Nusselt number
P	Static pressure
Pr	Prandtl number
δ	Delta
ρ	Density
Re	Reynolds number
T_s	Static temperature
T_0	Total temperature
μm	Microns
V	Airspeed (tunnel or flight)
x	Chordwise position along airfoil
y	Model coordinate normal to chordline
2-D	Two-dimensional
3-D	Three-dimensional
Alt.	Altitude
BTU	British thermal unit
CFR	Code of Federal Regulations
Deg.	Degrees
FAA	Federal Aviation Administration
g/m^3	Grams per meter cubed
IPS	Ice protection systems
IR	Infrared
IRT	Icing Research Tunnel
ktas	Knots true airspeed
lbm/s/ft	Pounds mass per second per foot
LWC	Liquid water content

MVD	Median volumetric diameter
NACA	National Advisory Committee for Aeronautics
NASA	National Aeronautics and Space Administration
psia	Pounds per square inch absolute
RHF	Relative heat factor
S	Surface distance along airfoil from leading edge
SLD	Supercooled large droplet

EXECUTIVE SUMMARY

The results of a research program to investigate runback ice accretions due to hot-air ice protection systems (IPS), scaling of external flow parameters for testing thermal systems, and the resulting aerodynamic effects are presented in this report. The research program was motivated by the need to test thermal ice protection systems in sea-level icing facilities and produce representative ice accretions for aerodynamic tests. The difference in altitude between the test facility and operational conditions caused a pressure mismatch that affected the heat and mass transfer in the external flow. This necessitated a scaling method to correct for the altitude difference and produce accurate operational runback ice shapes in a sea-level icing wind tunnel.

An icing tunnel test was conducted at the National Aeronautics and Space Administration Glenn Icing Research Tunnel (IRT) to evaluate three scaling methods developed to match thermodynamic and droplet impingement parameters. These scaling methods were based on matching either the static or total air temperature of the reference conditions. A representative business jet wing section with a hot-air, anti-icing system was used for the test. Test conditions simulated an airplane holding in both ambient static air temperatures near freezing (warm hold) and well below freezing (cold hold), as well as descending through (descent) Title 14 Code of Federal Regulations Part 25 Appendix C (herein after referred to as Appendix C) icing conditions. The warm-hold and cold-hold ice shapes were accreted at 3 degrees angle of attack, and the descent ice shape was accreted at -1 degrees angle of attack. Warm-hold ice accretions were characterized on the suction surface by dense frozen rivulets that formed a ridge, and the pressure surface accretion was composed of nodules and chunks that formed a ridge. Test conditions also included a simulation of holding in supercooled large drop (SLD) icing conditions at an ambient, static-air temperature near freezing. Results for this case (SLD warm-hold case) were similar to the results for the warm-hold case in Appendix C conditions. The suction surface was composed of rivulets but had a smoother glaze character near the beginning of the ridge, and the pressure surface ridge was composed of densely packed nodules. The cold-hold accretions had the character of rime ice and exhibited more spanwise variation due to the proximity of the ridge to the hot-air jet impingement zones. Descent accretions also exhibited spanwise variation in chordwise position, but were more uniform in height than the cold-hold accretion. On both the pressure and suction surface, the ridge in the descent case was very short in the chordwise direction, compared to the warm- and cold-hold cases, and was followed by a region of frost. An investigation into the sensitivity of runback ice shapes to the air temperature was conducted at the warm-hold condition. The shapes were shown to be very sensitive to temperature in both height and chordwise location. Sensitivity to the settings of the hot-air system was also investigated at the warm-hold condition. In general, increased hot-air temperature and mass flow rate were found to correspond to shorter ridges located farther aft on the model. Data collected from the test included surface temperatures (using both thermocouples and an infrared camera), photographs, high-definition video, tracings, and molds. Results of the scaling analysis showed that a useful and qualitatively accurate scaling method was developed for scaling thermal anti-icing systems for ground testing. However, further development and investigation of the method and governing equations are required, including generating full-scale runback ice accretions for quantitative evaluation of the scaling methods.

A wind tunnel test was also conducted to evaluate the aerodynamic performance effects of simulated ice shapes based on the shapes observed in the icing tunnel test. Aerodynamic tests

revealed significant aerodynamic penalties for all flight conditions tested. Runback ice accretions present a unique problem in iced-airfoil aerodynamics in that the airfoil typically has a clean leading edge forward of the ice shape. To investigate the aerodynamic effects of runback ice accretions, ice shape simulations were scaled from accretions obtained in testing at the IRT for testing in the Illinois 3- by 4-foot subsonic wind tunnel. Simple geometric scaling based on airfoil chord, as well as boundary-layer scaling based on estimated boundary-layer thickness, was used. The National Advisory Committee for Aeronautics (NACA) 3415 and the NACA 23102 were tested at a Reynolds number of 1.8×10^6 and Mach number of 0.18 with and without the simulated ice shapes attached. Simple two-dimensional (2-D) simulations were constructed for the test, as well as three-dimensional (3-D) simulations that used multiple substrate layers and roughness to simulate the features of the full-scale accretion. Significant penalties due to runback accretions were identified. The maximum lift coefficient (C_{lmax}) of the NACA 3415 was reduced to 1.16 from 1.35, and the stalling angle of attack was reduced by 1 degree due to the 3-D warm-hold simulation. The NACA 23012 experienced a reduction in C_{lmax} to 1.16 from 1.46 and a loss of 2 degrees in stalling angle of attack. The 3-D cold-hold simulation reduced C_{lmax} to 0.9 and caused a 3 degree reduction in stalling angle of attack for the NACA 3415. The same ice shape reduced C_{lmax} to 0.73 and caused a 4 degree reduction in stalling angle of attack for the NACA 23012.

Geometrically scaled, 2-D simulations of the warm-hold accretions were found to enhance the lift performance of the NACA 3415 and had little effect on the NACA 23012. The cause of this phenomenon is hypothesized to be a combination of energizing the boundary layer and the pressure distribution established by the presence of the ridge shape. The boundary-layer-scaled equivalent of that ice shape simulation was observed to reverse this phenomenon. Boundary-layer calculations indicated that the geometrically scaled ice shape simulation was approximately the same height as the local boundary thickness at angles of attack near stall. The boundary-layer-scaled ice shape simulations were observed to cause greater penalties than both the geometrically scaled, 2-D and 3-D ice shape simulations. Boundary-layer-scaled, 3-D ice shape simulations remain to be tested. It should be noted that data regarding the effect of full-scale runback ice accretions are not publicly available at this time. Therefore, it is difficult to judge which scaling method is appropriate. However, it is clear from this work that geometric scaling may not be sufficient for scaling runback-type ice accretions for aerodynamic testing.

Continued testing in this area should include both thermal scaling investigations and aerodynamic performance penalty investigations. The ability to generate runback ice accretions in a controlled environment in which the reference, full-scale conditions can be simulated is critical to understanding the external flow associated with thermal ice protection systems. It is also critical to assessing the aerodynamic performance effects of runback ice accretions. Testing in a pressurized icing wind tunnel is recommended to collect these data. A full-scale test is desirable for generating ice shapes for aerodynamic testing, but is not required to achieve the goal of understanding the thermal scaling problem. It has been shown that Reynolds number effects may be important to assessing the performance penalties of runback ice accretions, especially in the case of warm-hold accretions. Ideally, a full-scale test at high Reynolds number of high-fidelity runback simulations would be conducted to assess the aerodynamic penalties of these accretions. Alternatively, scaled aerodynamic testing of runback ice simulations in a high-

Reynolds number facility would address Reynolds number concerns and provide reasonable estimates of the aerodynamic performance effects of these accretions.

1. INTRODUCTION.

Runback ice accretions occur on wings with thermal anti-icing systems when the system does not evaporate 100% of the water that impinges on the surface. The water runs back from the impingement zone, leaving the leading-edge region without ice. When the water reaches the region where the added heat no longer raises the surface temperature above freezing, the water begins to freeze and a ridge line develops. Frozen rivulets follow the ridge line in cases where the air temperature is close to freezing, which leads to ice shapes with large chordwise extent. In hot-air systems, extensive spanwise variation is also possible due to the arrangement of the hot-air jets that provide the surface heat.

Runback icing is a potential problem in some phases of flight, such as holding and descent through icing conditions. Holding can increase the exposure time and can challenge the system if high water catch rates or very low temperatures are experienced. Descent can be critical because the engine power is reduced, and decreased mass flow and lower temperature air is provided to the system.

The ability to generate runback ice shapes in a ground testing facility has many advantages. First, it provides a cost-effective way to generate the geometrical characteristics of runback icing, which are not well documented in the public domain. This is despite the fact that thermal systems are widely used on most commercial aircraft and private jets. Second, the cost of certification could be greatly reduced by minimizing the number of flights required to certify a new system. Finally, aerodynamic testing of runback ice shapes is directly facilitated by ground testing through tracings and moldings of the accreted shapes.

1.1 REVIEW OF LITERATURE.

Data for the operation of hot-air, anti-icing systems, both in wind tunnels and in-flight, are not widely available in the public domain. Runback icing was investigated as early as 1953 when Gray and von Glahn [1] tested a National Advisory Committee for Aeronautics (NACA) 65_1-212 airfoil equipped with a hot-air, anti-icing system. Multiple runback accretions were documented and the aerodynamic penalties of the shapes were evaluated. Formation of a runback ridge aft of the heated region was found to cause substantial increases in drag. Other experiments have been conducted more recently to validate numerical models of runback icing and runback water. Most of these experiments used an electrothermal, rather than hot-air, system. Al-Khalil, et al. [2] conducted runback icing experiments with a NACA 0012 airfoil equipped with an electrothermal ice protection system. However, the focus was primarily on heat transfer and surface temperature distributions.

The process of scaling thermal systems is not well understood and is a focus of this research. Boeke and Paselik [3] concluded that the heat required by a thermal system increases with both airspeed (V) and density (ρ). Scaling thermal systems for sea-level testing requires that both icing parameters, such as liquid water content (LWC) and median volumetric diameter (MVD), and atmospheric parameters, such as temperature, be modified. Therefore, there is a delicate balance between thermodynamic, atmospheric, and aerodynamic scaling parameters that must be achieved to accurately reproduce runback shapes in icing facilities that cannot simulate altitude. Anderson [4] has applied ice accretion similarity relationships to both size and test condition scaling methods. The effect of altitude (ambient, static-air pressure) on unprotected ice shapes was found to be negligible in his calculations of the relevant similarity parameters. Tests in pressurized icing wind tunnels [5 and 6] have confirmed that static-air pressure has a negligible effect on unprotected ice shapes. In thermally protected surfaces, the relative importance of the similarity parameters is altered by the dominance of convective heat and mass transfer, which cause static-air pressure to have a substantial effect on the ice accretion. Anderson also stated that a rigorous pressure-scaling method could be devised from the similarity parameters shown to be important, but that it would need to be validated in a pressure-controlled icing tunnel before it could be recommended.

Testing the aerodynamic performance penalties of runback ice accretions is another aspect of the hot-air, anti-icing systems research at the University of Illinois. Studies by Jacobs [7], Lee, et al. [8], and others have clearly demonstrated the impact of ice shapes on aerodynamic performance. Lee, in particular, studied ridge shapes, although not necessarily runback ridges, and found dramatic loses in lift and increases in drag. Jacobs placed a k/c=0.005 spoiler at various chordwise positions on a 5-inch chord NACA 0012 at Reynolds number (Re)=3.1x10^6. His study was mostly concerned with the drag effects of manufacturing protuberances. He observed much more substantial reductions in maximum lift coefficient (C_{lmax}) for the same shape attached at x/c=0.05 (almost 50%) versus those attached at x/c=0.15 (less than 15%). Calay, et al. [9] simulated runback ridges using a step, a ramp, and a triangular shape, each with k/c=0.0035, on a NACA 0012 at Re=1.25x10^6 and found that drag increased up to 30% while C_{lmax} decreased up to 20%. He also found that the same shapes at x/c=0.15 increased the C_{lmax} of the airfoil. The greatest C_{lmax} increase was approximately 5%, and stalling angle of attack (α_{stall}) was delayed by 1 degree. Calay noted that the stall of the airfoil with the simulated ice shapes began from the ice shape rather than from the trailing edge, as is the case for the clean airfoil. He attributed the increase in C_{lmax} to the ice shape causing the flow to remain attached at greater angle of attack (α) than in the clean case. Calay concluded that small changes in the ice configuration were able to produce large changes in the performance effect requiring accurate simulations to estimate actual runback effects. Papadakis and Gile-Laflin [10] also observed increases in airfoil performance due to a backward facing ramp with k/c=0.0041 at x/c=0.15 and a spoiler with k/c=0.0053 at x/c=0.15. Their tests were conducted using a modified NACA 63_A213 airfoil at Re=2.0x10^6. The ramp increased C_{lmax} by 9% and delayed stall by 4 degrees. The spoiler increased C_{lmax} by 1% and delayed stall by 1 degree. Tests with the ramp at x/c=0.025 resulted in an 18% loss in C_{lmax} and a 2 degree reduction in stalling angle of attack.

1.2 OBJECTIVES AND APPROACH.

The Federal Aviation Administration (FAA) has initiated a research program to investigate runback ice accretions that result from the operation of hot-air, anti-icing systems. The overall objective of this program was to develop methods for investigating runback ice accretions on an airfoil with a thermal ice protection system. The detailed objectives of this program were:

- Investigate thermal ice protection system (IPS) runback ice shapes representative of in-flight ice shapes.

- Develop reliable scaling methods that permit investigations of thermal IPS runback ice accretions in unpressurized (atmospheric) icing wind tunnels.
- Observe and document characteristic features of runback accretions.
- Investigate the aerodynamic effects of runback ice accretions.

In collaboration with the National Aeronautics and Space Administration (NASA) Glenn and the Cessna Aircraft Company, the University of Illinois tested a typical business jet wing section equipped with a thermal (hot-air) IPS in the Icing Research Tunnel (IRT). The IRT model was a full-scale wing section representative of actual flight hardware. Representative cases that spanned the flight envelope and icing envelope of flight conditions considered critical relative to the formation of runback icing were chosen. Scaling methods were developed for ground testing to model the performance of the system at altitude.

Two testing campaigns were completed at the IRT. The first test, in September 2003, was used to evaluate the scaling methods that were developed based on matching the static temperature of the reference conditions and to explore the thermodynamics and icing physics of runback icing. The second test, in October 2004, explored a modified set of scaling methods, based on matching the total temperature of the reference cases. Sensitivity cases were also run to explore the sensitivity of the ice accretions to tunnel and bleed air temperature.

The aerodynamic effects of runback ice accretions were investigated using the Illinois 3- by 4-foot subsonic wind tunnel. Because of model size constraints, it was impossible to perform aerodynamic testing on the wing model used for the ice accretion testing. Further, programmatic and funding issues (1) prohibited any full-scale model aerodynamic testing in another facility and (2) limited the choice of airfoil models that could be used for the aerodynamic testing to those that were already available from other research programs. Therefore, airfoils representative of the business jet thermal model, in terms of pressure distribution at selected lift coefficients (C_l), were chosen for the Illinois wind tunnel tests. These airfoils were the NACA 23012 and NACA 3415. The choice of these airfoils did not compromise the objective of evaluating the aerodynamic effect of the runback ice accretions.

The full-scale ice accretions generated during the IRT testing were scaled to the model size used in the Illinois tunnel. The scaled shapes were constructed out of simple, basic materials such as sections of balsa and grit roughness. These components were combined to simulate the three-dimensional (3-D) character of the runback ice from measurements and observations of the accretions obtained during testing at the IRT.

The results of both the icing and aerodynamic tests were published in 2005 by Whalen, et al. [11], Following that, two-dimensional (2-D) ice shape simulations were studied to examine a range of ridge heights and locations as well as the need for accurate simulation of the runback ice features. During these tests, a phenomenon was observed in which α_{stall} and C_{lmax} increased with the addition of certain runback ice shape simulations. These tests were conducted at below full-scale Reynolds number with ice shape simulations at aft x/c locations, relative to typical ice accretions. Therefore, the boundary layer was relatively thick, compared to the ice shape simulation height, and scaling was a concern. To address these topics, the calculated boundary-layer thickness was used to scale the runback ice shape simulations and their effects were documented. The results from those investigations were published in 2006 [12]. This report further describes the results of both the ice accretion and aerodynamic test campaigns.

2. ICE ACCRETION TESTS.

The ice accretion tests were carried out to address the first three objectives of this program as described in section 1.2. The selected approach was to employ a test article that was essentially equivalent to flight hardware. That is, the full-scale wing section was equipped with a hot-air, anti-icing system typical of flight hardware. The objectives of this work then focused on how to account for differences in static pressure at a given flight condition relative to the static pressure in the icing tunnel. This was determined to be critical to the goal of producing runback ice accretions that were representative of those observed in flight. A complete record of the IRT runs conducted as part of this program is presented in appendix A. This section describes in more detail the icing facility and model, as well as the simulated flight conditions and the scaling methods employed. Finally, the key results of the ice accretion testing are presented.

2.1 FACILITY AND MODEL.

Ice accretion tests were performed in the NASA Glenn IRT. The IRT is an atmospheric, closed return-type icing wind tunnel capable of maintaining temperatures from freezing to -22^{o}F at speeds up to 350 knots. Supercooled water droplets can be produced with MVD between 10 and 300 µm, with LWC from 0.5 to 2.5 g/m^3. The test section dimensions are 6 feet tall by 9 feet wide by 20 feet long.

The full-scale model, provided by NASA, was a representative business jet wing section equipped with a hot-air, anti-icing system. The model had a span of 72 inches, a root chord of 66.82 inches, and a tip chord of 55.4 inches. The model was mounted vertically in the test section, and the angle of attack was controlled by rotating the turntable in the test section floor. Figure 1 is a photograph of the model installed in the IRT. The piccolo tube that supplied the hot air to the leading edge entered through the floor of the tunnel and exhausted into the test section at the ceiling. The hot air was delivered from an external source to the model leading edge through jets arranged in a diamond pattern along the length of the piccolo tube. The diamond pattern was created by aiming a single jet at the leading edge, followed by two jets offset at $\pm 45^{o}$ and then another single jet again aimed at the leading edge. The spanwise spacing of the jets (the distance from a $\pm 45^{o}$ pair of jets to a single leading-edge jet) was 6.6 cm (~2.5 inches). Both the mass flow rate and the temperature of the hot air were adjustable. The model was designed to maintain choked jet flow down to very low flow rates, which was important for near sea-level testing. The heated region extended to $x/c=0.08$ on the suction and pressure surface. A cross section of the leading edge is shown in figure 2. The heated region of the model was extended to $x/c=0.08$ by a diffuser positioned behind the piccolo tube that acted to concentrate the hot-air flow near the skin and direct it to an exhaust manifold. Thermocouples were installed on the inside of the skin at 30 and 42 inches from the tunnel floor. Thirteen thermocouples were installed at each of those stations to monitor surface temperatures back to $x/c=0.08$ on the suction and pressure surface.

Figure 1. Representative Business Jet Thermal Model Installed in the IRT

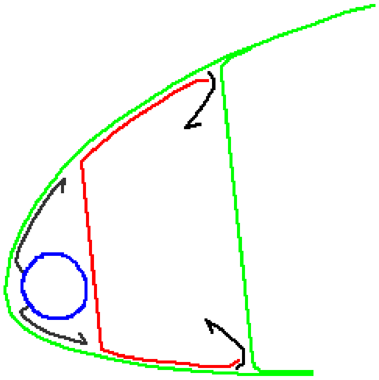

Figure 2. Cross Section of the Model Leading Edge Showing the Piccolo Tube and Diffuser With Airflow Path Indicated

During each IRT test run, data were collected to fully document the process of runback ice formation. The ESCORT data system collected tunnel and icing data, thermal system mass flow, and temperature, as well as the temperatures from thermocouples imbedded in the heated portion of the wing. Infrared (IR) video of the black region of the leading edge (figure 1) was taken at the beginning and end of each icing spray. High-definition video was used to document the formation of the ice shapes. Following each run, photographs were taken of the model's suction surface, pressure surface, and leading edge. Tracings were made at three spanwise locations: 31, 36, and 44 inches from the test section floor. Ice heights were also measured at the tracing locations. Molds of the ice accretion were made after the final run of most test days. Seven molds were made during the 2003 test, and one mold was made during the 2004 test. The molds and resulting castings were produced purely for documentation purposes. While costly to produce, they are considered the highest-fidelity method of recording ice accretion characteristics.

2.2 REFERENCE CONDITIONS.

Three flight regimes, identified as critical to the thermal system operation and runback icing formation, were selected for this investigation. Table 1 presents the reference conditions for each of these cases. Holding at near-freezing temperatures, the warm-hold condition was critical to the system operation because it generated the highest water catch rate based on Appendix C conditions. Holding at very cold temperatures (-22°F), the cold-hold condition, represented the largest temperature difference, based on Appendix C conditions, between the wing skin and the outside air. Descent was critical for the IPS due to reduced engine power, and therefore, reduced bleed air mass flow and temperature. In the warm- and cold-hold cases, the nominal IPS supply air temperature was 350°F, and the nominal unit mass flow rate was 0.01 lbm/s/ft. In the descent case, these values were reduced to 250°F and 0.005 lbm/s/ft, respectively. The bleed air temperature was set at the inlet to the piccolo tube, and the temperature decreased along the length of the system. For example, in the warm-hold case, the nominal supply air temperature fell to approximately 330°F at the exhaust. The IPS mass flow was normalized by the span, resulting in the per unit length in the mass flow units.

Table 1. Reference Conditions

Flight Condition	Alt. (ft/1000)	V (ktas)	α (deg)	T_s (°F)	T_0 (°F)	LWC (g/m^3)	MVD (µm)	h (Btu/hr/ft/°F)	K_0	RHF	m_w (lbm/hr/ft)	n_0
Warm Hold	15	205	3	20	30	0.50	20	91.3	0.033	0.048	4.36	0.18
Cold Hold	15	196	3	-22	-12	0.15	20	95.5	0.034	0.013	1.27	1.00
Descent	10	250	-1	-4	15	0.15	20	129.9	0.035	0.014	1.83	1.00

Alt. = altitude
V = airspeed
ktas = knots true airspeed
deg. = degrees
g/m^3 = grams per meter cubed
µm = microns
RHF = relative heat factor

2.3 THERMAL SCALING.

Parameters governing development of the runback ice accretion were scaled, using three different scaling methods for testing in the IRT. These scaling methods were designed to scale the external heat and mass transfer. The angle of attack and static temperature (T_s) or total temperature (T_o) from the reference conditions were used in the ground test. The relevant parameters in the scaling procedure were convective heat transfer coefficient (h), modified inertia parameter (k_0), water catch rate (m_w) and relative heat factor (RHF). Convective heat transfer coefficient was calculated, as a function of *Re* and Prandtl number (*Pr*), from a simple correlation for a flat plate turbulent boundary layer. The modified inertia parameter, as a function of the droplet Reynolds number and inertia parameter, was obtained from LEWICE [13]. The water catch rate was also calculated using the total collection efficiency obtained from LEWICE. The RHF is the ratio of the product of m_w and the specific heat of water to h. Finally, the stagnation point freezing fraction (n_0) was calculated using LEWICE for the model without the thermal IPS operating. It was considered as a scaling parameter but was not examined until after the test campaigns.

Three scaling methods were developed by matching various combinations of these parameters to their reference condition values. For clarity, the methods were named based upon the parameters that were matched to the reference condition values. The three methods were: h, k_0, RHF; k_0, RHF; and k_0, m_w. The h, k_0, RHF scaling method was designed to match all the parameters that were thought to be important to the scaling of this problem. Anderson [14] has done a thorough evaluation of scaling methods for icing problems; the basis for the selection of these parameters arose from his work. Other parameters have been suggested in recent studies, mostly having to do with water film dynamics. Since little was known about the influence of film dynamics on runback ice accretion scaling, the current set of scaling parameters was adopted. The h, k_0, RHF method incorporated each parameter that was considered important to scaling the problem. The second and third methods were subsets of that method. The k_0, RHF scaling method was simpler and less restrictive for testing, because the explicit use of the convective heat transfer parameter was removed. The k_0, m_w scaling method was also simpler and less restrictive for testing, because the convective heat transfer was completely removed from the scaling method, and replaced RHF with m_w.

The details of the scaling procedure are described for the warm-hold case. The reference and scale conditions are given in table 2. The reference conditions are identical to those in table 1 and were based on the flight condition simulated in the IRT. The h, k_0, RHF-scaled case attempts to match all the parameters. An inspection of table 2 shows that the scale values are not identical to the reference values, but are within about 4%. The main reason for this discrepancy was that the variation in the IRT static pressure with velocity was not taken into account prior to testing. So, the initial calculations were performed assuming that the tunnel static pressure was standard sea-level pressure (14.7 pounds per square inch absolute (psia)). The values shown in table 2 were calculated at the completion of the test, using the measured static pressure in the IRT test section. So, for an airspeed of 115 ktas, the test section static pressure was 14.08 psia, corresponding to about 1200-ft altitude in the standard atmosphere.

Table 2. Warm-Hold-Scaled Conditions

Scaling Method	Alt. (ft/1000)	V (ktas)	T_s (°F)	T_0 (°F)	LWC (g/m^3)	MVD (μm)	h (Btu/hr/ft/°F)	K_0	RHF	m_w (lbm/hr/ft)	n_0
Reference	15	205	20	30	0.50	20	91.3	0.033	0.048	4.36	0.18
h, k_0, RHF	1.2	115	20	23	0.87	29	87.8	0.034	0.050	4.41	0.35
k_0, RHF	1.8	154	20	26	0.82	26	109.1	0.034	0.051	5.58	0.25
k_0, m_w	2.0	168	20	27	0.60	25	116.3	0.034	0.038	4.46	0.28

Determining the scale conditions for the h, K_0, RHF method required several steps:

a. Select scale temperature, either T_s or T_0: The choice of temperature was made first because it affected the evaluation of fluid properties such as the thermal conductivity (k_0) and viscosity (μ). For this example, in table 2, the static temperature was matched to the reference condition.

b. Determine the scale velocity: Scale velocity was calculated such that the reference and scale convective heat transfer coefficients were matched. The correlation for the local convective heat transfer coefficient for a flat plate, turbulent, boundary layer, described in terms of the nondimensional Nusselt number (Nu), was taken from Chapman [15].

$$Nu = \frac{hc}{k_0} = 0.0296 Re^{0.8} Pr$$

In this case, the Prandtl number was taken as a constant for air (0.72). The parameter k_0 is the thermal conductivity of air. The Reynolds number was calculated in the usual way, based on the model chord length.

$$Re = \frac{\rho V c}{\mu}$$

$$\rho = \frac{p}{RT}$$

These equations imply that the local values of Nu and h were calculated at x=c, that is, at the trailing edge of a flat plate with chord length c. What is important about the use of these equations is not the absolute value of h, but that the proper variation with Reynolds number is captured. Determining the actual value of the local heat transfer coefficient, or an integrated value in the region of the leading-edge impingement area, would be much more difficult. This scaling method assumes that h varies as Reynolds number raised to the 0.8 power. Further, it was also assumed that the mass transfer effects governing the evaporation of the surface water were scaled equivalently with h.

Table 2 shows that the airspeed was reduced to 115 ktas from 205 ktas to account for the increase in static pressure between 15,000 and 1,200 ft. As shown in these equations, this was manifest through the density change in the Reynolds number.

c. Determine the scale value of k_0: The decrease in velocity required to match the heat transfer coefficient resulted in a mismatch of the modified droplet inertia parameter, k_0. This was accounted for by increasing the droplet MVD in the scale condition. LEWICE was used to calculate k_0. As shown in table 2, the MVD was increased to 29 μm from 20 μm to account for the reduction in velocity.

d. Determine the scale value of LWC: The last step in the scaling process involved increasing the LWC to match the water catch rate,

$$m_w = LWC \cdot V \cdot \Delta Y_0 \cdot c$$

where ΔY_0 is the total collection efficiency times the projected height of the airfoil at angle of attack. The total collection efficiency was calculated using LEWICE. Table 2 shows that the scale LWC was increased to 0.87 g/m^3 from the reference value of 0.50 g/m^3. This increase was required due to the decrease in velocity determined in step a.

In the h, k_0, RHF method, matching h and m_w implies that the RHF is matched, since RHF is simply the ratio of m_w times the specific heat of water to h. So, it would be equivalent to say that h, K_0, and m_w are matched, or that h, k_0, m_w and RHF are matched.

The other scaling methods (k_0, RHF and k_0, m_w) in table 2 were simply subsets of this process. In these cases, the heat transfer coefficient was not matched at all. Each of the three scaling methods was tested for the warm-hold case to evaluate their ability to generate ice accretions that were representative of in-flight accretions. It was expected that the h, k_0, RHF method would generate the most realistic runback shapes. The extra freedom afforded by the other two methods created added flexibility in the run conditions and allowed for the evaluation of the importance of the various scaling parameters. Since the h, k_0, RHF method matched all the parameters, it was used for a majority of the icing runs. The angle of attack and static temperature or total temperature from the reference conditions were used in the ground test. Both static and total temperatures could not be matched, because the airspeeds dictated by the scaling methods were substantially lower than the reference case.

2.4 SCALED ICING RESULTS USING MATCHED STATIC TEMPERATURE.

2.4.1 Appendix C Warm-Hold Case.

Table 2 presents the test conditions for the warm hold-case for each scaling method. This case was used to explore each scaling method as well as the effect of changes in IPS operating parameters, air temperature, and mass flow rate. Mass flow rates of 0.005, 0.01, 0.015, 0.02, 0.03, and 0.04 lbm/s/ft at a bleed air temperature of 350°F were tested as well as bleed air temperatures of 250°, 275°, 300°, 325°, and 350°F at a mass flow rate of 0.01 lbm/s/ft. As expected, reducing the IPS operating parameters resulted in larger ice shapes farther upstream on the model. In some cases, increased hot-air, mass flow rates resulted in 100% evaporation and no ice accumulation.

Accretion heights varied widely across both span and among runs at the same conditions. Table 3 presents the measurement data for four warm-hold runs, carried out at the same conditions, using the h, k_0, RHF scaling method. The maximum height at the three tracing stations (31, 36, and 44 inches) on the suction and pressure surface was recorded. Spanwise variation in the runback ridges was observed for all flight conditions. However, the repeatability of the chordwise ridge location and average ridge height was good. Multiple factors contributed to the spanwise variation of the ridge height. The surface temperature distribution was not uniform owing to the offset pattern of the piccolo tube jets. In addition, the temperature of the hot air varied along the span of the piccolo tube. Because the model geometry varied along the span, things such as collection efficiency could be expected to vary along the span as well. The painted IR surface near station 44 had different surface properties than the polished aluminum surface on the remainder of the leading edge. Because the formation of the ridge is dependent on the liquid rivulets flowing back to the ridge, the surface quality can greatly affect the formation, path, and coalescence of the rivulets. Although they are small, especially in Appendix C cases, spatial variations in the icing cloud could have contributed to the measurement differences. Finally, the measurements presented in table 3 are point measurements in a ridge with spanwise variation, so that the action of any of these effects could result in the variability recorded.

Table 3. Variation in Measured Runback Ridge Height From Repeat Runs at the Same Conditions

	Suction Surface Maximum Height (in.)			Pressure Surface Maximum Height (in.)		
Run	Sta. 31	Sta. 36	Sta. 44	Sta. 31	Sta. 36	Sta. 44
1	0.23	0.23	0.32	0.86	0.73	0.64
2	0.14	0.23	0.10	0.68	0.97	1.14
3	0.16	0.26	0.07	0.51	0.39	0.85
4	0.16	0.17	0.38	0.41	0.41	1.36

Sta. = station

This portion of the report will focus on the results with the system running at nominal operation, that is, a mass flow rate of 0.01 lbm/s/ft and a temperature of 350°F. Figure 3 is a tracing of the runback ice accretion that resulted from the use of the h, k_0, RHF scaling method (table 2) with nominal IPS operation. The end of the heated region is indicated by the section marking labeled Heated Region and the end of the polished aluminum region on the suction and pressure surface is indicated by the section markings labeled Polished Aluminum. The polished aluminum region can clearly be seen in figure 1 and is also accurately represented in figure 2 by the extents of the wing skin on the suction and pressure surface. The spray time for the run was 22.5 minutes.

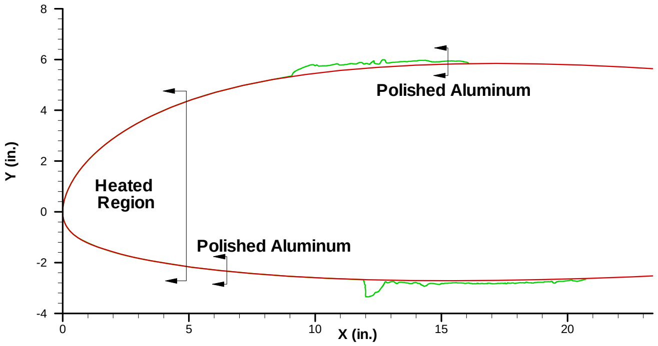

Figure 3. Tracing of a Warm-Hold Runback Accretion After a 22.5-Minute Spray, Using the *h*, K_0, RHF Scaling Method

Figure 4 is a close-up photograph of the accretion on the suction surface of the model. Note that the frozen rivulets were almost entirely confined to the polished aluminum region. The frozen rivulets tended to breakup at the seam at the end of the polished aluminum region and then reappear downstream, but were smaller and less dense than those forward of the seam (figure 5). The height of the suction surface accretion along the span varied between 0.23 and 0.32 inch while the pressure surface accretion height was between 0.64 and 0.86 inch. These ranges are based on measurements of the maximum ice thickness at each tracing station. On the suction surface, the ridge had a rough texture that was followed by smooth, densely packed frozen rivulets that terminated at the seam of the polished aluminum. Sparse, small frozen rivulets were observed downstream of the polished aluminum seam. The pressure surface accretion had a well-defined ridge as well, but was very rough and exhibited extensive spanwise variation on large and small scales (figure 6). The ice accretions that resulted from the *h*, k_0, RHF scaling method were found to be representative of reference accretions based on experience with in-flight runback accretions by collaborators that participated in the investigation. However, it is not possible to make a conclusion as to the validity of this scaling method without close comparison to runback ice accretions obtained at several reference conditions.

Figure 4. Close-Up Photograph (Suction Surface) of a Warm-Hold Runback Accretion After a 22.5-Minute Spray, Using the h, k_0, RHF Scaling Method (flow from right to left)

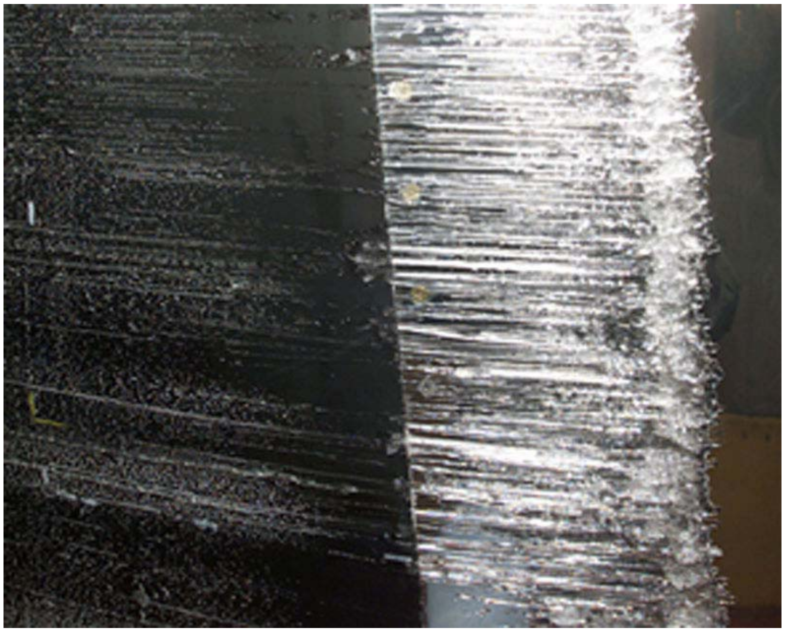

Figure 5. Overall Photograph (Suction Surface) of a Warm-Hold Runback Accretion After 22.5-Minute Spray, Using the h, k_0, RHF Scaling Method (flow from right to left)

Figure 6. Overall Photograph (Pressure Surface) of a Warm-Hold Runback Accretion After a 22.5-Minute Spray, Using the *h*, k_0, RHF Scaling Method (flow from left to right)

2.4.2 Supercooled Large Droplet Warm Hold Case.

Table 4 presents the reference and scaled (*h*, k_0, RHF scaling method) parameters for holding in supercooled large drop (SLD) icing conditions at near-freezing temperatures. In this case, the MVD and LWC were selected based on a calibrated SLD operating point for the IRT. To establish the reference condition, the LWC and MVD that corresponded to the calibrated point were calculated. With nominal IPS operation, the character of the ice was not unlike the Appendix C accretions. On the suction surface of the model, a well-defined ridge formed on the polished aluminum region with dense frozen rivulets extending to the seam of the leading edge (figure 7). The SLD ridge appeared to have a smoother texture overall than the Appendix C warm-hold ridge. The overall height of the suction surface accretion measurements varied similarly to that seen in table 3. However, the character of the shape was quite different.

Table 4. Warm-Hold SLD Conditions

Scaling Method	Alt. (ft/ 1000)	*V* (ktas)	T_s (°F)	T_0 (°F)	LWC (g/m^3)	MVD (μm)	*h* (Btu/hr/ft/°F)	I_0	RHF	m_w (lbm/ hr/ft)	n_0
Reference	15	205	20	30	0.32	93	91.3	0.361	0.131	11.92	0.17
h, K_0, RHF	1.2	115	20	23	0.57	133	87.8	0.355	0.136	11.97	0.33

The Appendix C ridge consisted of large chunks that appeared periodically on a shorter ridge, while the SLD ridge was taller with periodic valleys along the span. Figure 8 is a photograph of the pressure surface taken at an angle that better reveals the structure, rather than taken from directly above like the other photographs. The ridge appeared to be similar to that seen in the Appendix C warm-hold case. However, the large-scale features of the ridge developed from the formation of nodules that froze together to form the ridge. The ridge was followed by more nodules and some small frozen rivulets.

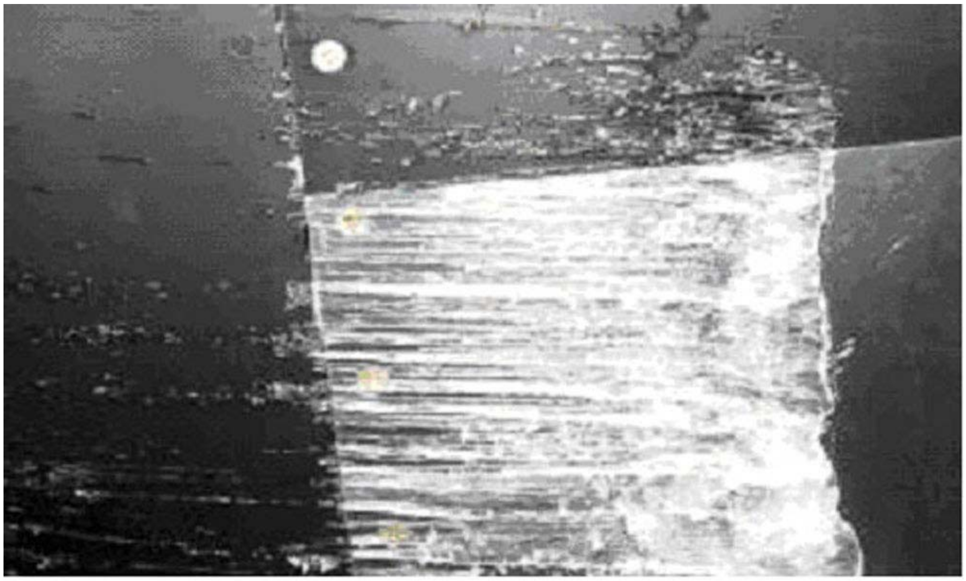

Figure 7. Close-Up Photograph (Suction Surface) of a Warm-Hold SLD Runback Accretion After a 22.5-Minute Spray, Using the *h*, k_0, RHF Scaling Method (flow from right to left)

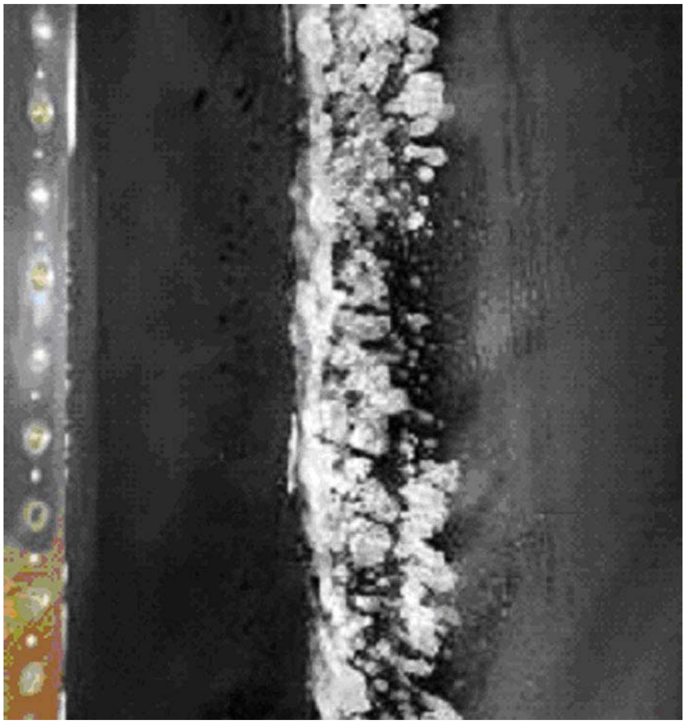

Figure 8. Close-Up Photograph (Pressure Surface) of a Warm-Hold SLD Runback Accretion After a 22.5-Minute Spray, Using the *h*, k_0, RHF Scaling Method (flow from left to right)

2.4.3 Appendix C Cold Hold Case.

The scaling parameters for the Appendix C cold-hold conditions are shown in table 5. The cold hold is a critical runback icing and IPS design condition due to the large temperature difference between the ambient air and the exposed IPS skin surface. Again, only the h, k_0, RHF scaling method was tested. The low static temperature proved to be a critical condition for the system, as was predicted. The scaled LWC for the cold-hold runs was outside the calibrated operating envelope of the IRT at the scaled airspeed. To account for this limitation, the LWC was set at the IRT minimum for that airspeed, and the spray time was scaled by the ratio of the scaled LWC to the IRT minimum LWC. For instance, the scaled LWC for the cold hold was 0.26 g/m^3 and the minimum LWC of the IRT at the scaled airspeed was 0.69 g/m^3, so the spray time was reduced by a factor of 0.38 (i.e., 0.26/0.69). This changed the spray time for the cold-hold runs from 22.5 to 8.6 minutes.

Table 5. Cold-Hold Conditions

Scaling Method	Alt. (ft/ 1000)	V (ktas)	T_s (^{o}F)	T_0 (^{o}F)	LWC (g/m^3)	MVD (µm)	h (Btu/hr/ft/^{o}F)	k_0	RHF	m_w (lbm/ hr/ft)	n_0
Reference	15	196	-22	-12	0.15	20	95.5	0.034	0.013	1.27	1.00
h, k_0, RHF	1.3	110	-22	-19	0.26	29	94.3	0.034	0.013	1.26	1.00

Significant rime ridges with extensive spanwise variation were observed at nominal IPS operation. Figure 9 is a tracing of a cold-hold accretion and figure 10 is a close-up photograph of the suction surface. Periodic accumulations that occurred along the ridge, one visible near the bottom of figure 10, were due to the proximity of the ridge to the jet impingement zones and were observed to grow up to approximately 0.4 inch high. This was characteristic of the accretions at the cold-hold temperature. The pressure surface (figure 11) had a more consistent structure of wide, flat, or slightly rounded regions separated by sharp valleys (in the chordwise direction) that acted as accumulation points for incoming water, evident from the increased ridge height in the area of the valleys. The structure of the ridge on the pressure surface was far more regular than that on the suction surface. Note that the distance between the screws that secure the leading edge was 2 inches on center. Also, the piccolo tube jets were spaced 6.6 cm (~2.5 inches) apart. Looking at figure 11, it is apparent that the valleys (spaced approximately 5 inches apart) were likely due to the two jets at ±45^o expanding the heated area in the chordwise direction. Ice accumulated, in the area of the valleys, to over 0.6 inch thick in some cases. The flat areas correspond to the single jet's effect. A similar phenomenon was observed in the descent case as well. At lower bleed air temperatures and mass flow rates, the leading edge of the model was covered with ice. However, small holes did remain at the locations of jet impingement.

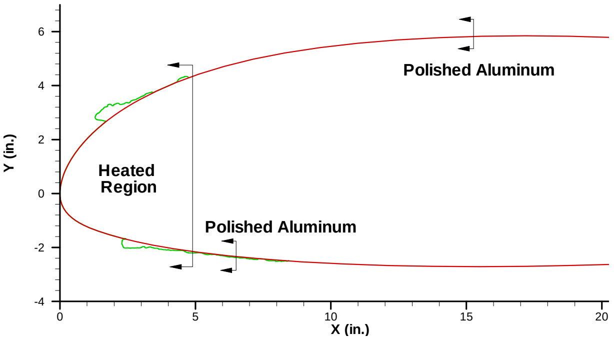

Figure 9. Tracing of a Cold-Hold Runback Accretion After an 8.6-Minute Spray, Using the *h*, k_0, RHF Scaling Method

Figure 10. Close-Up Photograph (Suction Surface) of a Cold-Hold Runback Accretion After an 8.6-Minute Spray, Using the *h*, k_0, RHF Scaling Method (flow from right to left)

Figure 11. Overall Photograph (Pressure Surface) of a Cold-Hold Runback Accretion After an 8.6-Minute Spray, Using the h, k_0, RHF Scaling Method (flow from left to right)

2.4.4 Descent Case.

The reference and scaled descent parameters are presented in table 6. The descent is a critical runback icing and IPS design condition, due to reduced availability of bleed air for the IPS and the lower temperature of the available bleed air at reduced engine power levels required for descent. The IPS was operated at a unit mass flow of 0.005 lbm/s/ft and a supply air temperature of 250°F. The baseline spray time was 3.25 minutes, based on a 6500-foot descent at 2000 ft/min. However, the minimum LWC at the scaled airspeed was 0.40 g/m^3, and the scaled LWC was 0.21 g/m^3 (table 6). Therefore, the LWC was set at the minimum for the scaled airspeed and the spray time was scaled by a factor of 0.52 (i.e., 0.21/0.4) to 1.7 minutes.

Table 6. Descent Conditions

Scaling Method	Alt. (ft/ 1000)	V (ktas)	T_s (°F)	T_0 (°F)	LWC (g/m^3)	MVD (µm)	h (Btu/hr/ft/°F)	k_0	RHF	m_w (lbm/ hr/ft)	n_0
Reference	10	250	-4	15	0.15	20	129.9	0.035	0.014	1.83	1.00
h, k_0, RHF	2.5	194	-4	5	0.21	25	133.2	0.038	0.016	2.12	1.00

The suction surface ridge height was comparable to that seen in the warm-hold case, between 0.2 and 0.25 inch. However, the location of the ridge was at approximately x/c=0.01 (figure 12). The pressure surface ridge formed around x/c=0.015 but was less than 0.1 inch in height (figure 12). Because of the reduced IPS supply air temperature and mass flow, the ice ridge forward, where variations on the IPS surface were the greatest, caused the sinusoidal variation in the ridge location (figures 13 and 14). In this case, the valleys were spaced approximately 2.5 inches apart, corresponding to the locations of the jets. The lack of variation in the amplitude of the oscillation was likely due to the low system operating parameters and cold-air temperature. The cold-air temperature resulted in no frozen rivulets; the ice following the ridge had the character of frost. The pressure surface accretion was similar to the suction surface. However, there was less frost or other ice surrounding the ridge.

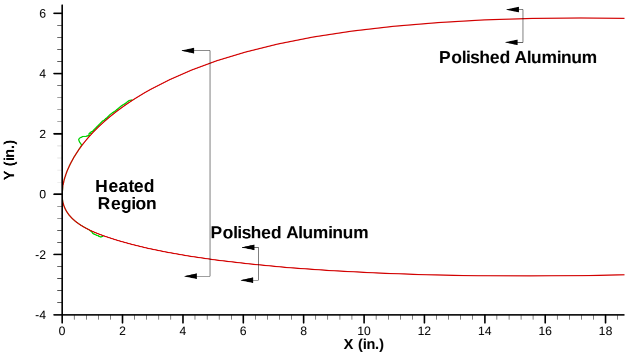

Figure 12. Tracing of a Descent Runback Accretion After a 1.7-Minute Spray, Using the h, k_0, RHF Scaling Method

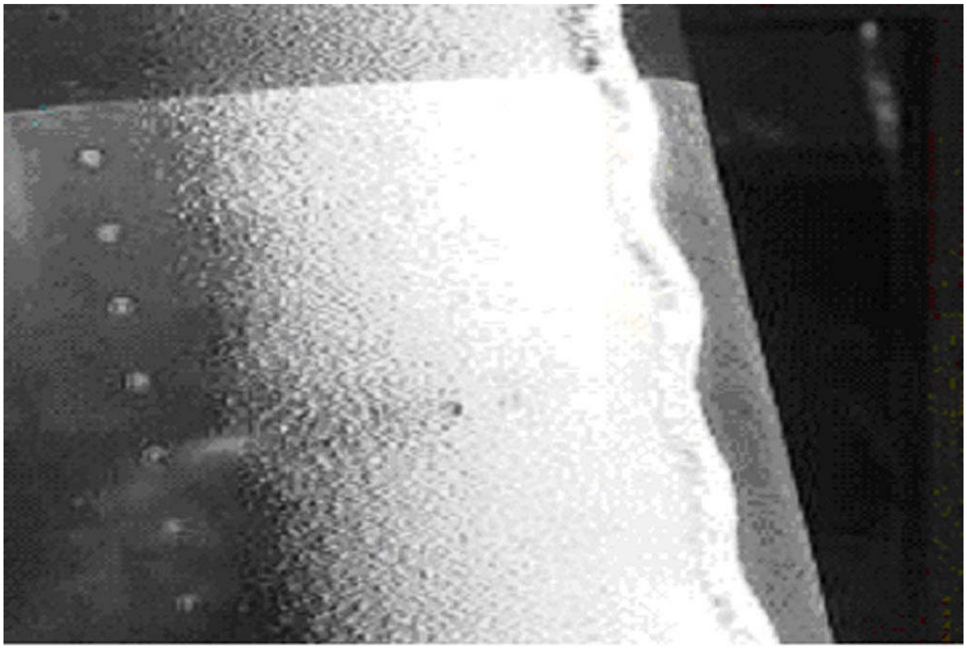

Figure 13. Close-Up Photograph (Suction Surface) of a Descent Runback Accretion After a 1.7-Minute Spray, Using the h, k_0, RHF Scaling Method (flow from right to left)

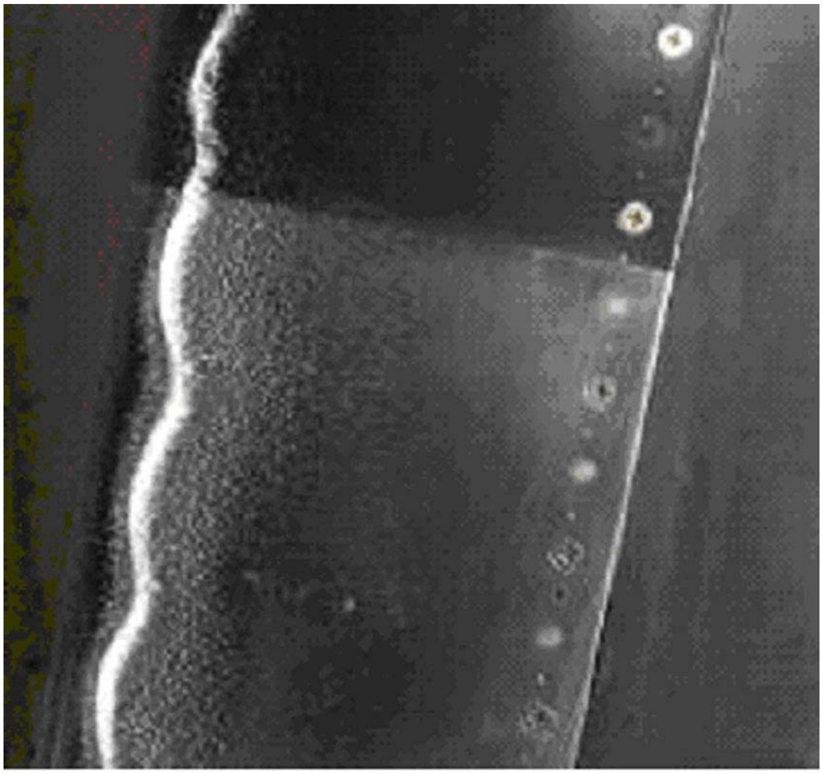

Figure 14. Close-Up Photograph (Pressure Surface) of a Descent Runback Accretion After a 1.7-Minute Spray, Using the h, k_0, RHF Scaling Method (flow from left to right)

2.5 SCALED ICING RESULTS USING MATCHED TOTAL TEMPERATURE.

Matching the total temperature of the scaled icing test to the reference condition was explored for the warm-hold case after reviewing the results of the 2003 tests. Because the airspeed had to be reduced to match the convective heat transfer coefficient of the reference case, the scaled total temperature was substantially less than in the reference case. For the h, k_0, RHF scaled warm-hold case, the total temperature was 23.0° versus 30.0°F for the reference case. Furthermore, total temperature was found to have an effect on the ice ridge location and size.

Table 7 presents the variation of ridge location and average height for a range of total temperatures using the h, k_0, RHF scaling method (table 2). A T_0 of 23.0°F corresponded to the matched static temperature case, while 30.0°F corresponded to the matched total temperature case. Photographs and run conditions for each of the cases presented in table 7 can be found in appendix B. Static temperature did not significantly affect the scaling parameters (table 8), so the tunnel conditions were held constant at the values set by scaling at matched static temperature. The ridge height on the suction surface increased with total temperature until 28.5°F, where it sharply declined to less than the height in the static temperature-scaling case. The ridge location moved steadily aft with increasing total temperature. Clearly, the runback ice accretion was very sensitive to the choice of the temperature on which the scaling method was based.

Table 7. Effect of Total Temperature Variation on Ridge Location and Height

		Suction Surface		Pressure Surface	
T_s (^oF)	T_0 (^oF)	Avg. Ice Height (in.)	Ridge Location (x/c)	Avg. Ice Height (in.)	Ridge Location (x/c)
19.9	23.0	0.21	0.15	0.66	0.23
21.9	25.0	0.36	0.19	0.36	0.28
23.8	27.0	0.36	0.30	0.25	0.34
25.4	28.5	0.13	0.40	**	0.60*
26.8	30.0	**	0.50*	**	0.80*

* Accretion aft of tracing, estimated

** Accretion aft of tracing, no measurement

Table 8. Comparison of Scaling Methods Based on Total and Static Temperature

Scaling Method	V (ktas)	T_s (^oF)	T_0 (^oF)	LWC (g/m^3)	MVD (mm)	h (Btu/hr/ft/^oF)	k_0	RHF	m_w (lbm/hr/ft)	n_0
Reference	205	20	30	0.50	20	91.3	0.033	0.05	4.41	0.18
h, k_0, RHF (T_s)	115	20	23	0.87	29	87.8	0.034	0.05	4.52	0.35
h, k_0, RHF (T_0)	115	27	30	0.87	28	87.3	0.034	0.05	4.49	0.10

Table 8 compares the tunnel conditions for the h, k_0, RHF scaling method based on static and total temperature. The tunnel conditions were not significantly affected by the change in the temperature. However, the stagnation freezing fraction of the model was calculated to be 0.10 in the total temperature-scaled case versus 0.35 in the static temperature-scaled case. The result of this is seen in figure 15, a photograph of the suction surface of the model after a 22.5-minute spray at the conditions set by the total temperature scaling. As seen in figure 15, water did not begin to freeze on the model until x/c=0.50 on the suction surface and x/c=0.80 on the pressure surface. A plot of the surface temperature, as measured by thermocouples attached to the inside of the polished aluminum skin, for the two cases is presented as figure 16. Negative s/c values correspond to the pressure surface, and positive s/c values correspond to the suction surface. The temperature at the piccolo tube jet stagnation zone was approximately 0.5^{o}F warmer in the total temperature-scaling case. At the limits of the heated region, the temperature difference grew to 4 degrees on the pressure surface and 6 degrees on the suction surface.

Figure 15. Photograph of the Suction Surface (Trailing-Edge Region) for the Warm-Hold Case With Matched Total Temperature (flow from right to left)

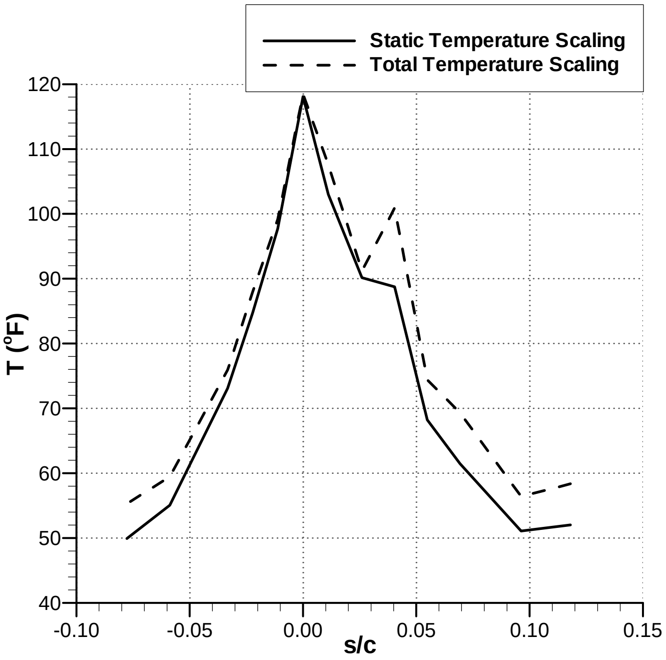

Figure 16. Thermocouple Surface Temperature Data for the Static and Total Temperature Scaling of the Warm-Hold Case

The run conducted at a total temperature of 28.5°F best matched the stagnation freezing fraction of the reference case. The freezing fraction of that case was 0.16 versus 0.18 for the reference case. The suction and pressure surface accretion (figures 17 and 18) exhibited dense rivulets that had large chordwise extent. There was no distinct ridge as was seen in the matched static temperature case. Comparing the two ice accretions, it can be seen that the ridge formed farther aft on the model in the matched freezing fraction case, corresponding to a total temperature of 28.5°F, than in the matched static temperature case corresponding to a total temperature of 23.0°F (table 7). In addition, the data show that the average height of the accretion was shorter on both the suction surface and the pressure surface than in the matched static temperature-scaled case. Testing in an icing tunnel capable of altitude simulation is necessary to understand the role of temperature in the scaling process as well as to acquire reference ice accretions for comparison.

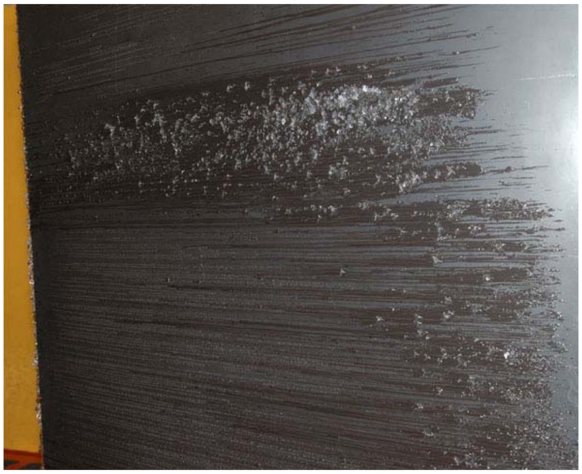

Figure 17. Suction Surface Ice Accretion Following a 22.5-Minute spray at Warm-Hold Conditions and a Total Temperature of 28.5°F (flow from right to left).

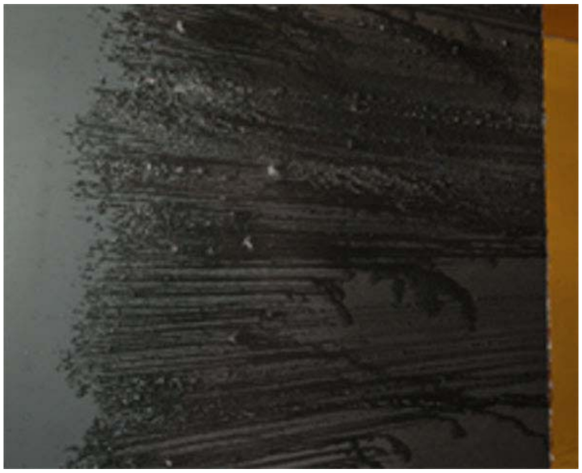

Figure 18. Pressure Surface Ice accretion Following a 22.5-Minute Spray at Warm-Hold Conditions and a Total Temperature of 28.5°F (flow from left to right).

2.6 SENSITIVITY TO HOT-AIR SETTINGS.

Sensitivity analyses of the runback ice ridge relative to IPS operating conditions were conducted at warm-hold conditions using the h, k_0, RHF scaling method. Table 9 presents the sensitivity of the ridge to the bleed air temperature. Two temperatures, 250°F and 350°F, were tested. The higher bleed air temperature caused the ridge to form farther aft on the model on both the suction and pressure surface. The maximum height on the pressure surface was approximately 34% shorter at the higher bleed air temperature, and the suction surface maximum ice height was slightly taller. Table 10 shows the variation of maximum ice ridge height and ridge location with the mass flow rate of the bleed air at a bleed air temperature of 350°F. Table 6 shows that the ice ridge became shorter and moved farther aft as the mass flow rate was increased. The height was approximately halved between 0.005 and 0.015 lbm/s/ft. Recall that 0.01 lbm/s/ft was the nominal mass flow rate for the warm-hold case.

Table 9. Sensitivity of a Warm-Hold Runback Ridge to the Bleed Air Temperature

Bleed-Air Temperature (^oF)	Average Suction Surface Maximum Height (in.)	Average Pressure Surface Maximum Height (in.)	Suction Surface Ridge Location (x/c)	Pressure Surface Ridge Location (x/c)
250	0.21	1.12	0.13	0.13
350	0.26	0.74	0.16	0.20

Table 10. Sensitivity of a Warm-Hold Runback Ridge to the Bleed Air Mass Flow Rate

Mass Flow (lbm/s/ft)	Average Suction Surface Maximum Height (in.)	Average Pressure Surface Maximum Height (in.)	Suction Surface Ridge Location (x/c)	Pressure Surface Ridge Location (x/c)
0.005	0.40	1.07	0.13	0.14
0.01	0.26	0.74	0.16	0.20
0.015	0.22	0.51	0.20	0.28

3. AERODYNAMIC TESTS.

As described in section 1.2, a primary objective of this program was to evaluate the aerodynamic performance effects associated with the runback ice accretions observed in the icing tests. In the ideal scenario, it would have been possible to take the ice castings produced in the icing tests and apply them to an equivalent full-scale, aerodynamic model to obtain high-quality and high-Reynolds number performance data. However, several programmatic and funding issues limited the options for assessing the aerodynamic effects of runback ice. Therefore, the performance tests were conducted at the University of Illinois, low-speed, low-turbulence facility. These factors also limited the choice of airfoil models to those already available from previous research programs.

This section describes the resulting methodology in terms of airfoil selection and ice accretion simulation. The airfoils selected were representative of the section used in the icing tests. The simulated ice shapes allowed for parametric variation of ridge height and chordwise location. It is important to note that the objective of investigating the aerodynamic effects of runback ice was not compromised by this methodology. In fact, it is often true that more insight into aerodynamic effects can be gained through parametric studies. In some ways, this work is an important precursor to more expensive, full-scale research.

3.1 FACILITY AND MODELS.

Aerodynamic tests of simulated runback ice accretions were conducted in the Illinois 3- by 4-foot subsonic wind tunnel. The Illinois tunnel is an open-return tunnel that is exhausted into the tunnel room. The inlet is equipped with a honeycomb flow straightener followed by four antiturbulence screens. The contraction ratio between the inlet and the test section is 7.5 to 1. Airspeed is set using a variable frequency drive that controls a 125 horsepower motor. The motor, in turn, drives a five-bladed fan. The empty test section maximum speed of the tunnel is 160 miles per hour or 235 ft/s, corresponding to a Reynolds number of 1.5 million per foot. The fan is followed by an acoustic silencer.

A three-component force balance was used to measure the lift and pitching moment of the model, and the integrated turntable was used to set the angle of attack. Drag was measured using a wake rake. The force balance was located below the test section and supported the model. The experimental setup is depicted in figure 19 where the model and traverse-mounted wake rake are shown. The wake rake had 59 total pressure probes that were used to acquire the wake pressures. Both the wake and airfoil surface pressures were acquired with an electronically scanned pressure system. More information about the setup can be found in Lee [8].

Figure 19. Experimental Setup in Illinois 3- by 4-Foot Wind Tunnel

Although measured surface pressure distributions were available, the lift coefficient and quarter-chord, pitching-moment coefficient (C_m) reported here were derived from the force balance. The pressure and balance data agreed very well for the clean model configuration. However, larger differences were observed for the iced-model configurations because surface pressures could not be resolved accurately in the vicinity of simulated ice shapes. In addition, the runback ice shapes often covered a large chordwise area, eliminating multiple pressure taps and causing the integrated force and moment to be incorrect. Therefore, the data from the balance were more accurate. The drag coefficient was calculated from the wake pressures using standard momentum-deficit methods. All aerodynamic coefficients and the angle of attack were corrected for wall interference effects using the methods of Rae and Pope [16]. The experimental uncertainty in these coefficients was also estimated using the methods of Kline and McClintock [17] and Coleman and Steele [18] for 20:1 odds (table 11). The uncertainties in α, C_l and C_m were determined from the force-balance data and the remaining quantities pressure coefficient (C_p) and drag coefficient (C_d) were determined from the pressure-based data. The values were determined by Lee [8] and Lee and Bragg [19] for free-stream conditions of Re=1.8x10^6 and Mach number (M)=0.18. All data in this report correspond to this free-stream condition.

Table 11. Estimated Experimental Uncertainties

Aerodynamic Quantity	Reference Value	Absolute Uncertainty	Relative Uncertainty
α	5.00	±0.02	±0.40%
C_p	-0.712	±0.0037	±0.52%
C_l	0.295	±0.0016	±0.53%
C_m	-0.0791	±0.00039	±0.50%
C_d	0.0102	±0.00014	±1.40%

In addition to aerodynamic performance measurements, two other tools were used to evaluate the effect of the ice accretions on the airfoils. Boundary-layer profile measurements were taken using a boundary-layer rake (figure 20). The rake used the local static pressure obtained from the nearest airfoil pressure tap with total pressures measured using an array of pitot tubes to calculate the local airspeed. Fluorescent oil flow visualization was also used to identify specific flow features and aid in the interpretation of airfoil surface pressure data.

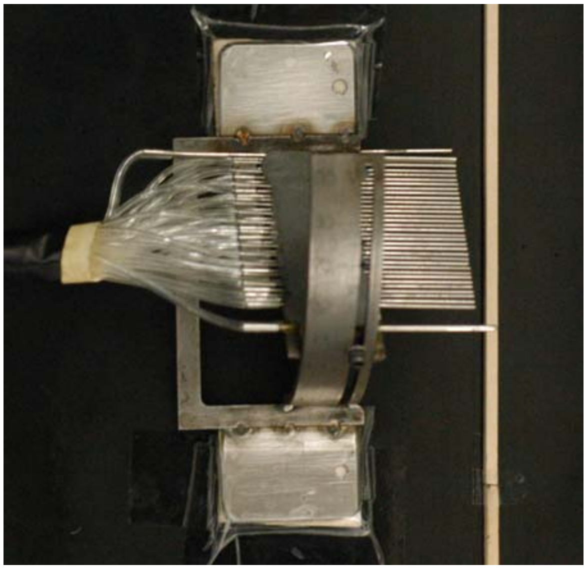

Figure 20. Boundary-Layer Rake (Viewed From Above) Attached to Model
(flow from right to left)

The models tested had a chord of 18 inches and spanned the entire height of the test section. Because a suitable model based on the business jet thermal model airfoil was not available for this investigation, two other models were chosen. The NACA 23012 and 3415 airfoils were selected to include a range of clean airfoil performance and geometric characteristics. The NACA 23012 model had 68 chordwise pressure taps and 19 spanwise pressure taps. The NACA 3415 model had a trailing-edge flap that was permanently set at zero degrees deflection for this test. The model had 78 chordwise pressure taps and 13 spanwise pressure taps.

Figure 21 compares the pressure distributions for these two airfoils. The pressure profile comparisons were done by matching the C_l of the business jet thermal model airfoil at 3 degrees XFOIL [20]. This corresponded to the angle of attack used for the hold condition during the IRT testing. Figure 21 shows that the NACA 23012 airfoil develops a higher suction surface pressure peak and steeper pressure recovery gradients than the NACA 3415 airfoil. Based on the lift and moment coefficient data for these airfoils (see section 3.2 for plots of these data), the NACA 23012 airfoil exhibits a leading-edge stall, and the NACA 3415 airfoil exhibits a combination of leading-edge and trailing-edge stall. In the latter case, such combinations of stalling characteristics are not uncommon, especially at low Reynolds number [21]. It is known that differences in clean airfoil characteristics can result in differences in iced airfoil performance penalties [8], especially with ridge-type shapes. Therefore, any differences in the performance of the airfoils with the runback simulations tested here present a range that may encompass the business jet model airfoil performance with the same runback simulations.

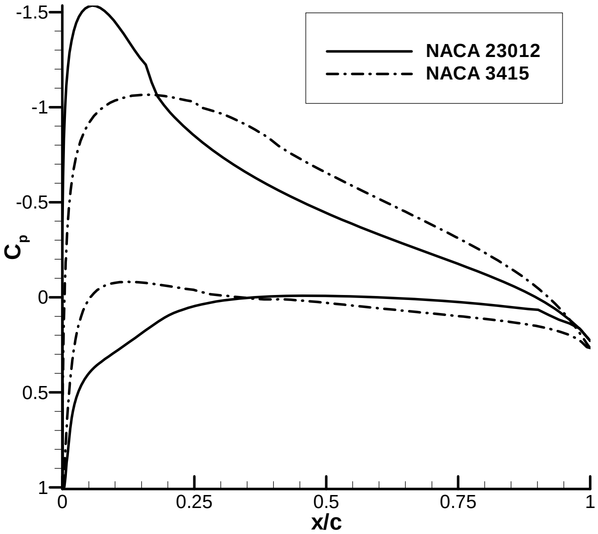

Figure 21. Comparison of Pressure Profiles at Matched C_l From XFOIL [20] (Re=7.65x10^6, M=0.33)

3.2 ICE SHAPE SIMULATION AND SCALING.

Since the aerodynamic investigations were limited to subscale, 2-D airfoil models, ice shape simulation and scaling were critical components of this work. While ice castings were produced from the icing tunnel tests, they could not be directly attached to the models used in the aerodynamic experiments. This was true for two reasons. First, the icing model had a mean chord length of 61 inches versus the aerodynamic model chord length of 18 inches. Second, the icing model was a 3-D wing section that had small, but not insignificant, amounts of sweep, taper, and twist. Both factors made it impractical, if not impossible, to apply any casting to the aerodynamic models used in this investigation. This meant that other methods of ice simulation had to be used.

The basic approach to this problem was to use simple materials, such as geometric shapes of balsa wood and roughness, to simulate the ice as documented in the icing tests. These are referred to as 3-D ice shape simulations. In this case, the castings did prove useful because they provided the best documentation of the accretions. As described in detail below, there is some precedent for the success of built-up simulations. Follow-up simulations that were much simpler in nature were also tested, such as a square or rectangular cross section that represented a ridge. These are referred to as 2-D ice shape simulations. These simpler simulations could then be easily varied parametrically in height and chordwise location. The combined aerodynamic results contributed to the understanding of the importance of simulation fidelity (i.e., how much of a difference does the extra geometry and roughness make?) as well as the sensitivity to height and chordwise location.

Another important factor in this investigation was ice shape scaling. Since the 2-D airfoil models used were much smaller in chord length than the icing model, the size of the ice accretions had to be reduced in the ice simulations. As described below, previous studies have shown that for many cases, geometric scaling based on the ratio of the model chord lengths produces excellent results over a large range of Reynolds number (1.0×10^6 to 10.0×10^6). In these studies, the simulated ice shapes were many times taller than the local boundary-layer thickness on the clean airfoil at the location of the ice. In the present study, it was found that for a subset of the runback ice accretions, this was not true. That is, the ridge heights were on the same order of magnitude as the local boundary-layer thickness on the clean airfoil. This meant that the geometric scaling method may not be appropriate for tests conducted at low Reynolds number (such as 1.8×10^6). Thus, the introduction of another scaling method, based on the ratio of the boundary-layer thickness between the icing and aerodynamic models, was required. Therefore, the Reynolds number and airfoil shape (pressure distribution) became important factors in the simulation in addition to the chord length. It is important to note that the geometric and boundary-layer scaling represent a reasonable range of simulated ice shape heights. The authors are unaware of any conclusive study governing the selection of appropriate scaling methods for runback-type ice ridges with heights that are on the order of the local boundary-layer thickness. Sections 3.2.1 and 3.2.2 describe the resulting simulation methodologies and both scaling methods.

3.2.1 Geometrically Scaled, 3-D Ice Shape Simulations.

All 3-D ice shape simulations tested on the NACA 23012 and 3415 airfoils were geometrically scaled based upon the ratio of the chord of the Illinois models to the midspan chord of the IRT model. The chord of the Illinois models was 18 inches and the midspan chord of the IRT model was 61 inches, which made the scaling factor 0.295.

Broeren and Bragg [22] showed that building up a 3-D ice shape simulation from roughness elements accurately reproduced the aerodynamic effects of cast shapes of leading-edge ice accretions. The geometric scaling factor in their study was 0.5. In addition, tests of a geometrically scaled ice shape simulation with a k/c=0.014 at x/c=0.20 on the suction surface were conducted on 36- and 18-inch chord models at Reynolds numbers between 1.8×10^6 and 7.5×10^6 [23]. Negligible changes in the aerodynamic penalties due to Reynolds number were observed. In both studies, the height of the ice shape simulations was at least an order of magnitude taller than the local boundary-layer thickness on the clean airfoil. Given the success of these previous geometric scaling experiments, this method was applied to the runback ice accretions obtained in this work.

A method similar to that of Broeren and Bragg [22], including the use of wood substrates, was used to create the runback 3-D ice shape simulations. Figure 22 is a photograph of the 3-D ice shape simulation or the suction surface. The construction of the ice shape simulations was conducted in the following manner. First, a substrate was chosen to simulate the base of the ice accretion, typically a section of balsa wood. Here, the base refers to the portion of the accretion that did not include roughness and other protuberances. The size of roughness elements used was determined by direct measurement of the features of the ice castings taken from the corresponding IRT accretion. In some cases, multiple roughness sizes were used. These elements were attached to the substrate by depositing them onto a layer of adhesive with chordwise extent corresponding to the average chordwise extent of the ice accretion being simulated. The roughness elements were deposited either by spraying or sprinkling, depending on the desired distribution and density. The density of the roughness was simulated in a qualitative manner from observation of the corresponding IRT accretion.

Figure 22. Photograph of Suction Surface 3-D Ice Shape Simulation for Warm-Hold Case

As seen in table 3, the height of the ice shapes was not easy to characterize. For the ice shape simulations tested, the average of the ice shape heights was taken and the height variation was simulated by the use of roughness elements. The 3-D ice shape simulations for the warm-hold case was constructed from a 0.063-inch-thick by 1.5-inches-wide wood substrate with roughness in the area of the ridge, approximately the first 0.25, and simulated rivulets aft. The shape was contoured to smoothly join with the airfoil at the end of the ice shape simulation, as was observed on the casting. The overall height of the shape was between 0.063 and 0.09 inch, corresponding to a k/c between 0.0035 and 0.005. The pressure surface ice shape simulation was a simple ridge, 0.3 inch in chordwise dimension, with roughness to simulate the features observed on the casting. The total height of the pressure surface ice shape simulations varied between 0.15 and 0.25 inch, equivalent to a k/c between 0.008 and 0.014, across the span. In the warm-hold case, the ice accretions began to form at approximately x/c=0.16 on the suction surface and x/c=0.20 on the pressure surface.

Figure 23 shows the leading edge of the NACA 23012 with the runback 3-D ice shape simulation for the cold-hold case. The suction surface ice shape simulation was constructed of two layers of balsa wood. The base was 0.063 inch thick. An overhang was created by securing a 0.03-inch-thick piece on top with 0.1 inch protruding forward of the base. This feature was observed on the castings of the cold-hold ice accretions. In addition, an effort was made to create periodic accumulations, one of which is visible in figure 11 near the bottom of the photograph. The overall height of the ice shape simulation with roughness was between 0.094 and 0.125 inch, corresponding to a k/c between 0.005 and 0.007. The chordwise extent of the ice shape simulation was approximately 0.6 inch and spanned the entire model. A similar ice shape simulation was constructed for the pressure surface. A 0.03-inch-thick base was used with a second 0.03-inch-thick layer overhanging the base by 0.05 inch. The thickness with roughness was approximately 0.1 inch, equivalent to a k/c of 0.006, and the chordwise extent was 0.625 inch. The cold-hold ice accretion was observed to begin at approximately x/c=0.015 on the suction surface and x/c=0.035 on the pressure surface.

Figure 23. Photograph of 3-D Ice Shape Simulation for Cold-Hold Case

The descent ice accretion was simulated with a simple ridge on the suction surface and roughness on the pressure surface positioned at x/c=0.01 and x/c=0.015, respectively. The suction surface ridge was a 0.063-inch (k/c=0.0035)-square piece and the pressure surface simulation consisted of 0.25 inch, in the chordwise direction, of 36 grit roughness that is nominally 0.0232 inch (k/c=0.0013) in diameter.

3.2.2 Geometrically and Boundary-Layer-Scaled 2-D Ice Shape Simulations.

In addition to the 3-D ice shape simulations, more simplified 2-D ice shape simulations were also tested on the NACA 23012 and 3415 airfoils. The goal of the 2-D ice shape simulations was to represent the height of the runback ice ridges. They consisted of balsa ridges with no roughness applied, no spanwise variation and, unless otherwise indicated in the discussion of the results, a square cross section. When the purpose of the 2-D ice shape simulation was to compare directly with the 3-D ice shape simulation, ridges were placed on both the suction and pressure surfaces. Otherwise, ridges were placed only on the suction surface, where they have the greatest aerodynamic effect. Since these 2-D ice shape simulations were simply balsa ridges with square (or, where noted, rectangular) cross sections placed at a given chordwise location along the span on the suction surface, they will usually be referred to simply as ridges in the rest of this report.

The location of the ridges corresponded to the forward face of the runback ice ridges observed in the icing tunnel testing. The advantage of using ridges for the aerodynamic testing was that they allowed for easy parametric variation in height and chordwise location. The ability to easily vary the height was important. In the development of the test matrix, it was noted that the heights of ridges were approaching the thickness of the local boundary layer. This led to the boundary-layer scaling method.

The ridges were scaled based upon the tunnel conditions at which the corresponding ice shapes were accreted in the IRT. Namely, the Reynolds number, Mach number, and angle of attack were used as inputs to the boundary-layer code that calculated the boundary-layer thickness at the ridge locations. The code used integral boundary-layer parameters obtained from XFOIL [20] with the Falkner-Skan [24] solution for a laminar boundary layer and the Coles wake [25] solution for a turbulent boundary layer to calculate the local boundary-layer thickness. Tables 12 and 13 compare the heights of the ridges scaled geometrically and using the boundary-layer height. Scaling was carried out at $\alpha=3^{o}$, the angle of attack at which the ice was accreted. The boundary-layer thickness δ is a function of angle of attack, causing k/δ to decrease as angle of attack is increased. The boundary-layer-scaled ridges were over twice as tall as the geometrically scaled ridges for the same case. Differences in boundary-layer growth on the two airfoils are more apparent in the warm-hold case because the ice shapes accrete farther aft on the airfoil.

Table 12. Ridge Scaling for Warm-Hold Case

	Geometric Scaling			Boundary-Layer Scaling		
Airfoil	*k* (in.)	k/c	*k*/δ	*k* (in.)	k/c	*k*/δ
Full Scale	0.232	0.0038	5.35	0.232	0.0038	5.35
NACA 23012	0.068	0.0038	2.44	0.149	0.0083	5.35
NACA 3415	0.068	0.0038	3.11	0.117	0.0065	5.35

x/c=0.16, suction surface, δ calculated at $\alpha=3^{\circ}$

Table 13. Ridge Scaling for Cold-Hold Case

	Geometric Scaling			Boundary-Layer Scaling		
Airfoil	*k* (in.)	k/c	*k*/δ	*k* (in.)	k/c	*k*/δ
Full Scale	0.412	0.0068	28.4	0.412	0.0068	28.4
NACA 23012	0.122	0.0068	12.5	0.278	0.0154	28.4
NACA 3415	0.122	0.0068	12.6	0.276	0.0153	28.4

x/c=0.028, suction surface, δ calculated at $\alpha=3^{\circ}$

3.3 RESULTS.

The results presented here are for 2-D airfoils (NACA 23012 and 3415). The effects of ice accretions on a 3-D wing would be dependent on the specific wing geometry. Furthermore, the simulated shapes tested were representative of the specific conditions tested in the IRT as described in section 2. The simulations were made using measurements taken from that test and by reproducing the features observed on the castings of the full scale accretions. As discussed in section 2, there are many factors that affect the accumulation of runback ice, including thermal system performance. The effect of runback ice on aerodynamic performance is a function of those factors as well as the geometry of the airfoil or wing. All scaling of the ridges for testing was done with respect to the midspan chord of the thermal model.

3.3.1 Warm Hold.

The effect of a geometrically scaled, 3-D ice shape simulation (from an h, k_0, RHF warm-hold IRT run) is presented in figure 24. Both the NACA 23012 and 3415 data are shown. Maximum lift coefficient was reduced to 1.16 for both airfoils. The clean C_{lmax} was 1.46 and 1.35 for the NACA 23012 and 3415, respectively. A 1-degree reduction in α_{stall} was seen for the NACA 3415, and a reduction of 2 degrees was seen for the NACA 23012. The minimum drag coefficient increased to approximately 0.035 in both cases from the clean value of 0.0073 for the NACA 23012 and 0.0080 for the NACA 3415.

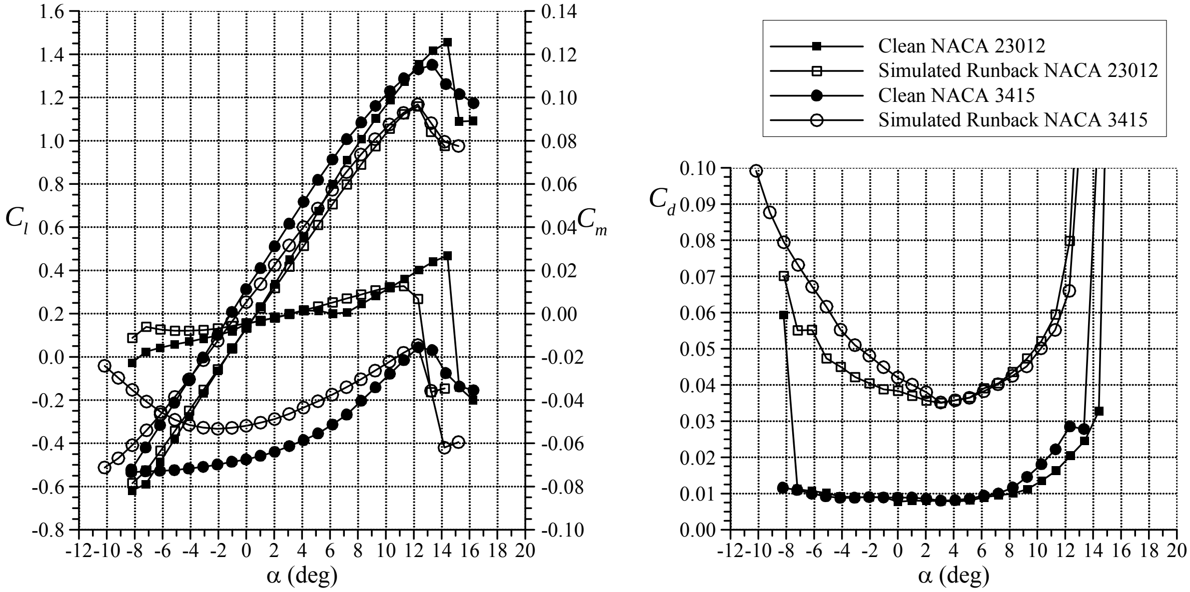

Figure 24. Effect of 3-D Ice Shape Simulation for the Warm-Hold Case on the Lift, Drag, and Pitching Moment of the NACA 23012 and 3415 (*Re*=1.8x10^6, M=0.18)

Figure 25 compares the effects on the performance of the NACA 3415 of a geometrically scaled, 3-D ice shape simulation for the warm-hold case to that of the 2-D ice shape simulation. For this study, both the suction and pressure surface accretions were simulated. The 2-D simulation increased C_{lmax} by 0.17 and increased C_{dmin} to 0.026. It also increased α_{stall} by 4 degrees. A 2-D simulation based on the maximum height measured from the full-scale accretion is also included. The ice shape had a height of 0.094 inch (k/c=0.0052). However, it was not representative of the overall ice shape because it was based on an isolated feature of the accretion. It does demonstrate that there was a significant change in the effect of the ridge at this x/c location at heights between 0.063 inch, where there was a lift performance increase, and 0.094 inch, where there was a lift performance penalty. The 2-D Max simulation decreased C_{lmax} by 0.14 and increased C_{dmin} to 0.028. The stalling angle of attack was unchanged by the simulation.

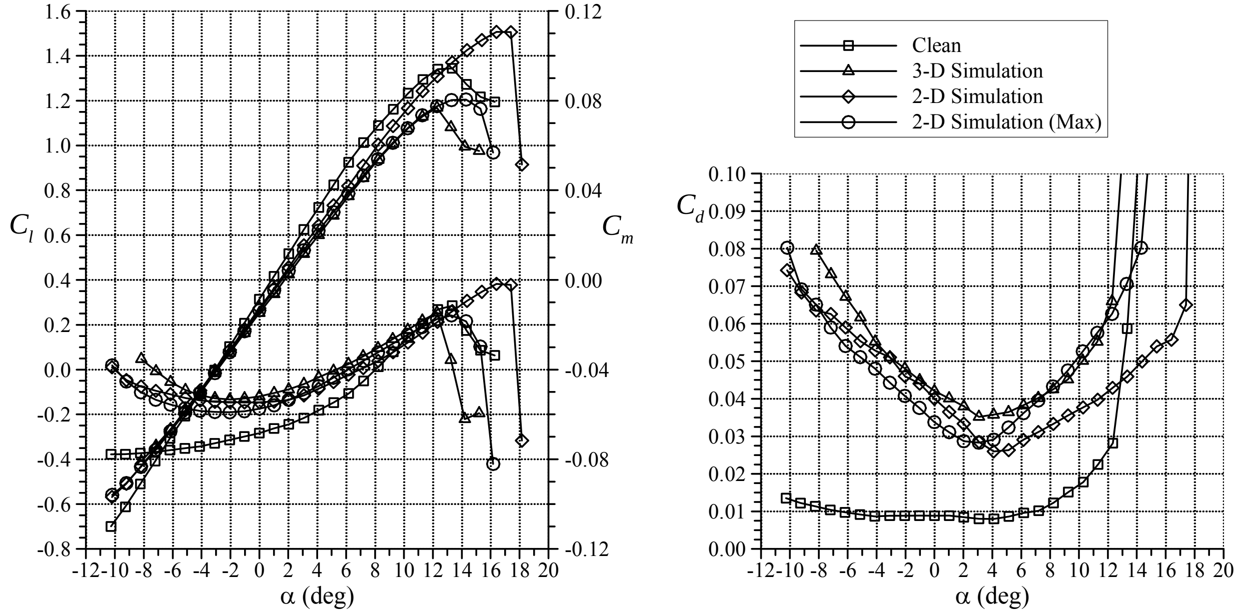

Figure 25. Comparison of the Effect of Geometrically Scaled, 3-D and 2-D Ice Shape Simulations for the Warm-Hold Case on the Lift, Drag, and Pitching Moment of the NACA 3415 (*Re*=1.8x10^6, M=0.18)

Figure 26 presents the performance effects of the same ice shape simulations on the NACA 23012. In contrast to the NACA 3415, the NACA 23012 exhibits an abrupt stall, indicating that it naturally stalls from the leading edge. McCullough and Gault [21] conducted extensive investigations into airfoil stall and found that leading-edge stall is typical of airfoils of moderate thickness like the NACA 23012, while trailing-edge stall is typical for thicker airfoils like the NACA 3415. The geometrically scaled, 2-D ice shape simulation had little effect on the maximum-lift performance of the NACA 23012, reducing C_{lmax} by 0.04. However, the minimum drag increase to 0.030 was similar to that experienced by NACA 3415. The 2-D simulation based on the maximum measured height again had a substantial effect on the performance, similar to that of the 3-D ice shape simulation, and appeared to alter the stalling character of the airfoil. The pressure surface ridge for that case was not based on the maximum height of the pressure surface ice accretion, and was actually slightly shorter, with a height of 0.17 inch, than the primary 2-D ice shape simulation. This caused the drag at low and negative C_l to be lower. This was also observed on the NACA 3415, but to a lesser degree. The 2-D Max simulation reduced the C_{lmax} to 1.04 and increased C_{dmin} to 0.032. It is important to note that in all these cases (i.e., figures 25 and 26), the presence of the ice shape reduced the lift curve slope. It was only at high angle of attack that the geometrically scaled, 2-D ice shape simulation was able to achieve any improvement in performance (for the NACA 3415 airfoil only).

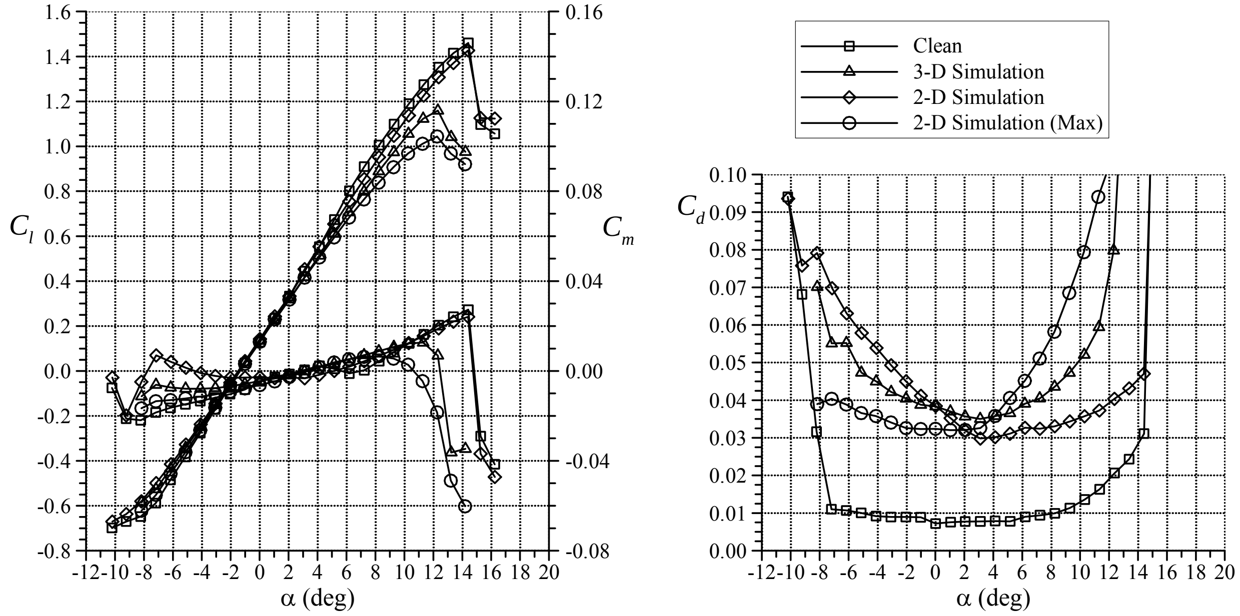

Figure 26. Comparison of the Effect of Geometrically Scaled, 3-D and 2-D Ice Shape Simulations for the Warm-Hold Case on the Lift, Drag, and Pitching Moment of the NACA 23012 ($Re=1.8\text{x}10^6$, M=0.18)

Figure 27 presents the effect of ridges for the warm-hold case on the performance of the NACA 3415. The suction surface ice shapes alone are presented to demonstrate the difference between the boundary-layer and geometrically scaled ice shape simulations. The simulated geometrically scaled ice shape refers to an ice shape created by taking an average height and chordwise location, taken from ice measurements as well as castings, and scaling that height based upon the ratio of the chord of the subscale model to that of the full-scale model (i.e., matched k/c). The boundary layer-scaled ice shape refers to the same ice shape scaled by the ratio of the local boundary-layer thickness of the subscale model to the full-scale model (i.e., matched k/δ). The goal of the 2-D ice shapes was to simulate the ice ridge rather than the entire extent of the ice shape. In the geometrically scaled case, a 0.063-inch (k/c=0.0035)-high square section of balsa was positioned at x/c=0.16 to simulate the warm-hold ice shape. Interestingly, α_{stall} increased by 4 degrees and the C_{lmax} increased to 1.51. This is the effect that motivated the investigation of Reynolds number effects on the small-scale model boundary-layer behavior as a factor in the performance effects of these ice shapes. Note that the character of the stall changed for the geometrically scaled ice shape simulation. It became much more abrupt, indicating that it was a leading-edge stall, in both the loss of lift and the change in the pitching moment. The boundary-layer-scaled ice shape was a 0.125-inch-square section of balsa also positioned at x/c=0.16 and reduced C_{lmax} to 0.95 and caused a 2 degree reduction in stalling angle of attack. For the boundary-layer-scaled ice shape simulation, the stall character appeared to be more like that of the clean airfoil.

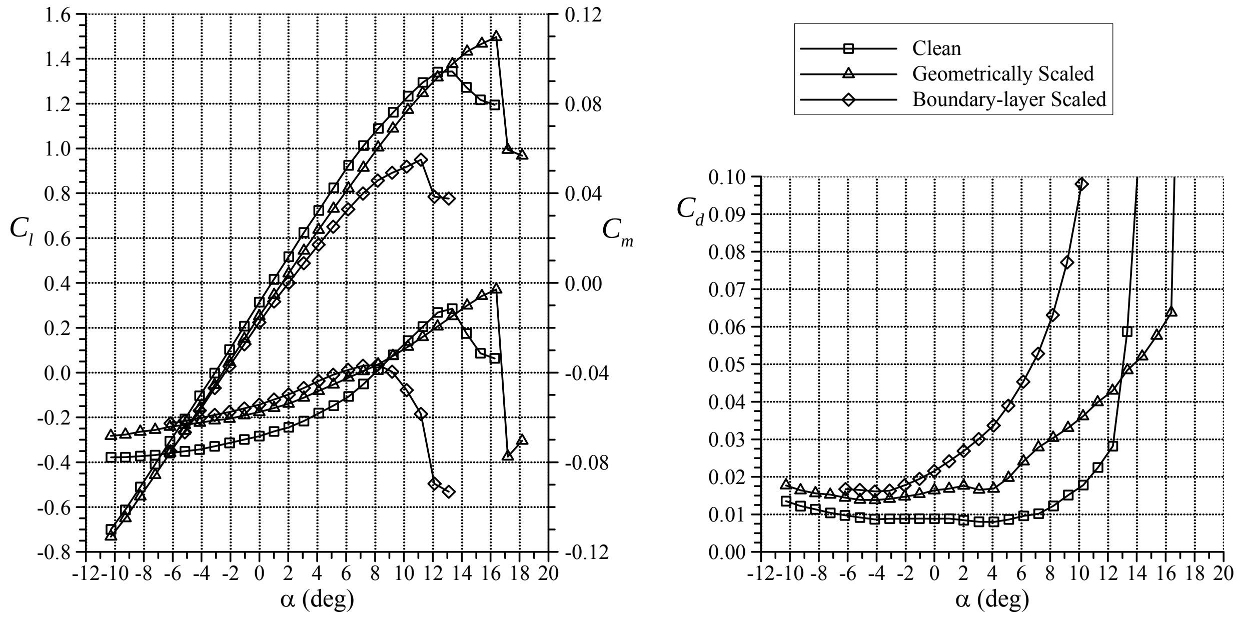

Figure 27. Effect of a 2-D Ice Shape Simulation for the Warm-Hold Case (Suction Surface Only) on the Lift, Drag, and Pitching Moment of the NACA 3415 (Re=1.8x10^6, M=0.18)

3.3.2 Effect of Chordwise Extent of Ridges.

An investigation into the effect of the chordwise extent of the ridges was conducted. Figure 28 presents the effect of chordwise extent for 0.063- and 0.125-inch-high rectangular ridges at x/c=0.05 and 0.10 on the maximum lift and stalling angle of attack of the NACA 23012. Stalling angle of attack and maximum lift coefficient did not vary significantly with the chordwise extent of the ridge, except in the case of the 0.063-inch ridge. In the case of the 0.063-inch ridge at x/c=0.10, the stalling angle of attack (figure 28(a)) was reduced to approximately 11 degrees at the shortest chordwise extent (0.35%c or 0.063 inch), then increased to nearly the clean value and was again reduced to approximately 12 degrees by the ridge with the greatest chordwise extent (2.77%c or 0.5 inch). The maximum lift coefficient followed a similar trend (figure 28(b)). The ridge with shortest chordwise extent reduced C_{lmax} to 1.15 and that with greatest chordwise extent reduced it to 1.17, but the intermediate chordwise extents reduced C_{lmax} to only 1.30. At x/c=0.05, there appeared to be some dependence of maximum lift coefficient on chordwise extent, but it was not as dramatic as at x/c=0.10. The stalling angle of attack was not affected by chordwise extent for the 0.063-inch shape at x/c=0.05.

Figure 29 presents the effect of chordwise extent of ridges at x/c=0.05 and x/c=0.10 for both a 0.063- and 0.125-inch-high ridge on the zero-lift angle of attack ($\alpha_{l,0}$) and zero-lift drag of the NACA 23012. The clean value of both parameters is included in the plots as a bold line. It can be seen that the 0.063-inch-high ridge causes $\alpha_{l,0}$ to become less negative as the chordwise extent is increased (figure 29(a)), in effect decambering the airfoil. The 0.125-inch ridge appears to have a similar effect, but it is less significant than for the 0.063-inch ridge. Chordwise extent acted to reduce the zero-lift drag increase caused by the both the 0.063- and 0.125-inch ridges (figure 29(b)).

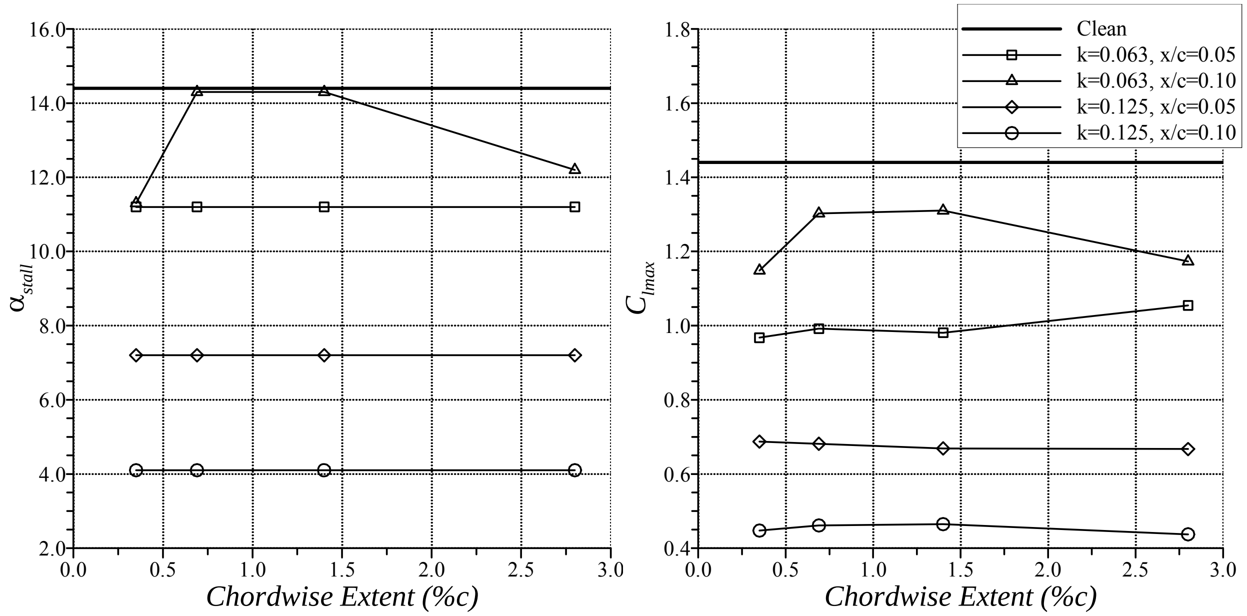

(a) (b)

Figure 28. Effect of Chordwise Extent of *k*=0.063-Inch and *k*=0.125-Inch Ridges at x/c=0.05 and 0.10 on the (a) α_{stall} and (b) C_{lmax} of the NACA 23012 (*Re*=1.8x10^6, M=0.18)

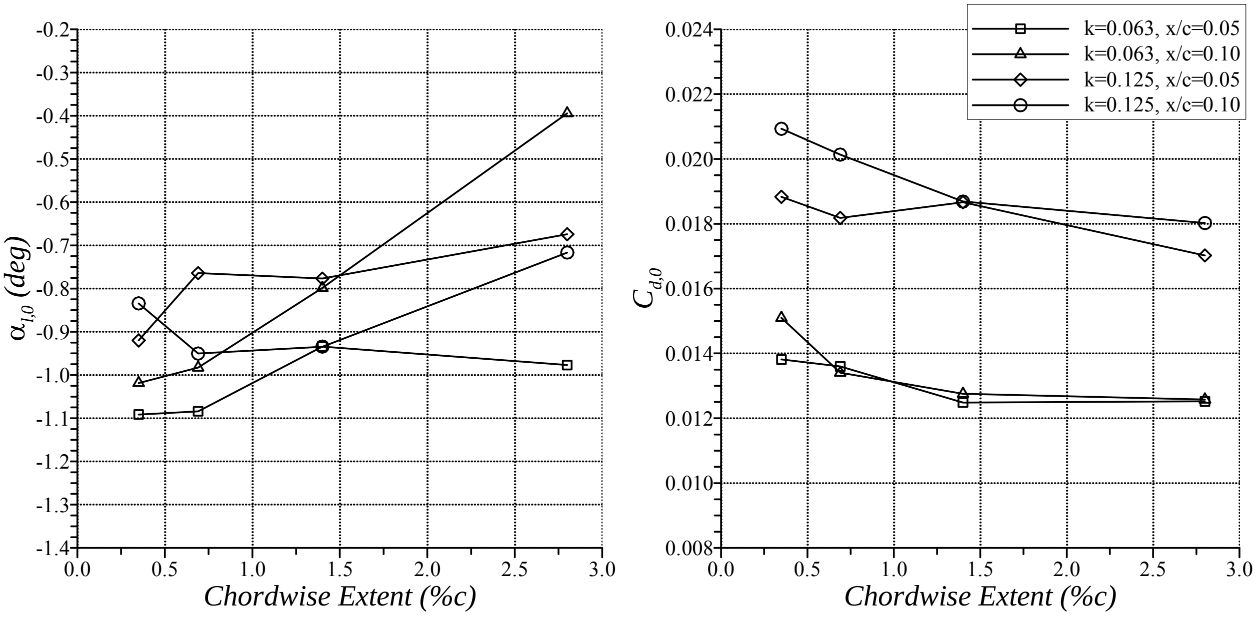

(a) (b)

Figure 29. Effect of Chordwise Extent of *k*=0.063-Inch and *k*=0.125-Inch Ridges at x/c=0.05 and 0.10 on the (a) $\alpha_{l,0}$ and (b) $C_{d,0}$ of the NACA 23012 (*Re*=1.8x10^6, M=0.18)

3.3.3 Lift Enhancement of Ridges.

Another motivation for exploring the boundary-layer scaling of the ridges was to investigate the phenomenon by which α_{stall} and C_{lmax} are increased by the presence of the geometrically scaled ridges for the warm-hold case. Results from fluorescent oil flow visualization for the NACA 3415 at $\alpha=16^o$ with the 0.063-inch-high ridge located at x/c=0.16 are presented in figure 30. Sixteen degrees angle of attack corresponded to C_{lmax} for this case (figure 27). Transition was apparent near the leading edge, followed by a faint zone at approximately x/c=0.22 where the flow reattached after separating from the ridge. Trailing-edge separation then occurred between x/c=0.60 and x/c=0.65. Stall, in this case, resulted from the collapse of the leading-edge pressure peak that was developed because of the separation bubble just aft of the ice shape.

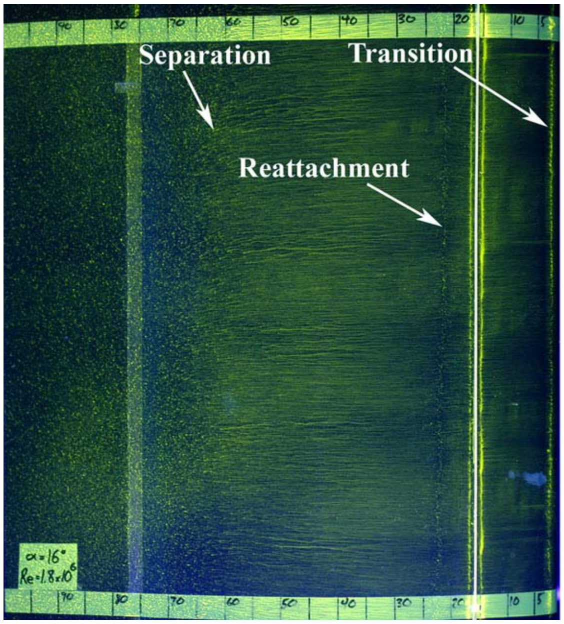

Figure 30. Fluorescent Oil Flow Visualization at $\alpha=16°$ for the NACA 3415 With the Geometrically Scaled Ridge for the Warm-Hold Case ($Re=1.8x10^6$, M=0.18)

In the case of the boundary-layer-scaled ice shape, which had a height of 0.125 inch, the reattachment zone moved aft rapidly with angle of attack. Figure 31 shows the fluorescent oil flow visualization results for the NACA 3415 with the boundary-layer-scaled ridge for the warm-hold case. The corresponding performance data were presented in figure 27. In figure 31(a), corresponding to $\alpha=6°$, the reattachment zone following separation from the ridge was clearly visible near $x/c=0.35$. At $\alpha=8°$ (figure 31(b)), trailing-edge separation moved forward slightly and reattachment moved aft by approximately 0.05. At $\alpha=9^o$, there appeared to be some reverse flow in the region between the ridge and approximately $x/c=0.40$; however, there was no evidence of attached flow following the line that divided the reverse flow from the flow aft of it. This indicated that the bubble was no longer closed, and the flow was separating from the ridge and not reattaching to the airfoil. In the case of the 0.125-inch-high ridge, separation progressed forward rapidly from the trailing edge to meet the separation bubble growing rearward to cause stall.

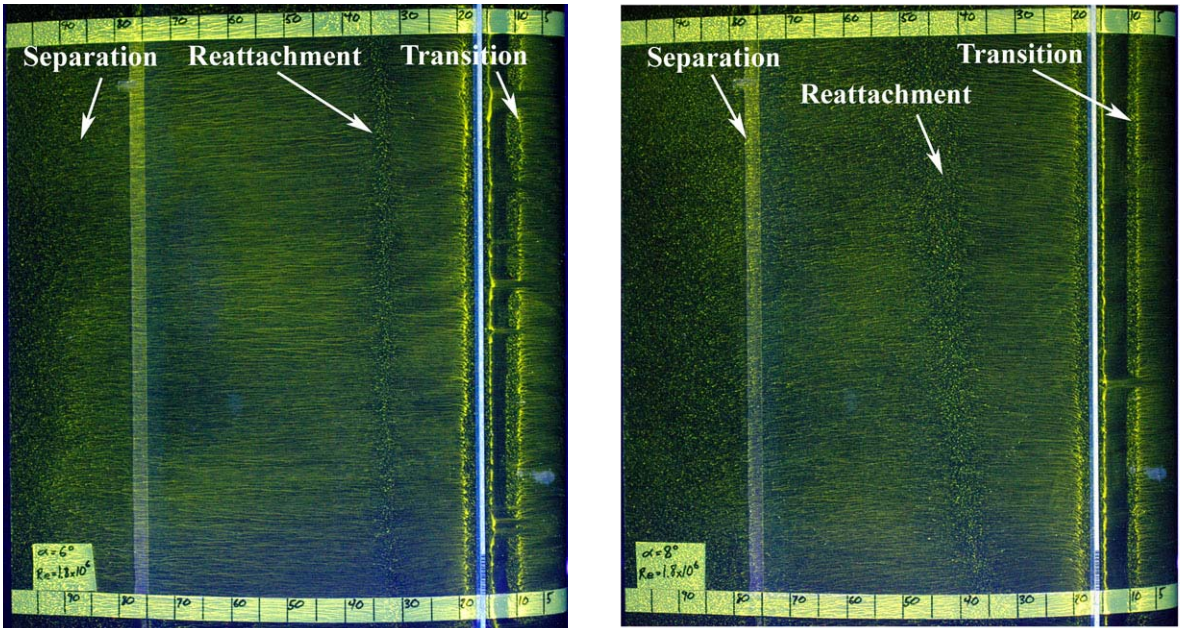

(a) α=6° (b) α=8°

Figure 31. Fluorescent Oil Flow Visualization at (a) α=6° and (b) α=8° for the NACA 3415 With the Boundary-Layer-Scaled Ridge for theWarm-Hold Case. (*Re*=1.8x10^6, M=0.18)

The results of the flow visualization are summarized in figure 32. For the boundary-layer-scaled ridge, flow visualization showed that trailing-edge separation progressed rapidly forward as angle of attack increased, and that the separation bubble was much larger than for the geometrically scaled ridge. The separation bubble for the geometrically scaled ridge remained approximately 5% to 7% of the chord up to stall (figure 32(a)) and trailing-edge separation progressed only to approximately x/c=0.65 at stall. For the boundary-layer-scaled ridge, the separation bubble was 30% to 40% of the chord prior to stall (figure 32(b)). In addition, the flow appeared to be separated directly from the ridge at angles of attack greater than 8 degrees.

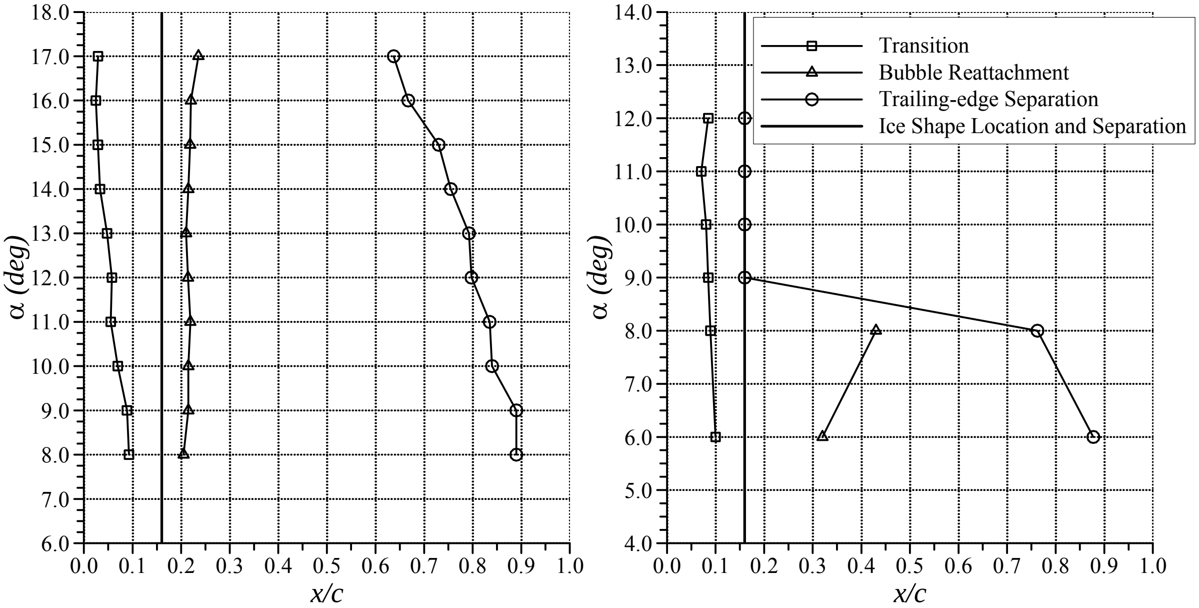

(A) GEOMETRICALLY SCALED (B) BOUNDARY-LAYER SCALED

Figure 32. Fluorescent Oil Flow Visualization Analysis With (a) the Geometrically Scaled and (b) the Boundary-Layer-Scaled Ridge for the Warm-Hold Case at x/c=0.16 (NACA 3415, *Re*=$1.8\text{x}10^6$, M=0.18)

Figure 33 illustrates the effect of ice shape height at x/c=0.16 on the performance of the NACA 3415. Ridges of two other heights, in addition to the geometrically scaled, 2-D warm-hold ice shape, were also tested. Stall was delayed by the previously discussed 0.063-inch-high (k/c=0.0035) and the 0.08-inch-high (k/c=0.0044) ridges. However, the 0.094-inch-high (k/c=0.005) ridge reduced the C_{lmax} of the airfoil and maintained the same α_{stall} as the clean airfoil. Recall that the geometrically scaled ridge had k/c=0.0035 and the boundary-layer-scaled ridge had k/c=0.007.

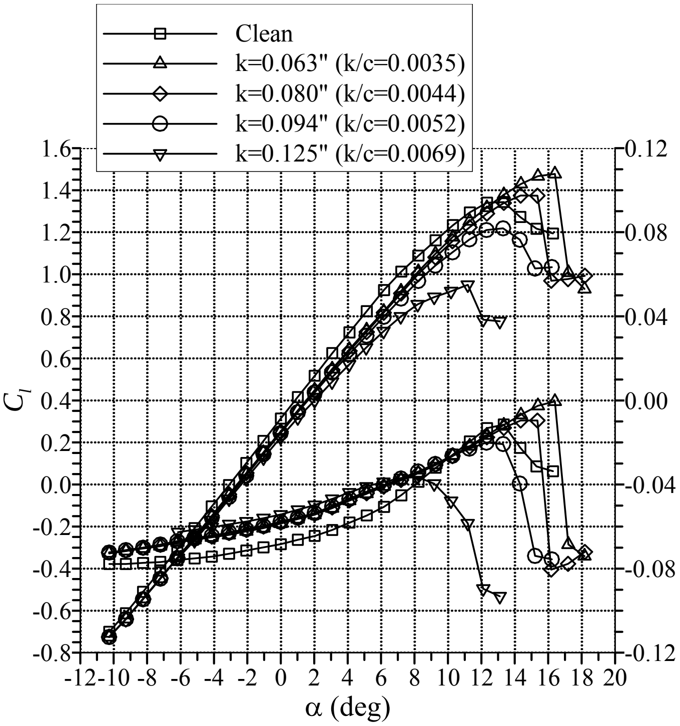

Figure 33. Effect of Ridge Height at x/c=0.16 on the NACA 3415 (Re=1.8x10^6, M=0.18)

Figure 34 compares k/δ as a function of C_l/C_{lmax} for the ridge tested in the present study to 2-D ice shape simulations tested by Calay [9] and Papadakis [10]. In each case, the boundary-layer height was calculated for the clean airfoil. The Reynolds number for these cases ranged from 1.25x10^6 to 2.0x10^6. The Calay and Papadakis simulations were located at x/c=0.15 versus x/c=0.16 for the present study. 2-D ice shape simulations that were observed to cause a performance increase had a k/δ near 1 as the airfoil approached C_{lmax}. In contrast, the boundary-layer-scaled ridge with a height of 0.125 inch had a k/δ greater than 2 up to stall. This demonstrated that the relative height of the ridge to the boundary layer plays a significant role in the phenomenon. It also showed that simple geometric scaling of runback ice accretions may not be sufficient to accurately describe their aerodynamic effects.

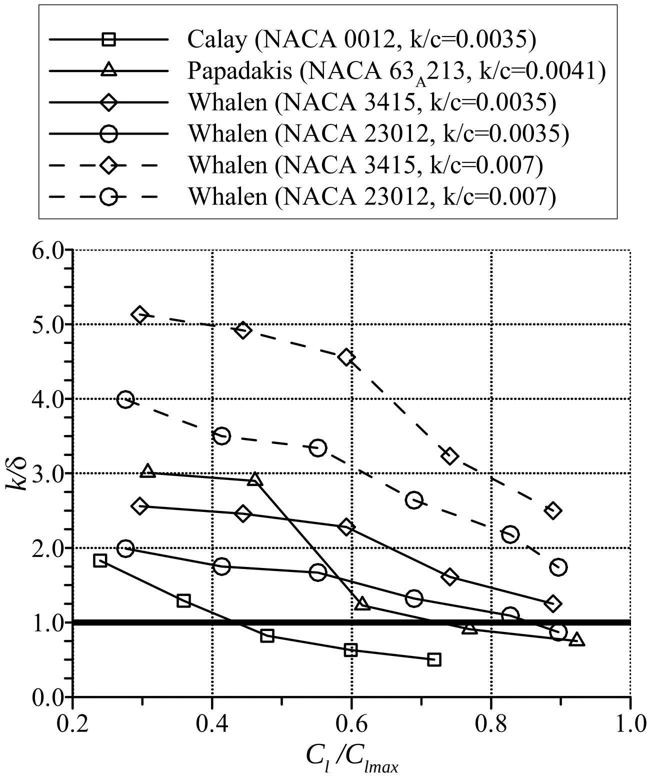

Figure 34. Comparison of *k*/δ for Various Ice Shapes at x/c=0.15 [9, 10, and 11]

Figure 35 shows boundary-layer profile measurements for the geometrically scaled ridges at $\alpha=8^o$. Figure 36 shows boundary-layer profile measurements for the boundary-layer-scaled ridge at $\alpha=8^o$. The boundary-layer flow is quite different between the two ice shapes. Pitot tubes were used to collect the pressure data from which local flow velocity was calculated. Because pitot tubes do not read correctly in areas of reverse flow, these areas are indicated as zero velocity in the figures. In the case of the geometrically scaled ice shape, the only zero velocity reported was at the lowest pitot tube positioned at approximately 0.01 inch from the model surface. At heights of 0.03 and 0.06 inch, there were sharp increases in the local velocity. Subsequent measurements at x/c=0.20, 0.24, and 0.30 showed that these sharp changes in the velocity in the boundary layer were not present by x/c=0.20. However, the phenomenon persisted in milder form and manifested as a slope change in the part of the profile that remains within the boundary layer to x/c=0.30, the farthest aft station where measurements were taken. At x/c=0.20, the slope change extends from approximately 0.04 to 0.08 inch and at x/c=0.30, the slope change extends from approximately 0.06 to 0.12 inch. The increased boundary-layer edge velocity was also echoed in the pressure profiles at this angle of attack (figure 37). In the pressure profiles, the local edge velocity, derived from surface pressure measurements, was greater than that on the clean model up to approximately x/c=0.25. The boundary-layer profiles for the boundary-layer-scaled ridge showed a large region of reverse flow that reached a maximum height of 0.2 inch near x/c=0.24 and decreased in height by *x*/c=0.30. Flow visualization showed that the separation bubble reattached near x/c=0.42. Clearly, the geometrically scaled ridge was able to modify the boundary-layer flow while only creating a small, stable separation bubble, while the boundary-layer-scaled ice shape generated a large separation bubble. This modification apparently allowed the boundary layer to remain attached at angles of attack greater than the clean stalling angle of attack by energizing it and delaying the advancement of the trailing-edge separation. The large separation bubble generated by the boundary-layer-scaled ridge removes momentum from the boundary layer and hastens the advancement of the trailing-edge separation, causing the airfoil to stall earlier.

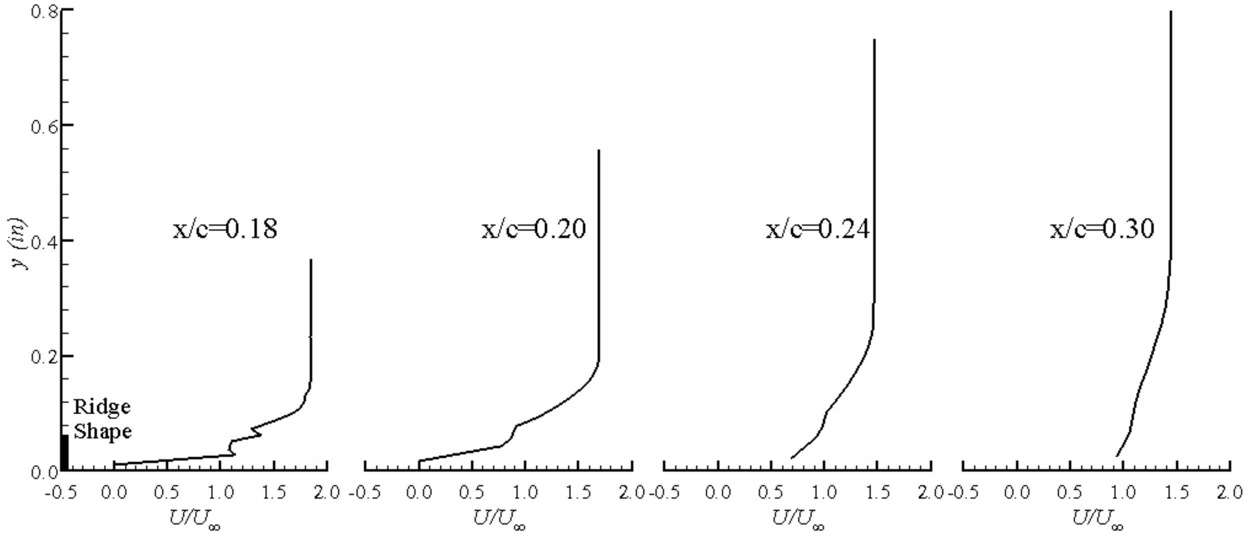

Figure 35. Boundary-Layer Profile Measurements at α=8° for the Geometrically Scaled Ridge for the Warm-Hold Case at x/c=0.18, 0.20, 0.24, and 0.30 (NACA 3415, *Re*=1.8x106, M=0.18)

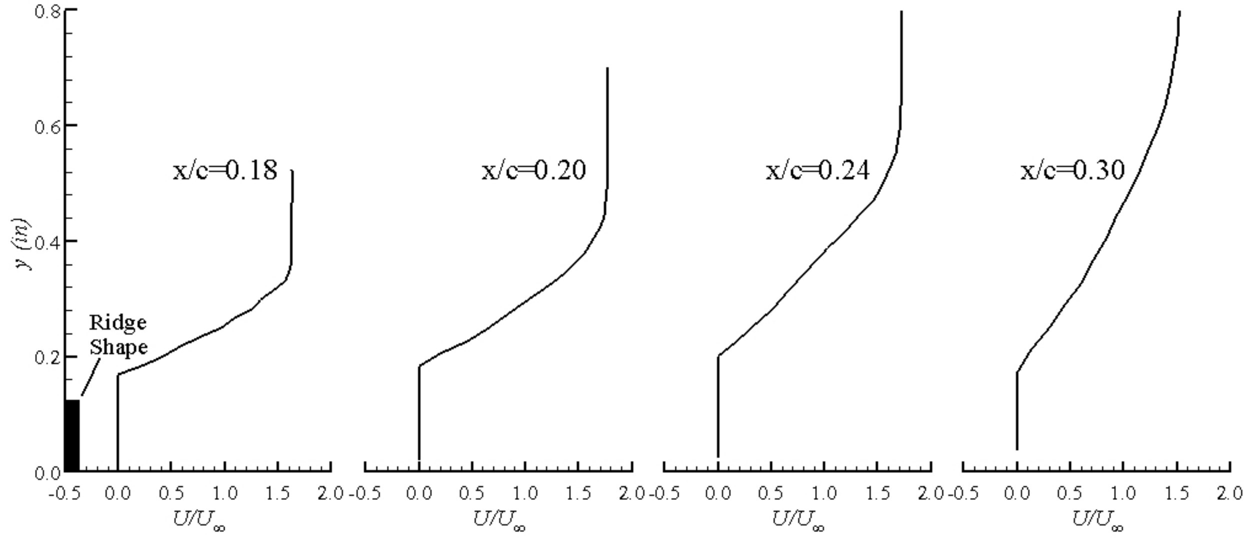

Figure 36. Boundary-Layer Profiles Measurements at α=8° for the Boundary-Layer-Scaled Ridge for the Warm-Hold Case at x/c=0.18, 0.20, 0.24, and 0.30 (NACA 3415, *Re*=1.8x10^6, M=0.18)

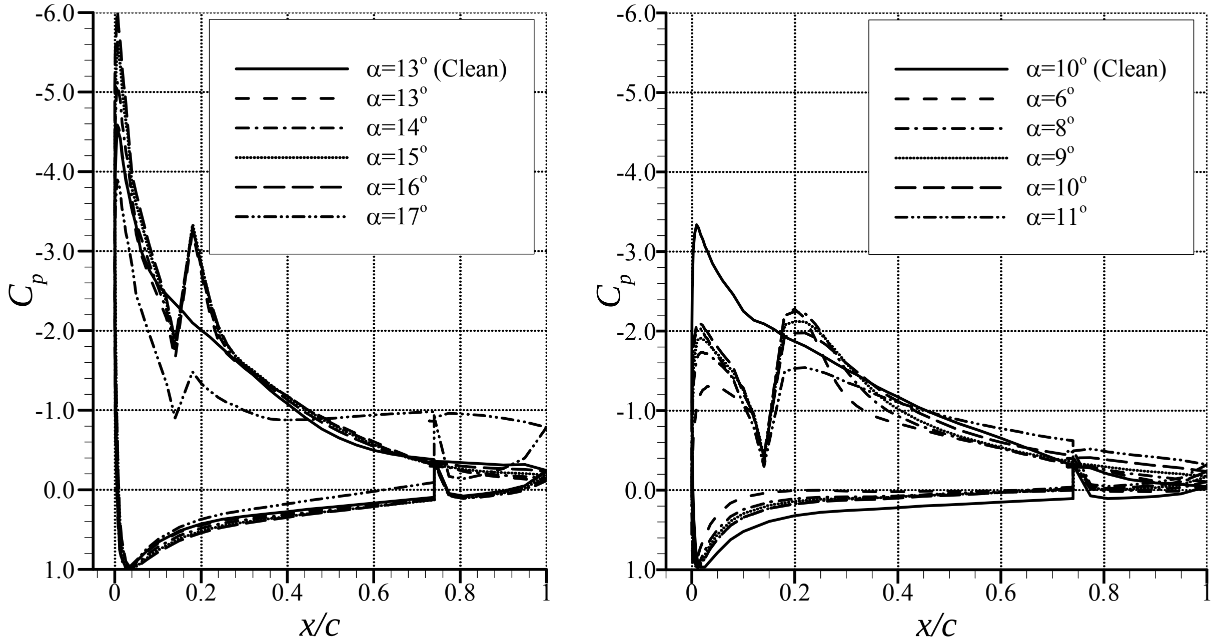

(a) **(b)**

Figure 37. NACA 3415 Pressure Profiles Near Maximum Lift With the (a) Geometrically Scaled and (b) Boundary-Layer-Scaled (b) Ice Shape Installed at x/c=0.16 (*Re*=1.8x10^6, M=0.18)

Analysis of the pressure distributions on the model as a result of these ridges indicated another effect besides energizing the boundary layer, which both Calay [9] and Papadakis [10] point to as the cause of the lift benefit. Figure 37(a) shows the pressure profiles for the NACA 3415 with the geometrically scaled ridge for the warm-hold case (0.063 inch high) installed at x/c=0.16. The first thing to note is the sharp increase in the magnitude of C_p following the ridge. In addition, the suction peak at the leading edge was allowed to grow to over 30% greater than the clean suction peak. The ability of the airfoil to sustain the higher suction peak and the added low pressure in the vicinity of the ridge generated lift coefficients that were larger than in the clean case. It is important to note that up to α=13°, the pressure peak was lower in magnitude, for the same angle of attack, with the ridge installed than it was in the clean case. The less negative C_p preceding the ice shape, as compared to the clean C_p in the same location, was caused by stagnation of the flow in front of the ridge. In addition, the flow accelerated over the ridge, generating an abrupt increase in the magnitude C_p. The subsequent rapid decrease in the magnitude of C_p and return to the clean C_p indicated the presence of a short separation bubble following the ice shape. A reduction in the lift curve slope at low angle of attack was observed for this ridge, which was consistent with the observed pressure distributions. At angles of attack greater than the clean stalling angle of attack, the delay in trailing-edge separation caused by the ridge allowed the circulation of the airfoil to continue to increase, driving the stagnation point farther aft on the pressure surface and resulting in greater flow acceleration near the leading edge. The recovery that followed the second pressure peak was gentle compared to that of the leading-edge peak and, in fact, was comparable to the recovery at 13 degrees, and decreased in slope with angle of attack. Ultimately, the gradients developed by the leading-edge peak were too great and the suction peak collapsed as the boundary layer separated from the ridge and failed to reattach. Oil flow visualization showed that after stall, the flow was still attached up to the ridge.

In the case of the boundary-layer-scaled ridge for the warm-hold case (0.125 inch high) (figure 37(b)), the pressure preceding the ridge is much greater than seen with the 0.063-inch-high ice shape, approximately -0.4 versus -1.8. Trailing-edge separation appeared to be extensive; this was confirmed by flow visualization (figure 12). The airfoil was unable to generate a substantial leading-edge suction peak due to the separation and stagnation ahead of the ridge. In fact, the secondary peak, caused by flow acceleration around the ridge, was greater in magnitude than the leading-edge suction peak. In addition, the low-pressure region caused by the ridge was greater in chordwise extent, indicating the greater extent of the separation bubble in that case. The secondary peak accounted for the fact that there was not a more significant penalty in lift at low angles of attack when compared to the effect of the 0.063-inch-high ridge (figure 27).

Pressure profiles with ridge of intermediate heights were also collected to further examine the transition of the ice shape effect from maximum lift enhancement to penalty. The leading-edge suction peak was slightly reduced in magnitude by the 0.08-inch-high ridge, compared to the 0.063-inch-high case, and the local acceleration area aft of the ridge was greater in chordwise extent. Stall was abrupt in this case. In the case of the 0.094-inch-high ridge, the local low pressure in the vicinity of the ridge was smaller in magnitude than that caused by the previous two ice shapes, reaching a minimum C_p of approximately -2.5 versus -3.0 for the shorter ice shapes. In addition, the pressure preceding the ridge was greater. That is, the stagnation region achieved a C_p of -1.0, while the previous ridges resulted in a C_p of -1.8 and -1.5 for the 0.063- and 0.08-inch-high ridges, respectively. The pressure peak near the leading edge was less than in the clean case, which accounts for the decreased C_{lmax} (figure 27). The reduction in the pressure peak was caused by the extraction of momentum by the separation bubble, which led to greater trailing-edge separation, effectively decambering the airfoil. This effect further reduced C_{lmax} as the ridge height was increased. Recall that the lift performance effect changed drastically between the 0.08- and 0.094-inch-high ridges (figure 33). The 0.094-inch-high ridge caused a performance penalty by promoting the natural trailing-edge stall of the NACA 3415. The change in stalling behavior was confirmed by flow visualization for the 0.125-inch-high ridge (figure 31), which had a similar poststall pressure distribution to the 0.094-inch-high ridge.

3.3.4 Cold Hold.

The aerodynamic effects of a geometrically scaled, 3-D ice shape simulation for the cold-hold case on the NACA 3415 and 23012 are presented in figure 38. The figure shows that the iced C_{lmax} of the NACA 23012 was reduced to 0.73, while the stalling angle of attack was reduced from 14 to 10 degrees. The NACA 3415 experienced a reduction in C_{lmax} from 1.35 to 0.9 and a 3 degree reduction in stalling angle of attack from 13 to 10 degrees (figure 38). In both cases, the stall exhibited classical thin airfoil behavior, making the stalling angle of attack and maximum lift coefficient difficult to distinguish. This behavior, due to ridge formations, has been observed in the past by Lee and Bragg [19]. The minimum drag coefficient of the NACA 23012 increased to approximately 0.026 from 0.0073 (figure 38). The minimum drag coefficient of the NACA 3415 increased similarly to 0.028 from 0.0080; however, the ridge seems to have had a much greater effect in the negative angle of attack region. In fact, figure 38 shows that the NACA 3415 has already begun to stall at -7 degrees angle of attack.

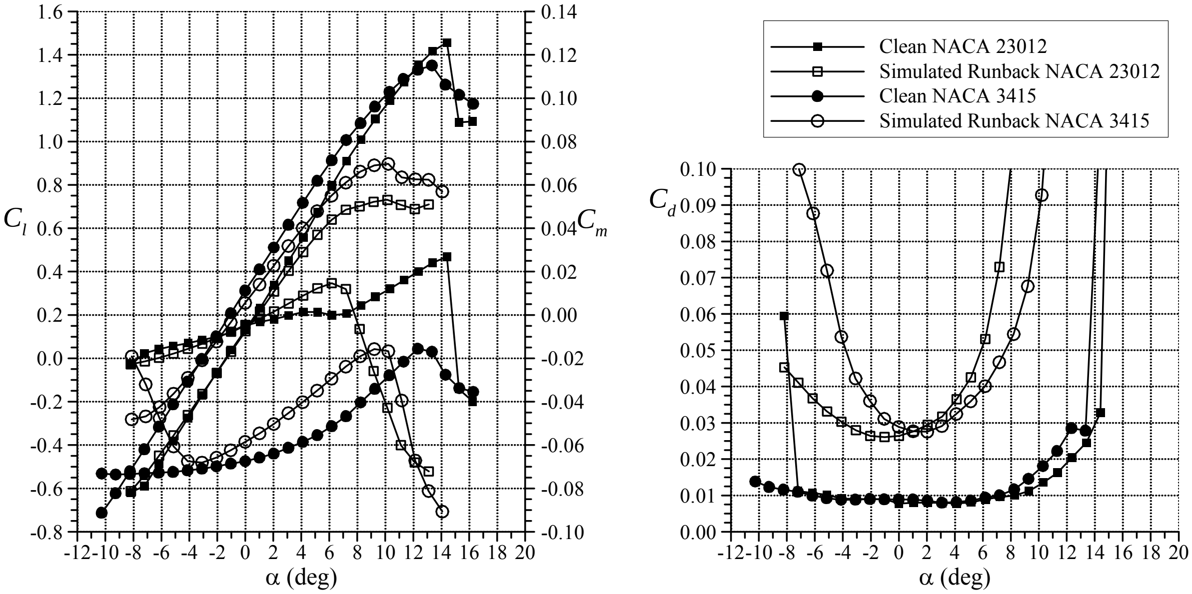

Figure 38. Effect of Ridge for the Cold-Hold Case on the Lift, Drag, and Pitching Moment of the NACA 23012 and 3415 (*Re*=1.8x10^6, M=0.18)

The performance penalties of geometrically scaled, 2-D and 3-D, cold-hold ice shape simulations on the NACA 3415 are compared in figure 39. The suction surface, 3-D ridge had a height between 0.094 and 0.125 inch and a chordwise extent of approximately 0.6 inch. The pressure surface, 3-D ridge had a height of 0.1 inch and a chordwise extent of 0.6 inch. The simulated 2-D ridge had a height of 0.125 inch and chordwise extent of 0.125 inch on the suction surface and a height of 0.094 inch and chordwise extent of 0.094 inch on the pressure surface. The suction surface ridge was attached at x/c=0.015, and the pressure surface ridge was attached at x/c=0.035. The 3-D ice shape simulation reduced the C_{lmax} to 0.90, compared to 0.97 for the 2-D simulation, and caused a loss of 3 degrees in stalling angle of attack compared to a loss of 2 degrees in the 2-D case. Chordwise extent studies conducted at x/c=0.05 with 0.125-inch-high simulations indicated that chordwise extent did not effect C_{lmax} or α_{stall}. Therefore, the greater chordwise extent of the 3-D simulation is likely not responsible for the greater penalties. The 3-D simulation did include an overhang to replicate the profile of the ice accretion, as discussed in section 3.2.1. This feature, along with the roughness, may have acted to extract greater momentum from the boundary-layer flow causing a lower C_{lmax} and α_{stall}. Drag penalty results were similar at moderate angles of attack, but were again greater in the 3-D case than in the 2-D case for angles of attack leading up to stall. The minimum drag coefficient increased to 0.028 in the 3-D case and 0.026 in the 2-D case. It is interesting to note that the drag penalty observed over the range of angle of attack tested was less than that observed for the warm-hold case. The pressure surface ridge in the warm-hold case was up to three times taller than in the cold-hold case, which was evident in the warm-hold drag polar at low and negative angles of attack.

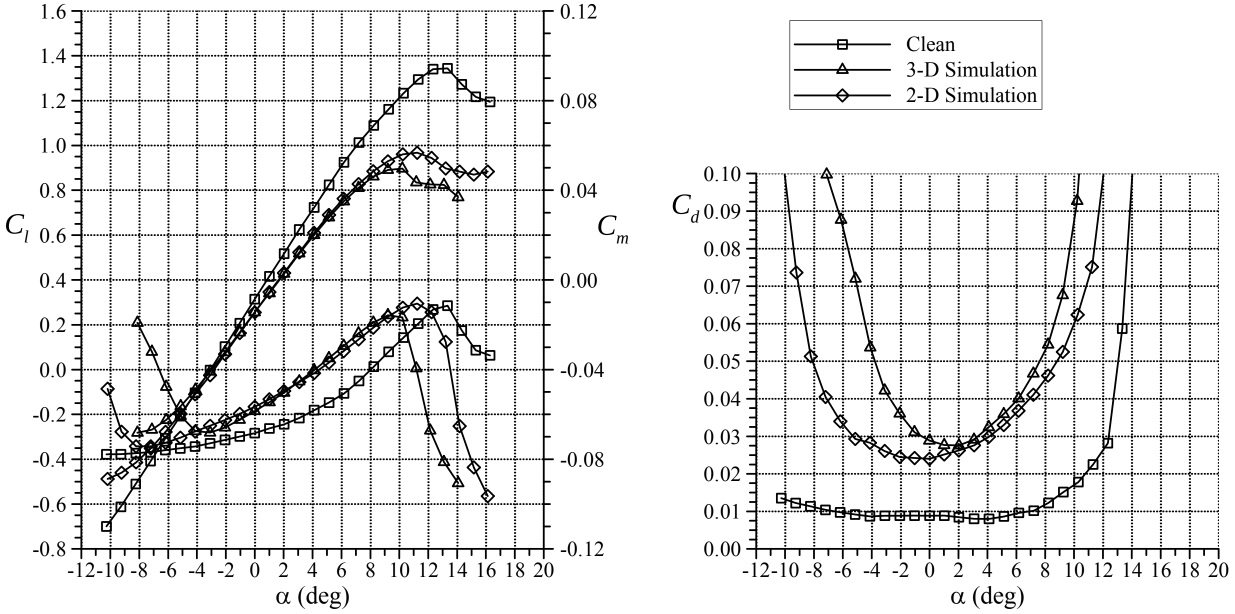

Figure 39. Comparison of the Effect of Geometrically Scaled, 2-D and 3-D Ice Shape Simulations for the Cold-Hold Case on the Lift, Drag, and Pitching Moment of the NACA 3415 (*Re*=1.8x10^6, M=0.18)

Performance penalties experienced by the NACA 23012 due to geometrically scaled, 2-D and 3-D ice shape simulations are presented in figure 40. The 3-D ice shape simulation reduced the C_{lmax} to 0.73 versus 0.81 in 2-D case. Stalling angle of attack was reduced to 9 degrees in the 2-D case and 6 degrees in the 3-D case. In this case, these numbers are based on the break in the pitching moment, defining α_{stall} since the C_l does continue to rise past that point. Again, the greater penalties associated with the 3-D simulation may be attributed to the geometry (cross section) of the shape and the added roughness. The minimum drag coefficient was increased to 0.026 in the 3-D case versus 0.020 in the 2-D case. In general, the cold-hold ice shapes had a greater effect on the NACA 23012 because of the higher pressure peak and steeper recovery that develops near the leading edge when compared to the NACA 3415. Also, the cold-hold ice shape simulations were, in general, more detrimental to the performance of the airfoils than were the warm-hold ice shape simulations.

Performance effects on the NACA 3415 of simulated 2-D, cold-hold ice shape simulations on the suction surface only are presented in figure 41. The suction surface ridges alone were tested to demonstrate the difference between the boundary-layer and geometrically scaled ice shape. The geometrically scaled, 2-D ridge was a 0.125-inch-high (k/c=0.007) section of balsa at x/c=0.028. The 2-D boundary-layer-scaled ridge was simulated using a 0.25-inch-high (*k*/c=0.014) section of balsa at x/c=0.028. The geometrically scaled ridge reduced in C_{lmax} to 0.96 and caused a 1 degree decrease in α_{stall}. The boundary-layer-scaled ridge decreased C_{lmax} to 0.72 and caused a 5 degree reduction in α_{stall}. The increase in drag was similarly more substantial at moderate to high α for the boundary-layer-scaled ridge. However, the minimum drag increase was very similar, 0.014 in the boundary-layer-scaled case versus 0.012 in the geometrically scaled case. These results are contrasted with the warm-hold results for the NACA 3415, where the geometrically scaled ridge improved the performance. In this case, both the geometrically scaled ridge and the boundary-layer-scaled ridge were over 4 times the local boundary-layer thickness in height. In fact, leading-edge ice shape simulations are typically scaled geometrically and have exhibited good agreement with full-scale tests of castings and 2-D simulations [23 and 26]. Therefore, the aerodynamic performance results using the geometrically scaled ice shape simulations should be considered representative of full scale.

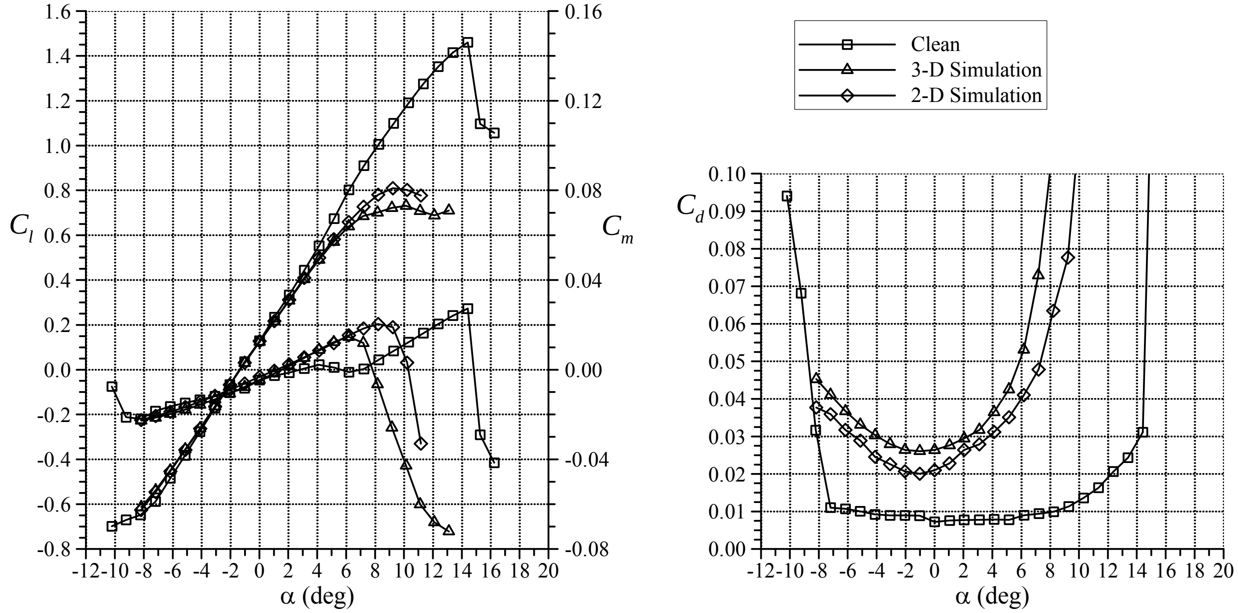

Figure 40. Comparison of the Effect of Geometrically Scaled, 2-D and 3-D Ice Shape Simulations for the Cold-Hold Case on the Lift, Drag, and Pitching Moment of the NACA 23102 (*Re*=1.8x10^6, M=0.18)

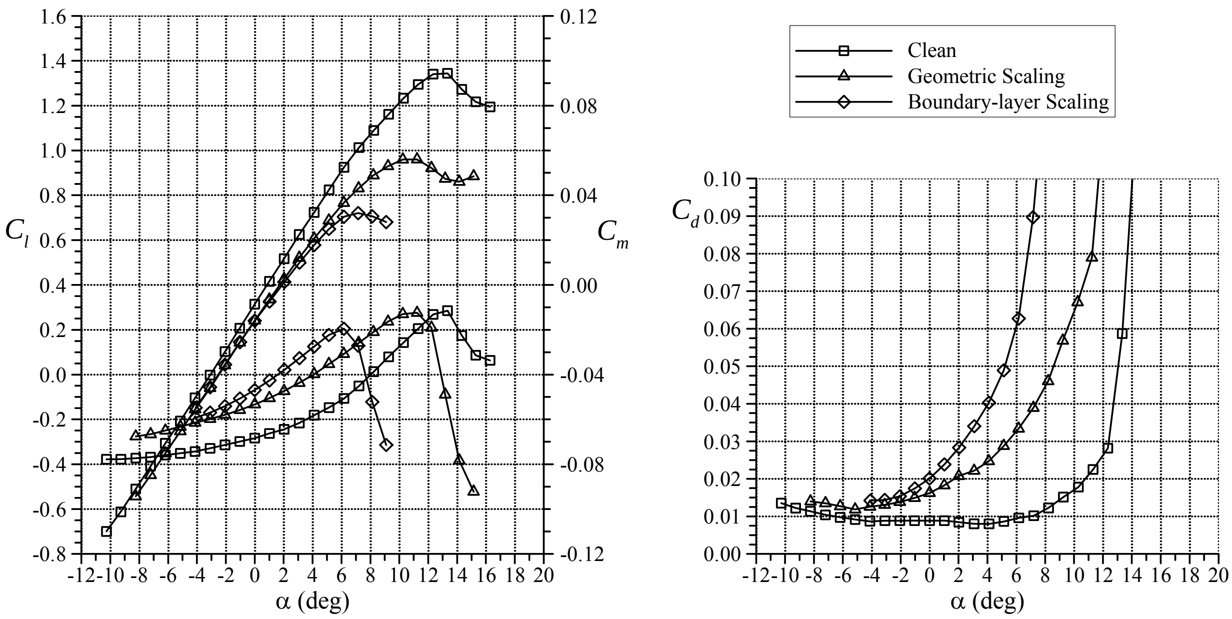

Figure 41. Effect of 2-D Ice Shape Simulation for the Cold-Hold Case on the Lift, Drag, and Pitching Moment of the NACA 3415 (Re=1.8x10^6, M=0.18)

3.3.5 Descent.

Figure 42 presents the aerodynamic effects of the 2-D ice shape simulation for the descent case. The minimum drag coefficient increased to approximately 0.014 in both cases. The maximum lift coefficient of the NACA 23012 was reduced to 0.94, and the stalling angle of attack was reduced by 3 degrees. The maximum lift coefficient of the NACA 3415 was reduced to 1.03, and the stalling angle of attack was reduced by 2 degrees. In both cases, as was seen in the cold-hold case, the stall was made relatively flat by the accretion. The penalties observed in the descent case were significant, considering that the simulated exposure time was 3.25 minutes versus 22.5 minutes for the warm- and cold-hold cases. The reduced IPS supply air temperature and mass flow rate allowed the ice accretion to grow rapidly and at a forward location, near x/c=0.01. The C_{lmax} penalty in this case was greater than in the warm-hold case, but the minimum drag was significantly less than in the warm- or cold-hold case.

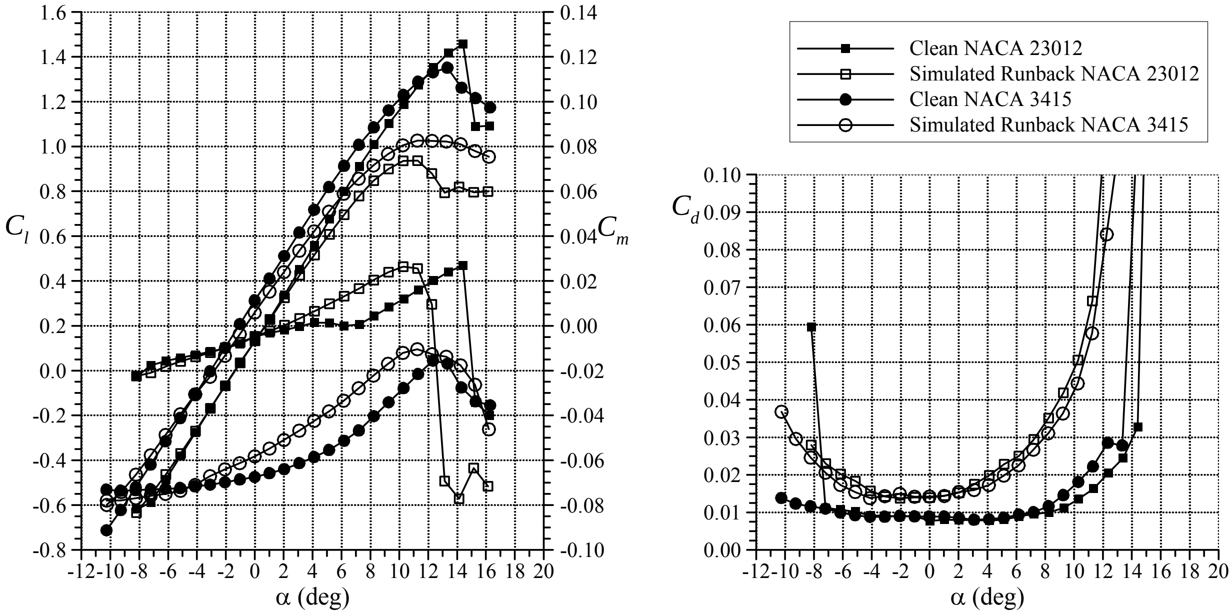

Figure 42. Effect of 2-D Ice Shape Simulation for the Descent Case on the Lift, Drag, and Pitching Moment of the NACA 23012 and 3415 (*Re*=1.8×10^6, M=0.18)

4. SUMMARY.

This report presents the results of a research program conducted to investigate the characteristics of runback ice accretions associated with a thermal, anti-ice protection system and the resulting aerodynamic effects. The overall objective was to develop a ground-based, thermal anti-icing system research capability. From the outset, it was recognized that pressure differences between flight at altitude and ground simulations could play an important role because of heat and mass transfer processes associated with the thermal IPS. Therefore, an extensive ice accretion testing campaign was conducted to evaluate various scaling methods to account for this difference and characterize the resulting runback ice accretions. Follow-on aerodynamic tests were later conducted to evaluate the performance effects of the documented ice accretion.

4.1 ICE ACCRETION TESTS.

The approach to the ice accretion testing component of this study was to use a representative, full-scale business jet wing as the test article. The model was equipped with a bleed air-based, thermal anti-icing system. The tests were designed to look at cases where the system does not evaporate 100% of the impinging water, thus leading to the formation of runback ice. The ice accretion tests were conducted at the NASA Glenn IRT. The model and ice protection system were both typical of flight hardware. The midspan chord length was 61 inches. The heated portion of the leading edge extended to x/c=0.08 on both the suction and pressure surface.

Three flight conditions were simulated in the ground test: warm-hold, cold-hold, and descent. These conditions corresponded to critical operating points in the Appendix C icing envelope due to high water catch rate, cold static temperature, and reduced IPS performance (low bleed air temperature and mass flow), respectively. All ice accretions were documented using photographs and tracings. Molds of selected accretions were also made and converted into castings for closer examination and use as guides in aerodynamic simulations. Surface temperatures were taken using thermocouples positioned at two spanwise locations in the skin of the model. The hot-air temperature and mass flow rate were also monitored during the tests. For some runs, IR temperature imaging and high-definition video were recorded.

An important part of the ice accretion tests was scaling of the external flow conditions to account for differences in pressure between flight at altitude and the near-sea-level operation of the icing tunnel. The warm- and cold-hold reference flight cases had an altitude of 15,000 feet. Methods were developed to scale these reference conditions for simulation in the icing tunnel at near-sea-level pressure. The scaling parameters used were the h, k_0, m_w, and RHF. Several combinations of these parameters were used to generate scale conditions for the warm-hold condition. It was found that scale conditions that matched h, k_0, and RHF yielded runback ice accretions that were representative of in-flight runback ice accretions as judged by collaborators that participated in the investigation. Therefore, a majority of the icing runs were scaled by holding h, k_0, and RHF constant between the reference and scale conditions.

The nominal reference flight conditions for the warm hold and cold hold were an airspeed of 200 ktas at 3 degrees α. The icing cloud conditions were based on Appendix C continuous maximum. The static air temperature was 20ºF for the warm-hold case and was -22ºF for the cold-hold case. Some of these conditions were different from those actually run in the tunnel due to the scaling methods and tunnel limitations. For the warm- and cold-hold cases, the thermal IPS was operated with the inlet bleed air temperature of 350ºF and a mass flow rate of 0.01 lbm/s/ft-span. This nominal condition was based on experience with flight hardware. For the descent case, the reference flight V was 250 ktas at -1 degree α. The T_S was -4ºF. Due to the reduce engine power associated with the descent case, the bleed air inlet temperature was 250ºF and a mass flow rate of 0.005 lbm/s/ft-span.

The runback ice accretions documented for the warm-hold flight condition were characterized by a suction and pressure surface ridge, followed by frozen rivulets downstream. The suction surface ridge in particular was characterized by features of layered frozen rivulets. There was extensive spanwise variation in the ridge height owing to many factors such as the sweep, taper, and twist of the model; the variation along the span of the bleed air temperature; and icing cloud uniformity in the tunnel. Despite the spanwise variation, the repeatability of ridge height and location was good for several different runs performed at identical conditions. At the model midspan station, the suction surface ridge was located at x/c=0.16 and had a height of k/c=0.004. The pressure surface ridge was located at x/c=0.20 and had a height of k/c=0.010. Both suction and pressure surface ridges were located well downstream of the heated portion of the leading edge, and this area upstream of the ridges was completely free of ice.

The runback ice accretions documented for the cold-hold flight condition were also characterized by suction and pressure surface ridges. The ridges were located much closer to the leading edge, on the heated portion, owing to the much lower ambient temperature. The rime ice was characterized by large accumulations that varied periodically in both height and chordwise location along the span. The spanwise variation was related to the internal orientation of the piccolo tube jets of the IPS. At the model midspan station, the suction surface ridge was located at x/c=0.015 and had height of k/c=0.006. The pressure surface ridge was located at x/c=0.035 and had height of k/c=0.006.

The combination of cold static air temperature, lower bleed air temperature, and mass flow rate led to runback ice accretion in the descent case that had the character of frost instead of frozen rivulets. The suction and pressure surface ridges had a distinct sinusoidal variation in chordwise location along the span, owing to the orientation of the piccolo tube jets. At the model midspan station, the suction surface ridge was located at x/c=0.01 and had height of k/c=0.0035. The pressure surface ridge was located at x/c=0.015 and had height of k/c=0.0016.

Additional investigations were performed for the warm-hold flight case where the static and total temperatures were varied. As a result of the scaling procedure, it was impossible to simultaneously match both the static and total temperature in the tunnel to the reference flight condition. Parametric variation of these temperatures proved to have a significant impact on the size and location of the runback ridges. As the total temperature approached 27ºF, a clear ridge was not observed and the frozen rivulets formed downstream of x/c=0.30 on the suction surface. Icing runs with parametric variations of the bleed air inlet temperature and mass flow rate were also performed for the warm-hold flight case. As expected, large changes in the runback ridge heights and locations were observed. Reduction in bleed air temperature or mass flow rate caused the ridges to both increase in height and be located closer to the leading edge.

4.2 AERODYNAMIC TESTS.

The aerodynamic effects of the runback ice accretions documented in the icing test were investigated using 3-D and 2-D ice shape simulations on subscale models. Programmatic and funding issues prohibited aerodynamic tests of the runback ice shape simulations at full scale. Therefore, 2-D airfoil models were selected that had aerodynamic characteristics of the business jet wing model used for the ice accretion tests. The NACA 3415 and 23012 airfoils were tested in the Illinois 3- by 4-foot wind tunnel at $Re=1.8 \times 10^6$ and M=0.18. The models had a chord of 18 inches and were tapped for surface pressure measurement. A force balance was used to collect lift and pitching moment directly, and a wake rake was used to measure pressure in the wake for drag calculations. Fluorescent oil flow visualization was used to investigate the flow field resulting from the ice simulations in a number of cases. Also, a small boundary-layer rake was used to measure the local velocity profiles behind selected simulations.

Since the aerodynamic tests were performed on subscale models with different airfoil shapes, simulation methods were used to represent the ice accretions documented in the icing tests. Both 2-D and 3-D simulations were tested. The 3-D simulations were built-up from simple shapes, such as sections of balsa with a rectangular cross section and grit roughness, and were meant to capture the 3-D variation in the ice accretions. The size and features of the simulations were derived from photographs, tracings, and observations of cast ice shapes. The 2-D simulations were meant to simulate the step height of the forward face of the runback ridges and usually had a square cross section. While the 3-D simulations appropriately captured the chordwise extent of the ice accretions, the 2-D simulations did not. All 3-D simulations were geometrically scaled according to the chord length of the full-scale (61 inches) and subscale models (18 inches). This geometric scaling was also used for the 2-D simulations as well as a scaling based on the ratio of the calculated local boundary-layer thickness of the clean models.

The ice shape simulations were found to cause substantial penalties to the aerodynamic performance of both the NACA 23012 and the 3415. Geometrically scaled, 3-D, warm-hold ice shape simulations were found to reduce the C_{lmax} of the NACA 3415 to 1.16 from a clean value of 1.35 and reduce the stalling angle of attack by 1 degree. The same ice shape simulations reduced the C_{lmax} of the NACA 23012 to 1.16 from a clean value of 1.46 and caused a 2 degree reduction in stalling angle of attack. For both airfoils, the minimum drag coefficient increased to approximately 0.035 due to the warm-hold shape. Geometrically scaled, 3-D ice shape simulations for the cold-hold case reduced the C_{lmax} of the NACA 3415 to 0.9 and led to a 3 degree reduction in stalling angle of attack, while the NACA 23012 experienced a reduction in C_{lmax} to 0.73 and a loss of 4 degrees in stalling angle of attack. The minimum drag coefficient increased to approximately 0.027 in both cases. Geometrically scaled, 3-D ice shape simulations for the descent case led to a reduction of C_{lmax} of the NACA 3415 to 1.02 and led to a 2 degree reduction in stalling angle of attack, while the NACA 23012 experienced a reduction in C_{lmax} to 0.94 and a loss of 3 degrees in stalling angle of attack. The minimum drag coefficient increased to approximately 0.014 in both cases.

Discrepancies between the 3-D ice shape simulations and their 2-D counterparts were largest for the warm-hold case and led to a number of parametric investigations. The effect of surface extent of the 2-D simulations was explored by using rectangular shapes in addition to the square ones. The height of the shape was held constant while the length was increased. This was seen to affect both maximum lift and drag and could be an important factor in the aerodynamic simulation of runback ice accretions.

Discrepancies between the 3-D ice shape simulations and their 2-D counterparts also motivated investigations on the effect of ridge height for the warm-hold case. The geometrically scaled, 2-D ice shape simulations had height of $k/c=0.0035$ and were located at $x/c=0.16$ on the suction surface. This resulted in only a minor effect on maximum lift of the NACA 23012 airfoil. However, for the NACA 3415 airfoil, the stalling angle of attack was increased by 4 degrees and C_{lmax} was increased to 1.51 from a clean value of 1.35. Two phenomena were identified that contributed to this phenomenon. First, the generation of a small separation bubble acted to energize the boundary layer and caused the trailing-edge separation to progress forward more slowly with angle of attack. Second, a low-pressure region and secondary pressure recovery setup by the ridge allowed the leading-edge suction peak to grow past the clean peak. This lift enhancement led to the testing of a boundary-layer-scaled ridge, which had height of $k/c=0.007$ and was also located at $x/c=0.16$ on the suction surface. The effect on the NACA 3415 airfoil was to reduce the stalling angle of attack by 2 degrees and the C_{lmax} to 0.95.

5. CONCLUSIONS.

5.1 ICE ACCRETION TESTS.

The ice accretion tests yielded several important conclusions about thermal scaling of external flow conditions for thermal ice protection systems. The foremost of these is that the warm-temperature cases appear to be the most important for thermal scaling. For the warm-hold case, total temperatures in the range of 23° to 30°F had a large effect on the resulting runback ridge height and location. Because these scaling methods required the test airspeed to be lower than in the flight case, it was impossible to match both static and total temperature. Since there was a large dependence of the ice accretion on temperature, it was not clear what temperature should be matched. Calculations performed after the icing tests suggest that the temperature could be selected based upon matching the stagnation point freezing fraction on the unprotected surface. This approach deserves consideration in future testing. For the cold-hold and descent cases, the static and total temperatures were low, such that the stagnation point freezing fraction of the unprotected surface was 1.0. This implied that matching the temperature in the scale case to the reference is not nearly as critical. The tests conducted here support this conclusion. For cases with cold reference flight conditions, it is likely most important to match the modified droplet inertia parameter and the water catch rate. The convective heat transfer coefficient has less importance.

The warm-hold flight condition presents a challenging problem for testing of thermal ice protection systems in ground-based facilities without altitude simulation. The large dependence on static and total temperature is an important consideration. This analysis also made assumptions about the mass transfer effects governing the evaporation of the runback water on the model surface. Attempts to quantify this effect proved to be very difficult and should be considered in any future work.

5.2 AERODYNAMIC TESTS.

Previous iced-airfoil aerodynamic tests performed on various scale models and over a large range of Reynolds numbers ($1.0x10^6$ to $10.0x10^6$) has shown that geometric scaling of ice accretion simulations yields excellent results. For these cases, which dealt mainly with leading-edge and large-ridge simulations, the characteristic heights were much larger than the local boundary-layer thickness. For the present series of runback ice accretion, this is also true for the cold-hold and descent cases. Therefore, the aerodynamic results presented here for geometrically scaled, 3-D and 2-D simulations applied to the National Advisory Committee for Aeronautics (NACA) 23012 and 3415 are representative for these types of accretions.

In the case of the warm-hold ice accretions, the fact that the airfoil is clean leading up to the ice shapes, that the ridges are relatively short, and that the ridges are quite far aft results in Reynolds number considerations and effects potentially being important to characterizing the aerodynamic penalties of these ice shapes. The boundary-layer scaling method employed here was an attempt to ascertain the potential aerodynamic penalties of the warm-hold accretions. However, the authors are unaware of any studies where this has been demonstrated as a valid method. If, in fact, the boundary-layer thickness plays an important role in scaling these accretions, then the Reynolds number dependence may be larger than previously observed in iced-airfoil aerodynamics. This is due simply to the direct dependence of boundary-layer thickness upon Reynolds number.

6. RECOMMENDATIONS.

Several recommendations arise from this work. The effect of the scaling parameters on runback ice accretions should be further investigated, particularly for warm-temperature cases. It is important to confirm the ability of the scaling methods to accurately reproduce runback accretions. The selection of appropriate scale temperature should be an important consideration. To accomplish this, a database of full-scale runback accretions, either from carefully controlled flight tests or icing tunnel tests where altitude scaling is not required, should be performed. Testing in a pressurized icing wind tunnel is recommended to achieve this goal because the reference altitude can be simulated.

There are currently no public data regarding the aerodynamic effects of runback ice shape simulations on airfoils at full-scale Reynolds number. Therefore, there is little to which these results can be compared. Full-scale Reynolds number aerodynamic investigations of full-scale, high-fidelity simulations of runback ice shape simulations are recommended to accurately characterize the aerodynamic performance effects of these shapes. Alternatively, full-scale Reynolds number tests of scaled high-fidelity and simple runback ice shape simulations would provide valuable information regarding the aerodynamic performance penalties and the role of Reynolds number. Either approach could be used to evaluate boundary-layer thickness scaling methods and determine when this becomes an important consideration relative to geometric scaling.

7. REFERENCES.

1. Gray, V.H. and von Glahn, U.H., "Effect of Ice and Frost Formations on Drag of NACA 651-212 Airfoil for Various Modes of Thermal Ice Protection," NACA TN-2962, June 1953.

2. Al-Kahlil, K.M., Miller, D., and Wright, W., "Validation of Thermal Ice Protection Computer Codes: Part 3 – The Validation," AIAA 97-0051, Reno, NV, January 1997.

3. Boeke, F.L. and Paselik, R.A., "Icing Problems and the Thermal Anti-Icing System," I.A.S. Meeting, Los Angeles, CA, August 16-17, 1945.

4. Anderson, D.N., "Manual of Scaling Methods," NASA/CR 2004-212875, March 2004.

5. Oleskiw, M.M., De Gregorio, F., and Esposito, B., *The Effect of Altitude on Icing Tunnel Airfoil Icing Simulation*, Proceedings of the FAA International Conference on Aircraft Inflight Icing, Vol. II, DOT/FAA/AR-96/81, August 1996, pp. 511-520.

6. Bartlett, C.S., "Inflight Scaling Considerations for Aircraft Engine Testing," AIAA 88-88-0202, January 1988.

7. Jacobs, E.N., "Airfoil Characteristics as Affected by Protuberances," NACA Report 446, 1932.

8. Lee, S., "Effect of Supercooled Large Droplet Icing on Airfoil Aerodynamics," Ph.D. Dissertation, Dept. of Aeronautical and Astronautical Eng., Univ. of Illinois, Urbana, IL, 2001.

9. Calay, R.K., Holdo, A.E., and Mayman, P., "Experimental Simulation of Runback Ice," *Journal of Aircraft*, Vol. 34, No. 2, March-April 1997.

10. Papadakis, M. and Gile-Laflin, B.E., "Aerodynamic Performance of a Tail Section With Simulated Ice Shapes and Roughness," AIAA 2001-0539, Reno, NV, January 2001.

11. Whalen, E.A., Broeren, A.P., Bragg, M.B., and Lee, S., "Characteristics of Runback Ice Accretions on Airfoils and their Aerodynamic Effects," AIAA 2005-1065, Reno, NV, January 2005.

12. Whalen, E.A., Broeren, A.P., and Bragg, M.B., "Considerations for Aerodynamic Testing of Scaled Runback Ice Accretions," AIAA 2006-0260, Reno, NV, January 2006.

13. Wright, W.B., "User Manual for the NASA Lewis Ice Accretion Code LEWICE 2.0," NASA CR 209409, January 1999.

14. Anderson, David N., "Manual of Scaling Methods," NASA CR 2004-212875, March 2004.

15. Chapman, A.J., *Heat Transfer*, 4th Edition, MacMillan, New York, 1984, p. 243.

16. Rae, W.H. and Pope, A., *Low-Speed Wind Tunnel Testing*, Wiley, New York, 1984, pp. 349-362.

17. Kline, S.J. and McClintock, F.A., "Describing Uncertainties in Single-Sample Experiments," *Mechanical Engineering*, Vol. 75, January 1953, pp. 3-8.

18. Coleman, H.W. and Steele, W.G., *Experimentation and Uncertainty Analysis for Engineers*, John Wiley and Sons, New York, 1989, pp. 40-118.

19. Lee, S. and Bragg, M.B., "Experimental Investigation of Simulated Large-Droplet Ice Shapes on Airfoil Aerodynamics," *Journal of Aircraft*, Vol. 36, No. 5, September-October 1999, pp. 844-850.

20. Drela, Mark, XFOIL Subsonic Airfoil Development System, *http://raphael.mit.edu/xfoil/*.

21. McCullough, G.B. and Gault, D.E., "Examples of Three Representative Types of Airfoil-Section Stall at Low Speed," NACA TN-2502, Washington, September 1951.

22. Broeren, A.P. and Bragg, M.B., "Effect of Airfoil Geometry on Performance With Simulated Intercycle Ice Accretions," AIAA 2003-0728, Reno, NV, January 2003.

23. Broeren, A.P., Lee, S., LaMarre, C.M., and Bragg, M.B., "Effect of Airfoil Geometry on Performance with Simulated Ice Accretions Volume 1: Experimental Investigation," DOT/FAA/AR-03/64, August 2003.

24. White, F.M., *Viscous Fluid Flow*, 2nd Edition, McGraw-Hill, 1991, pp. 242-247.

25. Coles, D., "The Law of the Wake in the Turbulent Boundary-Layer," *J. Fluid Mechanics*, Vol. 1, pp. 191-226, 1956.

26. Broeren, A.P. and Bragg, M.B., "Effect of Airfoil Geometry on Performance With Simulated Intercycle Ice Accretions," *Journal of Aircraft*, Vol. 42, No. 1, January-February 2005, pp.121-130.

APPENDIX A—ICING RESEARCH TUNNEL RUN LOGS

Tables A-1 through A-16 show Icing Research Tunnel (IRT) run logs from September 8-19, 2003, and October 24-28, 2003.

Table A-1. The IRT Runback Test Run Log for September 8, 2003

								Bleed Air				
Run No.	T_{total} (F)	T_{static} (F)	Airspeed (ktas)	Spray Time (min.)	AOA (deg)	MVD (mm)	LWC (g/m^3)	Temp. (F)	Press. (psi)	mdot (lbm/s/ft)	Escort Files	IR Images
1	23.1	20.0	115	N/A	3	N/A	N/A	368	49.2	0.020	14103	Capture1
2	23.1	20.0	115	N/A	3	N/A	N/A	353	72.2	0.030	14104	Capture2
3	23.1	20.0	115	N/A	3	N/A	N/A	363	86.9	0.036	14105	Capture3
4	23.1	20.0	115	N/A	3	29	0.87	368	86.2	0.036	14106	Run1
5	23.1	20.0	115	N/A	3	29	0.87	356	73.5	0.031	14107	Run1a
6	23.1	20.0	115	N/A	3	29	0.87	354	39.1	0.020	14108	Run1b
7	23.1	20.0	115	N/A	3	29	0.87	347	27.2	0.010	14109	Run1c
8	23.1	20.0	115	N/A	3	29	0.87	350	19.3	0.005	14110	Run1d
9	23.1	20.0	115	N/A	3	29	0.87	343	16.8	0.004	14111	Run1e

AOA = Angle of attack
mdot = Mass flow rate of hot air
MVD = Medium volumetric diameter
LWC = Liquid water content
IR = Infrared
N/A = Not applicable

Table A-2. The IRT Runback Test Run Log for September 9, 2003

								Bleed Air				
Run No.	T_{total} (F)	T_{static} (F)	Airspeed (ktas)	Spray Time (min.)	AOA (deg)	MVD (mm)	LWC (g/m^3)	Temp. (F)	Press. (psi)	mdot (lbm/s/ft)	Escort Files	IR Images
NG0628	23.1	20.0	115	22.5	3	29	0.87	355	37.9	0.015	14112 through 14114	IR628
NG0629	23.1	20.0	115	22.5	3	??	??	356	26.8	0.010	14115 through 14117	IR629, IR629A
NG0630	23.1	20.0	115	22.5	3	29	0.87	354	18.5	0.005	14119 through 14122	IR630, IR630A
NG0631	25.6	20.0	154	22.5	3	26	0.82	355	28.4	0.010	14123 through 14126	IR631, IR631A
NG0632	23.1	20.0	115	22.5	3	29	0.87	354	27.1	0.010	14129 through 14132	IR632, IR632A

Table A-3. The IRT Runback Test Run Log for September 10, 2003

								Bleed Air				
Run No.	T_{total} (F)	T_{static} (F)	Airspeed (ktas)	Spray Time (min.)	AOA (deg)	MVD (mm)	LWC (g/m^3)	Temp. (F)	Press. (psi)	mdot (lbm/s/ft)	Escort Files	IR Images
NG0633	23.1	20.0	115	22.5	3	29	0.87	352	27.3	0.010	14134 through 14137	IR633, IR633A
NG0634	26.7	20.0	168	22.5	3	25	0.6	350	27.5	0.010	14138 through 14141	IR634, IR634A
NG0635	23.1	20.0	115	45	3	29	0.87	350	18.6	0.005	14142 through 14156	IR635, IR635A
NG0636	23.1	20.0	115	22.5	3	29	0.87	354	27	0.010	14147 through 14150	IR636, IR636A
NG0637	23.1	20	115	45	3	29	0.87	356	18.7	0.005	14151 through 14154	IR637, IR637A

Table A-4. The IRT Runback Test Run Log for September 11, 2003

								Bleed Air				
Run No.	T_{total} (F)	T_{static} (F)	Airspeed (ktas)	Spray Time (min.)	AOA (deg)	MVD (mm)	LWC (g/m^3)	Temp. (F)	Press. (psi)	mdot (lbm/s/ft)	Escort Files	IR Images
N/A	23.1	20.0	115	10.0	3	N/A	N/A	250	N/A	0.010	N/A	N/A
NG0638	23.1	20.0	115	22.5	3	29	0.87	250	25.9	0.010	14156 through 14159	IR638, IR638A
NG0639	25.6	20.0	154	22.5	3	26	0.82	250	26.4	0.010	14160 through 14162a	IR639, IR639A
NG0640	23.1	20.0	115	45	3	29	0.87	351	26.7	0.010	14163 through 14167	IR640, IR640A
NG0641	23.1	20.0	115	45	3	29	0.87	352	27.1	0.010	14168 through 14173	IR641, IR641A

Table A-5. The IRT Runback Test Run Log for September 12, 2003

								Bleed Air				
Run No.	T_{total} (F)	T_{static} (F)	Airspeed (ktas)	Spray Time (min.)	AOA (deg)	MVD (mm)	LWC (g/m^3)	Temp. (F)	Press. (psi)	mdot (lbm/s/ft)	Escort Files	IR Images
N/A	23.1	20.0	115	15.0	3	??	??	350		0.01	N/A	N/A
NG0642	23.1	20.0	115	22.5	3	29	0.87	349	27.7	0.010	14174 through 14177	IR642, IR642A
NG0643	26.7	20.0	168	22.5	3	25	0.60	349	28.1	0.010	14178 through 14181	IR643, IR643A
NG0644	-19.1	-22.0	110	8.6	3	29	0.69	350	27.9	0.010	14182 through 14185	IR644, IR644A
NG0645	-19.1	-22.0	110	8.6	3	29	0.69	353	48.6	0.020	14186 through 14189	IR645, IR645A
NG0646	-19.1	-22.0	110	19.1	3	29	0.69	351	28.9	0.010	14182 through 14185	IR644, IR644A

Table A-6. The IRT Runback Test Run Log for September 13, 2003

								Bleed Air				
Run No.	T_{total} (F)	T_{static} (F)	Airspeed (ktas)	Spray Time (min.)	AOA (deg)	MVD (mm)	LWC (g/m^3)	Temp. (F)	Press. (psi)	mdot (lbm/s/ft)	Escort Files	IR Images
N/A	23.1	20.0	115	15.0	3	??	??	N/A	N/A	N/A	N/A	N/A
NG0647	23.1	20.0	115	22.5	3	29	0.87	250	26.2	0.010	14194 through 14197	IR647, IR647A
NG0648	23.1	20.0	115	22.5	3	133	0.57	348	28.7	0.010	14198 through 14201	IR648, IR648A
NG0649	26.7	20.0	168	45	3	25	0.60	351	28.1	0.010	14202 through 14206	IR649, IR649A
NG0650	23.1	20.0	115	22.5	3	133	0.57	353	27.8	0.010	14207 through 14210	IR650, IR650A

Table A-7. The IRT Runback Test Run Log for September 15, 2003

								Bleed Air				
Run No.	T_{total} (F)	T_{static} (F)	Airspeed (ktas)	Spray Time (min.)	AOA (deg)	MVD (mm)	LWC (g/m^3)	Temp. (F)	Press. (psi)	mdot (lbm/s/ft)	Escort Files	IR Images
N/A	19.9	16.8	115	15	3	??	??	N/A	N/A	N/A	N/A	N/A
NG0651	23.1	20.0	115	22.5	3	29	0.87	253	26.1	0.010	14211 through 14214	IR651, IR651A
NG0652	-19.1	-22.0	110	8.6	3	29	0.69	252	26.6	0.010	14215 through 14218	IR652, IR652A
NG0653	-15.9	-22.0	160	8.6	3	20	0.4	353	28.3	0.010	14219 through 14222	IR653, IR653A
NG0654	-15.9	-22.0	160	6	3	20	0.4	355	29	0.015	14223 through 14226	IR654, IR654A
NG0655	-19.1	-22.0	110	8.6	3	29	0.69	349	27	0.010	14226 through14229	IR655, IR655A

Table A-8. The IRT Runback Test Run Log for September 16, 2003

								Bleed Air				
Run No.	T_{total} (F)	T_{static} (F)	Airspeed (ktas)	Spray Time (min.)	AOA (deg)	MVD (mm)	LWC (g/m^3)	Temp. (F)	Press. (psi)	mdot (lbm/s/ft)	Escort Files	IR Images
N/A		Ambient	205	None	3	N/A	N/A	N/A	N/A	N/A	N/A	
N/A		Ambient	250	None	1	N/A	N/A	N/A	N/A	N/A	N/A	
N/A	19.9	16.8	115	15	3	??	??	N/A	N/A	N/A	N/A	N/A
N/A	28.0	18	205	N/A	3	24	0.49	350	N/A	.036 - .01	14231 through 14235	evap9-16, evap9-16a through d
NG0656	28.0	18.0	205	22.5	3	24	0.49	350	28.2	0.010	14236 through 14239	IR656, IR656A
NG0657	26.7	20.0	168	22.5	3	188	0.65	350	28.6	0.010	14240 through 14243	IR657, IR657A
NG0658	28.0	13.2	250	22.5	1.1	23	0.51	351	28.3	0.010		IR658, IR658A
NG0659	17.9	13.2	141	22.5	1.1	28	0.91	345	28.3	0.010	14248 through 14251	IR659, IR659A

Table A-9. The IRT Runback Test Run Log for September 17, 2003

								Bleed Air				
Run No.	T_{total} (F)	T_{static} (F)	Airspeed (ktas)	Spray Time (min.)	AOA (deg)	MVD (mm)	LWC (g/m^3)	Temp. (F)	Press. (psi)	mdot (lbm/s/ft)	Escort Files	IR Images
N/A	19.9	16.8	115	15	1.1	??	??	N/A	N/A	N/A	N/A	N/A
NG0660	28	23.3	141	22.5	1.1	28	0.91	351	29	0.010	14252, 14253, 14254, 14255	IR660, IR660A
NG0661	23.1	13.1	205	22.5	1.1	24	0.49	351	28.2	0.010	14256, 14257, 14258, 14259	IR661, IR661A
NG0662	22.9	18.2	141	22.5	1.1	28	0.91	348	29.5	0.010	14260, 14261, 14262, 14263	IR662, IR662A
NG0663	-11	-21.0	205	7.9	1.1	23	0.4	351	28.3	0.010	14264, 14265, 14266, 14267	IR663, IR663A
NG0664	-5.5	-20.5	250	2.0	1.1	23	0.4	358	28.6	0.010	14268, 14269, 14270	IR664
NG0665	-5.5	-20.5	250	2.0	1.1	23	0.4	350	28.5	0.010	14271, 14272, 14273, 14274	IR665

Table A-10. The IRT Runback Test Run Log for September 18, 2003

								Bleed Air				
Run No.	T_{total} (F)	T_{static} (F)	Airspeed (ktas)	Spray Time (min.)	AOA (deg)	MVD (mm)	LWC (g/m^3)	Temp. (F)	Press. (psi)	mdot (lbm/s/ft)	Escort Files	IR Images
N/A	2.0	??	115	15	-1	??	??	N/A	N/A	N/A	N/A	N/A
NG0666	4.9	-4.0	194	1.7	-1	25	0.4	148	16.3	0.005	14275, 14276, 14277, 14278	IR666
NG0667	4.9	-4.0	194	3.5	-1	25	0.4	152	16.5	0.005	14279, 14280, 14281, 14282	IR667
NG0668	4.9	-4.0	194	1.7	-1	25	0.4	248	17.6	0.005	14284, 14285, 14286, 14287	IR668
NG0669	4.9	-4.0	194	3.5	-1	25	0.4	253	18.1	0.005	14288, 14289, 14290, 14291	IR669
NG0670	22.9	7.9	250	22.5	1.1	23	0.51	349	29.2	0.010	14292, 14293, 14294, 14295	IR670, IR670A
NG0671	22.9	18.2	141	22.5	1.1	28	0.91	352	27.9	0.010	14296, 14297, 14298, 14299	IR671, IR671A

Table A-11. The IRT Runback Test Run Log for September 19, 2003

								Bleed Air				
Run No.	T_{total} (F)	T_{static} (F)	Airspeed (ktas)	Spray Time (min.)	AOA (deg)	MVD (mm)	LWC (g/m^3)	Temp. (F)	Press. (psi)	mdot (lbm/s/ft)	Escort Files	IR Images
NG0672	23.1	20.0	115	22.5	3	29	0.87	N/A	N/A	N/A	14300, 14301, 14302	N/A
NG0673	26.7	20.0	168	22.5	3	25	0.6	N/A	N/A	N/A	14303, 14304, 14305	N/A
NG0674	23.1	13.0	205	22.5	3	23.5	0.39	351	27.8	0.010	14306, 14307, 14308, 14309	N/A
NG0675	22.9	18.2	141	22.5	1.1	28	0.91	N/A	N/A	N/A	14310, 14311, 14312	N/A
NG0676	-19.1	-22.0	110	8.6	3	29	0.69	N/A	N/A	N/A	14313, 14314, 14315	N/A

Table A-12. The IRT Runback Test Run Log for October 24, 2004

								Bleed Air				
Run No.	T_{total} (F/C)	T_{static} (F/C)	Airspeed (ktas)	Spray Time (min.)	AOA (deg)	MVD (mm)	LWC (g/m^3)	Temp. (F/C)	Press. (psi)	mdot (lbm/s/ft)	Escort Files	IR Images
1	23.0/-5.0	19.9/-6.8	115	No Spray	3							
2	23.0/-5.0	19.9/-6.8	115	15	3			250/121		0.010		
CG0879	23.0/-5.0	19.9/-6.8	115	22.5	3	29	0.87	250/121	25.6	0.010	879	
CG0880	25.6/-3.5	19.9/-6.8	154	22.5	3	26	0.82	250/121	25.4	0.010	880	
CG0881	29.9/-1.2	26.8/-2.9	115	22.5	3	29	0.87	250/121	25.4	0.010	881	
CG0882	23.0/-5.0	19.9/-6.7	115	22.5	3	29	0.87	350/177	27.7	0.010	882	
CG0883	29.9/-1.2	26.8/-2.9	115	22.5	3	29	0.87	350/177	27.7	0.010	883	

Table A-13. The IRT Runback Test Run Log for October 25, 2004

								Bleed Air				
Run No.	T_{total} (F/C)	T_{static} (F/C)	Airspeed (ktas)	Spray Time (min.)	AOA (deg)	MVD (mm)	LWC (g/m^3)	Temp. (F/C)	Press. (psi)	mdot (lbm/s/ft)	Escort Files	IR Images
1	23.0/-5.0	19.9/-6.8	115	15	3							
CG0884	23.0/-5.0	19.9/-6.8	115	22.5	3	29	0.87	350/177	27.47	0.010	884	884, 884a
CG0885	25.0/-3.9	21.9/-5.6	115	22.5	3	29	0.87	350/177	27.7	0.010	885	885, 885a
CG0886	27.0/-2.8	23.8/-4.6	115	22.5	3	29	0.87	350/177	27.5	0.010	886	886, 886a
CG0887	28.5/-1.9	25.4/-3.7	115	22.5	3	29	0.87	350/177	27.9	0.010	887	887, 887a
CG0888	24.7/-4.1	20.0/-6.7	141	45	1	28	0.91	350/177	27.7	0.010	888	888, 888a

Table A-14. The IRT Runback Test Run Log for October 26, 2004

								Bleed Air				
Run No.	T_{total} (F/C)	T_{static} (F/C)	Airspeed (ktas)	Spray Time (min.)	AOA (deg)	MVD (mm)	LWC (g/m^3)	Temp. (F/C)	Press. (psi)	mdot (lbm/s/ft)	Escort Files	IR Images
1	23.0/-5.0	19.9/-6.8	115	15	3	-	-	350/177		0.010	-	-
CG0889	23.0/-5.0	19.7/-6.8	115	22.5	3	29	0.87	350/177	28.1	0.010	889	889, 889a
CG0890	23.0/-5.0	13.4/-10.3	205	22.5	3	24	0.49	350/177	27.7	0.010	890	890, 890a
CG0891	27.0/-2.8	17.2/-8.2	205	22.5	3	24	0.49	350/177	27.2	0.010	891	891, 891a
CG0892	30.0/-1.2	19.9/-6.7	205	22.5	3	24	0.49	350/177	27.8	0.010	892	892, 892a
CG0893	24.7/-4.1	20.2/-6.6	141	45	1	28	0.91	350/177	27.2	0.010	893	893, 893a

Table A-15. The IRT Runback Test Run Log for October 27, 2004

								Bleed Air				
Run No.	T_{total} (F/C)	T_{static} (F/C)	Airspeed (ktas)	Spray Time (min.)	AOA (deg)	MVD (mm)	LWC (g/m^3)	Temp. (F)	Press. (psi)	mdot (lbm/s/ft)	Escort Files	IR Images
1	23.0/-5.0	19.9/-6.8	115	15	3	-	-	350/177		0.010	-	-
CG0894	24.7/-4.1	20.2/-6.6	141	22.5	1	28	0.91	350/177	27.8	0.010	894	894, 894a
CG0895	24.7/-4.2	20.2/-6.7	141	22.5	1	28	0.91	351/177	27.8	0.010	895	895, 895a
CG0896	26.0/-3.4	19.7/-6.8	159	22.5	3	25	0.62	350/177	27.7	0.010	896	896, 896a
CG0897	26.0/-3.4	19.7/-6.8	159	22.5	3	20	0.62	350/177	27.7	0.010	897	897, 897a
CG0898	24.7/-4.1	20.2/-6.6	141	45	1	28	0.91	350/177	27.8	0.010	898	898, 898a
CG0899	23.0/-5.0	19.9/-6.8	115	5	3	29	0.87	325/163	27.4	0.010	899	899
CG0900	23.0/-5.0	19.9/-6.8	115	22.5	3	29	0.87	300/150	27.0	0.010	900	900, 900a

Table A-16. The IRT Runback Test Run Log for October 28, 2004

								Bleed Air				
Run No.	T_{total} (F/C)	T_{static} (F/C)	Airspeed (ktas)	Spray Time (min.)	AOA (deg)	MVD (mm)	LWC (g/m^3)	Temp. (F)	Press. (psi)	mdot (lbm/s/ft)	Escort Files	IR Images
1	23.0/-5.0	19.9/-6.8	115	15	3	-	-	350/177		0.010	-	-
CG0901	23.0/-5.0	19.9/-6.8	115	22.5	3	28	0.91	250/121	26.6	0.010	901	901, 901a
CG0902	23.0/-5.0	19.9/-6.8	115	5.0	3	28	0.91	275/135	26.6	0.010	902	902, 902a
CG0903	29.9/-1.2	26.8/-2.9	115	5.0	3	28	0.91	300/150	26.2	0.010	903	903, 903a
CG0904	23.0/-5.0	19.8/-6.8	115	22.5	3	28	0.91	350/177	18.7	0.005	904	904, 904a
CG0905	23.0/-5.0	19.8/-6.8	115	5.0	3	28	0.91	350/177	49.6	0.020	905	905, 905a
CG0906	23.0/-5.0	19.8/-6.8	115	5.0	3	28	0.91	350/177	71.9	0.030	906	906, 906a
CG0907	23.0/-5.0	19.8/-6.8	115	5.0	3	28	0.91	350/177	92.8	0.040	907	907, 907a
CG0908	23.2/-4.9	14.0/-10	200	2.0	3	100	0.29	N/A	N/A	N/A	908	-

APPENDIX B—TOTAL TEMPERATURE VARIATION RESULTS

Appendix B presents detailed run conditions and ice accretion photographs for the Icing Research Tunnel runs conducted to explore the effect of total temperature on the formation of runback icing. Table B-1 summarizes the ice height and ridge chordwise location for each run, the figure corresponding to each condition is also listed.

Table B-1. Effect of Total Temperature Variation of Ice Ridge Height and Chordwise Location

			Suction Surface		Pressure Surface	
Figure in Appendix	T_s (^oF)	T_0 (^oF)	Avg. Ice Height (in.)	Ridge Location (x/c)	Avg. Ice Height (in.)	Ridge Location (x/c)
B-1	19.9	23.0	0.21	0.15	0.66	0.23
B-2	21.9	25.0	0.36	0.19	0.36	0.28
B-3	23.8	27.0	0.36	0.30	0.25	0.34
B-4	25.4	28.5	0.13	0.40	**	0.60*
B-5	26.8	30.0	**	0.50*	**	0.80*

* Accretion aft of tracing, estimated.

** Accretion aft of tracing, no measurement.

								Bleed Air		
Run No.	T_{total} (F/C)	T_{static} (F/C)	Airspeed (ktas)	Spray Time (min.)	AOA (deg)	MVD (mm)	LWC (g/m^3)	Temp. (F/C)	Press. (psi)	mdot (lbm/s/ft)
CG0884	23.0 /-5.0	19.9 /-6.8	115	22.5	3	29	0.87	350 /177	27.47	0.010

Figure B-1. Warm-Hold Run at a Total Temperature of 23.0°F. (The top shows the conditions for the run. Clockwise from the upper left are photographs showing the suction surface looking downstream, the pressure surface looking downstream, a close-up of the pressure surface, and a close-up of the suction surface.)

Run No.	T_{total} (F/C)	T_{static} (F/C)	Airspeed (ktas)	Spray Time (min.)	AOA (deg)	MVD (μm)	LWC (g/m^3)	Temp. (F/C)	Press. (psi)	mdot (lbm/s/ft)
CG0885	25.0 /-3.9	21.9 /-5.6	115	22.5	3	29	0.87	350 /177	27.7	0.010

Figure B-2. Warm-Hold Run at a Total Temperature of 25.0°F. (The top shows the conditions for the run. Clockwise from the upper left are photographs showing the suction surface looking downstream, the pressure surface looking downstream, a close-up of the pressure surface, and a close-up of the suction surface.)

Run No.	T_{total} (F/C)	T_{static} (F/C)	Airspeed (ktas)	Spray Time (min.)	AOA (deg)	MVD (□m)	LWC (g/m^3)	Temp. (F/C)	Press. (psi)	mdot (lbm/s/ft)
CG0886	27.0 /-2.8	23.8 /-4.6	115	22.5	3	29	0.87	350 /177	27.5	0.010

Figure B-3. Warm-Hold Run at a Total Temperature of 27.0°F. (The top shows the conditions for the run. Clockwise from the upper left are photographs showing the suction surface looking downstream, the pressure surface looking downstream, a close-up of the pressure surface, and a close-up of the suction surface.)

Run No.	T_{total} (F/C)	T_{static} (F/C)	Airspeed (ktas)	Spray Time (min.)	AOA (deg)	MVD (μm)	LWC (g/m^3)	Temp. (F/C)	Press. (psi)	mdot (lbm/s/ft)
CG0887	28.5 /-1.9	25.4 /-3.7	115	22.5	3	29	0.87	350 /177	27.9	0.010

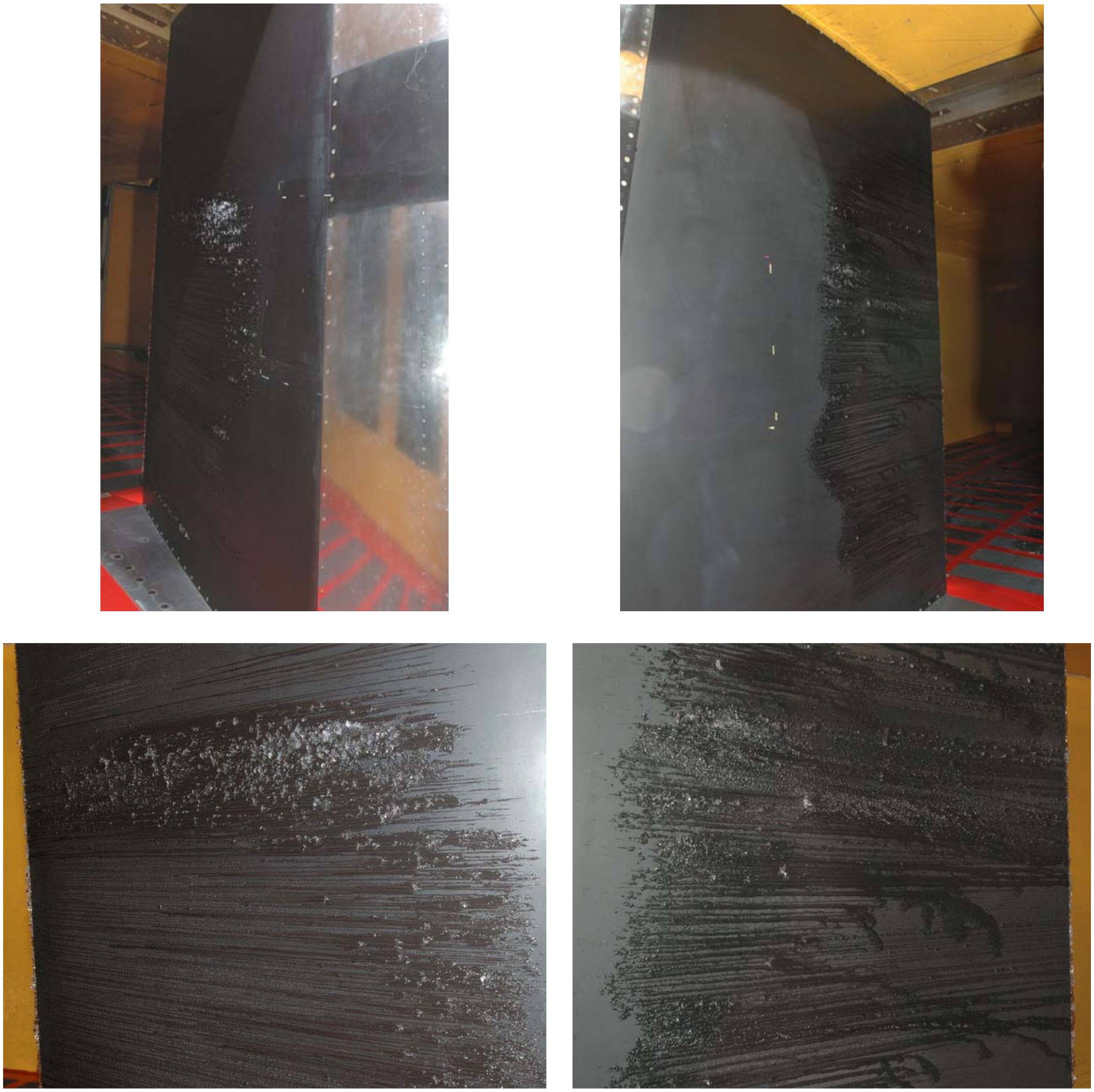

Figure B-4. Warm-Hold run at a Total Temperature of 28.5°F. (The top shows the conditions for the run. Clockwise from the upper left are photographs showing the suction surface looking downstream, the pressure surface looking downstream, a close-up of the pressure surface, and a close-up of the suction surface.)

Run No.	T_{total} (F/C)	T_{static} (F/C)	Airspeed (ktas)	Spray Time (min.)	AOA (deg)	MVD (μm)	LWC (g/m^3)	Temp. (F/C)	Press. (psi)	mdot (lbm/s/ft)
CG0883	29.9 /-1.2	26.8 /-2.9	115	22.5	3	29	0.87	350 /177	27.7	0.010

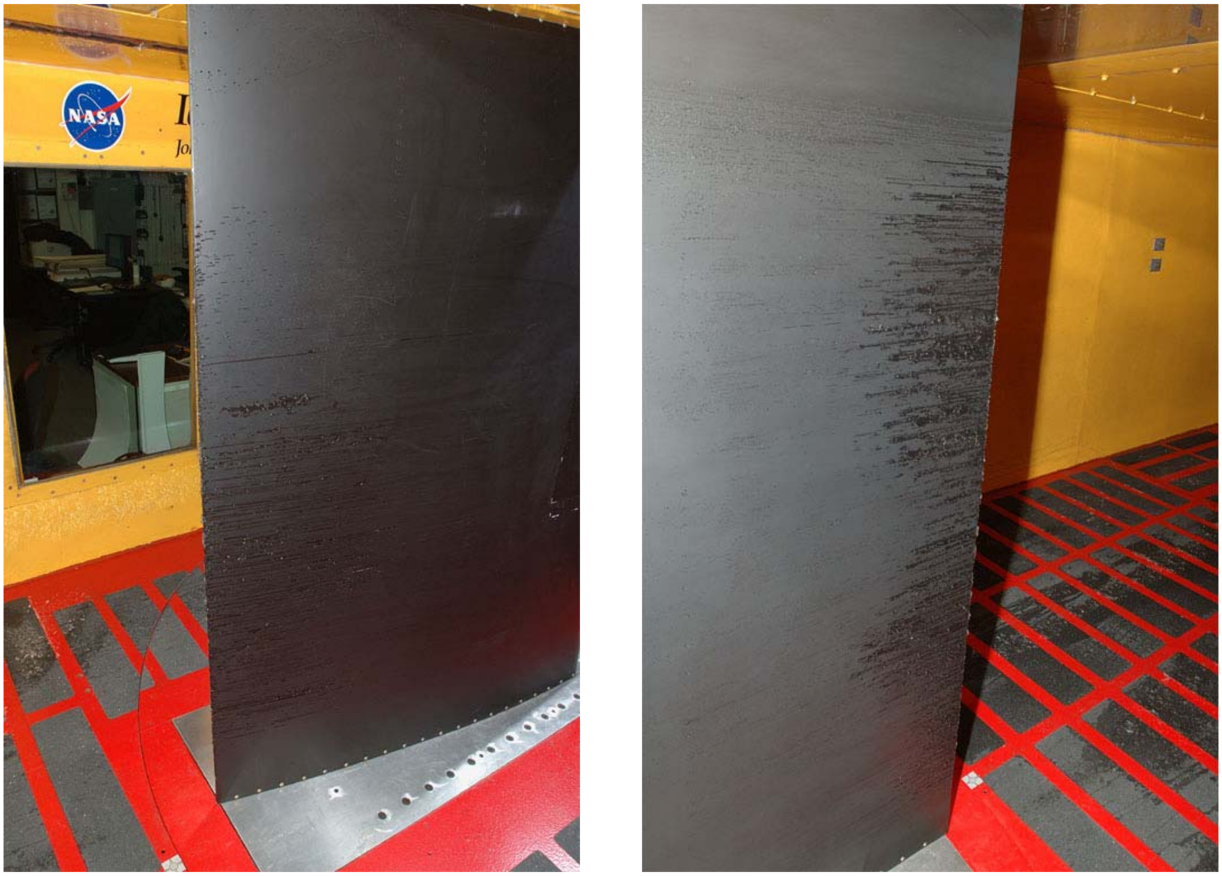

Figure B-5. Warm-Hold Run at a Total Temperature of 29.9°F. (The top shows the conditions for the run. At left is a photograph of the suction surface trailing edge, and at right is a photograph of the pressure-surface trailing edge.)